Master of Science Thesis

Oblique Shock Wave-Boundary Layer Interactions Over Porous Plates

Faculty of Aerospace Engineering

Arti Flinkerbusch 4058968

Date: April 16, 2018

Delft University of Technology

Challenge the future

Delft University of Technology

Oblique Shock Wave-Boundary Layer Interactions Over Porous Plates

Master of Science Thesis

Arti Flinkerbusch

April 16, 2018

Faculty of Aerospace Engineering at
Delft University of Technology

DELFT UNIVERSITY OF TECHNOLOGY
DEPARTMENT OF AERODYNAMICS

The undersigned hereby certify that they have read and recommend to the Faculty of Aerospace Engineering for acceptance the thesis entitled **"Oblique Shock Wave-Boundary Layer Interactions Over Porous Plates"** by **Arti Flinkerbusch** in fulfillment of the requirements for the degree of **Master of Science**.

Dated: April 16, 2018

Supervisors:

Dr. ir. B. W. van Oudheusden

Dr. ir. F. F. J. Schrijer

Dr. D. Ragni

L. Laguarda, MSc.

"Throughout the centuries there were men
who took first steps down new roads
armed with nothing but their own vision."

AYN RAND, THE FOUNTAINHEAD

ABSTRACT

This report discusses an investigation into the effect of a porous plate covering a cavity, on an oblique shock wave-boundary layer interaction. Four porous plates with different hole sizes and porosities, as well as a solid, 'dummy', plate, have been tested in a Mach 2 wind tunnel whereby an oblique shock wave (produced by a wedge) impinged on its surface, for two different wedge angles. Particle Image Velocimetry measurements, and Schlieren images, were recorded and used to analyze the interaction. The effect of the porous-plate covered cavity on the interaction's downstream boundary layer thickness and turbulence, flow separation and interaction length were analyzed and explained. The results showed that first of all, concerning the effect on boundary layer thickness, an increase in boundary layer thickness is induced by from the presence of a porous plate-covered cavity, that the effect of plate hole size, porosity and shock strength on this increase are insignificant. The turbulent kinetic energy of the downstream boundary layer could be observed to increase for a low shock strength, and decrease for a higher shock strength. This leads to the presumption that under specific circumstances a porous plate-covered cavity could lead to a beneficial application as a turbulence decreasing flow control device, but further research will have to validate this. The results showed that flow separation is increased for all plates tested, especially for higher hole sizes and lower porosities. Finally, interaction length was shown to increase due to the presence of the porous plate in all cases measured, although this result is likely highly specific to the design tested in this investigation, as is discussed in the Conclusions chapter. Keeping this in mind, interaction length seemed to increase with decreasing hole size and with increasing porosity. In order to be able to prove the above-mentioned correlations with more certainty, performing a future investigation with a larger parameter range is recommended.

NOMENCLATURE

List of abbreviations

DEHS	Di-ethyl-hexyl-sebacat
FOV	Field of View
NSW	Normal Shock Wave
OSW	Oblique Shock Wave
PIV	Particle Image Velocimetry
SWBLI	Shock Wave-Boundary Layer Interaction
TKE	Turbulent Kinetic Energy

List of symbols

γ	Ratio of specific heats
δ	Boundary-layer thickness
δ_{99}	Boundary-layer height at which 99% of velocity is reached
δ^*	Displacement thickness
θ	Deflection angle
θ	Momentum thickness
μ	Dynamic viscosity
ν	Kinematic viscosity
ρ	Density
τ	Wall shear stress
C_f	Skin friction coefficient
H	Shape factor
M	Mach number
p	Pressure
R	Gas constant
Re	Reynolds number
T	Temperature
u	Horizontal velocity
u_τ	Wall-friction velocity
v	Vertical velocity

Subscripts, superscripts and annotations

$_e$	Pertaining to the free stream
$_{inc}$	Incompressible
$_w$	Pertaining to the wall
$_\infty$	Pertaining to the free stream
$_0$	Pertaining to the undisturbed case
$'$	Fluctuations
$\overline{u}$	Mean value (of u)

CONTENTS

Abstract . . . . **I**

Nomenclature . . . . **II**

1 Introduction **1**
- 1.1 Background 1
- 1.2 Thesis aim and research questions 2
- 1.3 Thesis outline 2

2 Literature review **3**
- 2.1 Introduction 3
- 2.2 Basic interaction 3
- 2.3 SWBLI unsteadiness 5
- 2.4 Causes of SWBLI unsteadiness 7
- 2.5 Dependence of Reynolds number and Mach number 9
- 2.6 Flow control 10
  - 2.6.1 Passive cavity 11
  - 2.6.2 Boundary layer suction 12
  - 2.6.3 Boundary layer bleed / Injection 13

3 Methodology **14**
- 3.1 Introduction 14
- 3.2 Experimental set-up 14
- 3.3 Test matrix and rationale 15
- 3.4 Measurement techniques 18
  - 3.4.1 Schlieren visualization 18
  - 3.4.2 Particle Image Velocimetry 18
- 3.5 Data processing methods 19
  - 3.5.1 Schlieren image processing 19
  - 3.5.2 PIV processing 20
  - 3.5.3 Boundary layer integral parameters 22
  - 3.5.4 Density within the boundary layer 22

4 Boundary Layer Study **24**
- 4.1 Introduction 24
- 4.2 Velocity profile 24
- 4.3 Boundary layer parameters 24
- 4.4 Velocity fluctuations 27

5 Mean flow field **28**
- 5.1 Introduction 28
- 5.2 Description of flow fields 28
- 5.3 Interaction lengths 32
- 5.4 Mean velocity fields and profiles 32
- 5.5 Percentage of backflow 44
- 5.6 Separation area 47
- 5.7 Boundary layer integral parameters over the cavity 47
- 5.8 Vertical velocity over the cavity 53

6 Flow field fluctuations 55
6.1 Introduction 55
6.2 Turbulent kinetic energy plots 55

7 Conclusion 59
7.1 Introduction 59
7.2 Conclusions and answers to the research questions 59
7.3 Recommendations 60

Bibliography 62

A Technical drawing porous plate 1 66

B Shock identification images 67

C Integration heights for displacement and momentum thickness 77

D Determining mass flux through the plates 80

E Turbulence plots 82
E.1 $\overline{u'^2}$ turbulent normal stress flow fields 82
E.2 $\overline{v'^2}$ turbulent normal stress flow fields 85
E.3 $\overline{u'v'}$ turbulent shear stress flow fields 88

Chapter 1

Introduction

1.1 Background

Shock wave-boundary layer interactions (SWBLIs) are phenomena in the field of aerodynamics that have been and continue to be subject to much research. A shock wave is a discontinuous compression and deceleration of flow occurring at supersonic speeds, and the interaction of this with a boundary layer can lead to separation of the boundary layer, unsteady flow, and thermal heating. They can occur on aircraft travelling at transonic and supersonic speeds, and their occurrence can especially be influential on aircraft wings, engine inlets and compressor and turbine blades. On the wing, an aircraft flying faster than its critical Mach number will experience a normal shock somewhere along its surface, and the interaction of this with the boundary layer can cause separation which affects the stability of the wing (especially if this occurs disproportionately on one side). Supersonic engine inlets often have spike inlets (as shown in Figure 2.1) to decelerate the flow by oblique shocks and reflections of them. The interaction of the oblique shock with the boundary layer can cause instabilities in an engine's performance and structural failure (due to the fatigue caused by high-frequency unsteadiness). Also, oblique SWBLIs can occur between the blades in a turbine or compressor stage (as shown in Figure 1.2). Not only can their presence here also lead to engine performance instability and structural failure, but it can make the pressure recovery of the turbine less efficient. Thus, a better understanding of SWBLI phenomena can lead to improvements in the design of wings, engine inlets and compressor and turbine blades, to help to minimize the detrimental effects mentioned earlier.

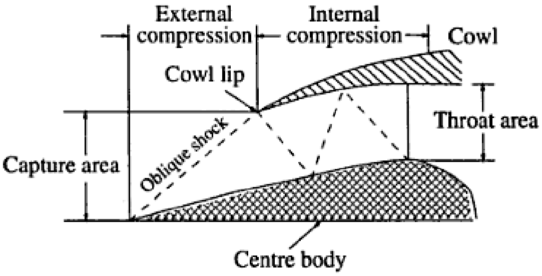

Figure 1.1: Oblique shock inlet found on supersonic engines. From (Sino Defence Forum, 2012).

Figure 1.2: Oblique shocks in a compressor cascade. From (Weber et al., 2002).

Research into SWBLIs started to become significant with the studies of Akeret, Feldmann and Rott (1947), Allen, Heaslet and Nitzberg (1947) and Fage and Sargent (1947). Since then, much research has also been done into the effects of active and passive flow control methods on SWBLIs. Some of the methods researched include boundary layer bleed (Donovan, 1996), the application of micro-ramp vortex generators (Giepman, 2016), and flexible walls (Visbal, 2014). Boundary layer bleed has already been applied as a flow control method to the design of the inlet of the SR-71 Blackbird Graham and Miller (2008). A study by Bur, Corbel and Délery from 1998 discovered the potential usefulness of a porous plate over a cavity as a means of flow control for a SWBLI of a normal shock. Hereby it was found that such a porous plate-covered cavity could achieve a modest decrease in drag, as well as make the shock more localized and decrease its unsteadiness. This came at the expense of a more turbulent and thicker boundary layer downstream. The working principle of the porous plate cavity was that air could flow into the cavity at its downstream end where there was a relatively higher pressure, and out of the cavity at its upstream end where there was a relatively lower pressure (which was confirmed by vertical velocity measurements over the holes). As this study was done at a low Mach number of 1.3, the porous plate's effect on flow separation could not be studied.

Therefore, there is a valuable opportunity for research to be done on the effect of a porous-plate covered cavity on SWBLIs arising from oblique shock waves. If this proves to be a beneficial method of flow control, it could help to make design of engine inlets and turbine and compressor cascades more efficient. Because the topic of oblique SWBLIs over porous plate-covered cavities has not been researched before, an exploratory study examining the method's effectiveness over a range of characteristics such as plate hole size, plate porosity and shock strength is first necessary.

1.2 Thesis aim and research questions

The aim of this thesis is to investigate in what way porous plates covering cavities influence the interaction between an oblique shock wave and a turbulent boundary layer. The research questions that are posed to achieve this are the following:

- How is the effect of the interaction on the downstream boundary layer affected by the presence of the porous plate-covered cavity?
- How is the level of turbulence downstream of the interaction affected by the presence of the porous plate-covered cavity?
- How is the flow separation region affected by the presence of the porous plate-covered cavity?
- How is the interaction length affected by the presence of the porous plate-covered cavity?
- What is the effect of hole size on this influence?
- What is the effect of porosity on this influence?
- What is the effect of shock strength on this influence?

The first three questions will be answered by PIV measurements, and the fourth by Schlieren measurements. These will be answered over a range of hole sizes, porosities and shock strengths, thereby answering the last two.

1.3 Thesis outline

In Chapter 2, the existing literature on SWBLIs is surveyed to provide background information to understand the investigation. In Chapter 3 the way the experiment has been performed is explained, what has been measured, and how the data gathered from it has been processed. In Chapter 4 the results pertaining to the upstream boundary layer are shown and compared to other investigations. This is done to give an indication of the reliability of the results of the investigation. In Chapter 5 the time-averaged, steady aspects of the flow field are discussed. This is followed by the unsteady aspects of the flow field in Chapter 6. In Chapter 7, the conclusions that can be drawn from this are discussed and how they fulfill the aim and answer the research questions. Also in that chapter, recommendations are made for further investigations into this topic: how the same research could be done better, or what topics might be valuable to research further. Appendix A shows a technical drawing of one of the plates that was used, Appendix B shows the images used to determine the interaction lengths, Appendix C shows the heights (defined by curves) that were used to calculate displacement and momentum thicknesses, Appendix D shows an attempt to calculate the mass flux through the plate and Appendix E shows plots of the turbulence stresses.

Chapter 2

Literature review

2.1 Introduction

In this chapter, some of the literature on SWBLIs is reviewed, specifically the parts which are relevant background information to understand the investigation that has been performed. First, the steady aspects of a basic oblique SWBLI are discussed, as well as in what ways it differs from an inviscid case, and how it is different from other types of SWBLIs. Next, the unsteady aspects are discussed, and what are generally thought to be the causes of this unsteadiness. Finally, the effects of Reynolds and Mach number on the interaction, and of flow control devices (relevant to the porous-plate covered cavity), are discussed.

2.2 Basic interaction

Babinsky and Harvey (2011) classify the interaction of a shock wave with a boundary layer into 5 distinct scenarios. These are:

1. An oblique shock reflection off a flat plate
2. Ramp flow
3. A normal shock
4. An imposed pressure jump
5. An oblique shock induced by a forward facing step

The present study is focused on oblique shock reflections off of flat plates, so for more information on the other four types the reader is referred to Harvey & Babinsky's book. In the inviscid case, an oblique shock is normally analyzed as moving towards the wall with a constant angle and reflecting off it at the wall itself, as shown in Figure 2.1. The reason why this cannot be the case when viscosity is taken into account is trivial. Because airspeed decreases to zero as one approaches the wall, this means there is a region of subsonic flow near the wall, where an oblique shock cannot exist.

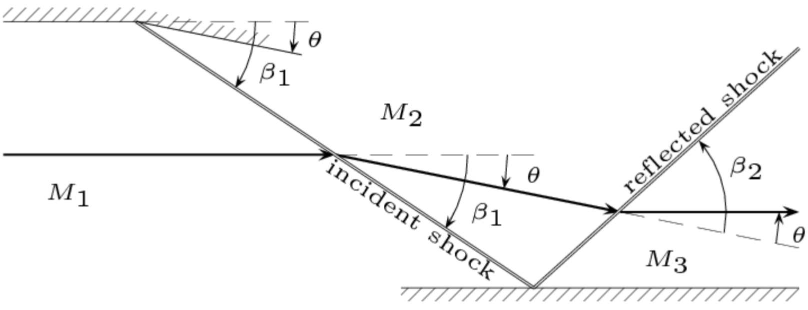

Figure 2.1: Oblique shock reflecting off a flat plate, neglecting viscous effects (Chen, 2008).

The viscous case whereby an oblique shock is incident upon a boundary layer on a flat plate can lead to separation of the boundary layer, or that it remains attached. These cases are shown in Figure 2.2 and Figure 2.3. In the figures, flow moves with a uniform velocity from left to right, and an oblique shock enters from the top-left. Three regions are defined: region II as the one where the incidence takes place, and where the compression waves emanate from the boundary layer, and region I and region III as the regions upstream and downstream from it respectively.

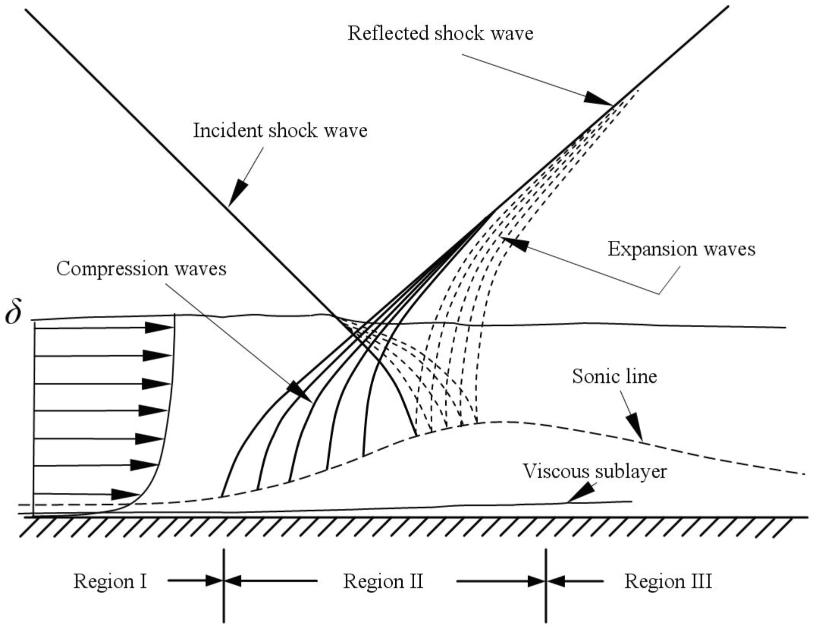

Figure 2.2: Oblique shock interacting with a boundary layer over a flat plate, unseparated case. From Délery and Bur (2000) as reported by Humble (2009).

The unseparated case is shown in Figure 2.2. As the oblique shock wave (labelled as the 'incident shock wave' in the diagram) enters the boundary layer, the local flow velocity (and Mach number) decreases, and this also increases the steepness of the angle of the shock and its strength (e.g. pressure rise). When the shock falls upon the sonic line, the pressure rise across the shock gets transferred to the subsonic layer, which causes the flow there to decelerate. Because the flow here is subsonic, a lower flow speed means that the boundary layer thickness increases, and also that the deceleration takes place continuously over an upstream distance. In region III, enough mixing of momentum has taken place so that the flow accelerates again and the boundary layer thickness decreases again. When the subsonic layer thickens, compression waves emanate from it. This is because the supersonic flow above the incoming boundary layer is confronted with a streamline, the sonic line, of increasing curvature. The compression waves ultimately coalesce to form the reflected shock wave. Before that, when the compression waves intersect with the incident shock wave, several compression waves split from it, which later reflect from the sonic line as expansion waves. Shock strength signifies the pressure rise that takes place across the shock, and this can be increased by increasing the freestream Mach number or the deflection angle of the ramp which caused the shock. With increasing shock strength, the pressure rise in the subsonic layer would also increase, the deceleration of the subsonic region of the boundary layer would start more upstream, and so would the emanation of a compression shock from the thickening boundary layer. The intersection of the incident shock wave and the reflected shock wave would take place higher above the wall.

When the shock strength is high enough the boundary layer may separate as a result of this interaction, and this is shown in Figure 2.3. Again, the incident shock wave decreases in strength throughout the boundary layer and becomes more steep. While it does so, expansion waves emanate from it away from the wall. When it interacts with the sonic line, it transfers its pressure rise to the boundary layer. This time, the boundary layer decelerates to such an extent that separation occurs. Because the deceleration in the subsonic region takes place over a region upstream, the actual point of separation (indicated with 'S' in the figure) is upstream of the point where the shock wave hits the boundary layer. Because thickening of the boundary layer takes place further upstream, the compression waves emanating from the boundary layer also emanate further upstream. This causes the reflected shock wave to appear further away from the wall and more to the left like in the figure. When the detached boundary layer flows over the separation bubble, momentum is mixed with it which will cause the boundary layer to reattach. When it does so, the change in curvature of the sonic line causes compression waves, which coalesce as a reattachment shock wave, to emanate into the freestream. The presence of this reattachment shock wave is a significant difference with the unseparated case. After reattachment, it can take in the order of 10 boundary layer thicknesses' length for the boundary layer's properties (velocity profile, pressure) to recover to pre-interaction levels.

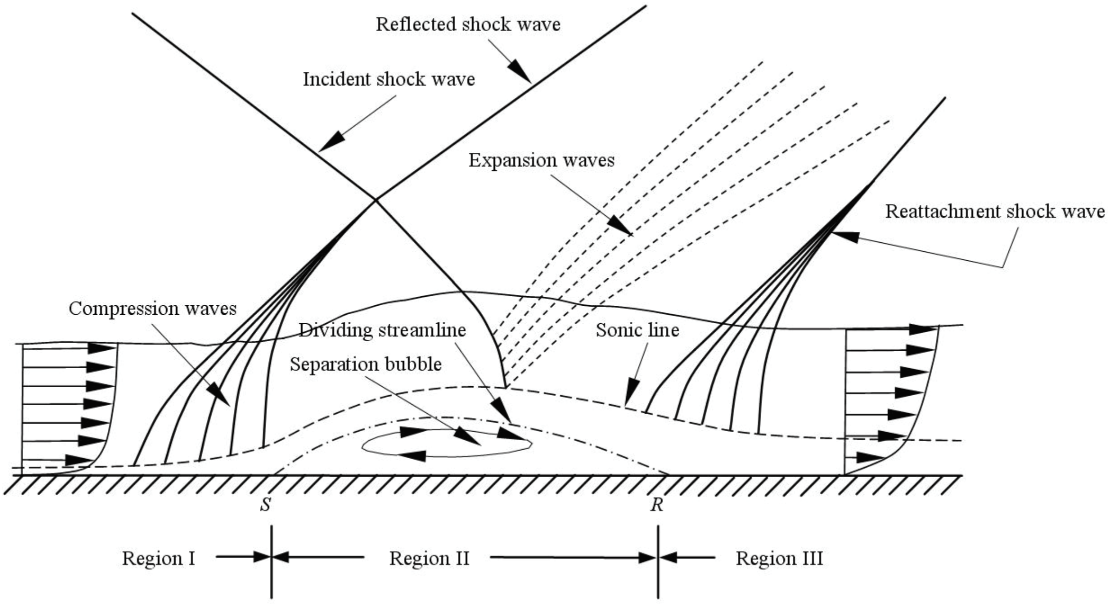

Figure 2.3: Oblique shock interacting with a boundary layer over a flat plate, separated case. From Délery and Bur (2000) as reported by Humble (2009).

It must be stated that the occurrence of separation in the interaction is not binary, as it may seem from the way it has been explained up to now. In Figure 2.4 Schlieren visualizations are shown of the interaction with increasing deflection angle. Hereby the interaction morphs gradually from the situation portrayed in Figure 2.2 to that shown in Figure 2.3. The situation in between the two is one whereby there is separation for some of the time, but no region at which the flow is constantly separated. A region over which the flow is constantly separated over time is dubbed a mean separation bubble.

When the shock strength becomes excessively large, a normal shock will occur over a small region between the incident shock and the compression emanating from the thickening boundary layer. This is dubbed a Mach reflection by Campo (2014). A Schlieren visualization of a Mach reflection is shown in Figure 2.5, and a sketch of the phenomenon is shown in Figure 2.6. The occurrence is dictated by the von Neumann condition (von Neumann, 1943), which says that a normal shock will occur if a weak oblique shock (which would in this case otherwise be the reflected shock downstream from the incident shock) cannot deflect the flow enough to make it align with the freestream. According to the Edney classification, the interaction in Figure 2.2 and Figure 2.3 is called a Type I interaction and that of Figure 2.6 is called a Type II interaction (Edney, 1968).

2.3 SWBLI unsteadiness

The structures shown in Figure 2.2, Figure 2.3 and Figure 2.6 are by no means fixed in time. The turbulent boundary layer contains turbulent flow of which the velocity fluctuates over time, the mean separation region varies in size, and the position of the shock foot does not stay constant

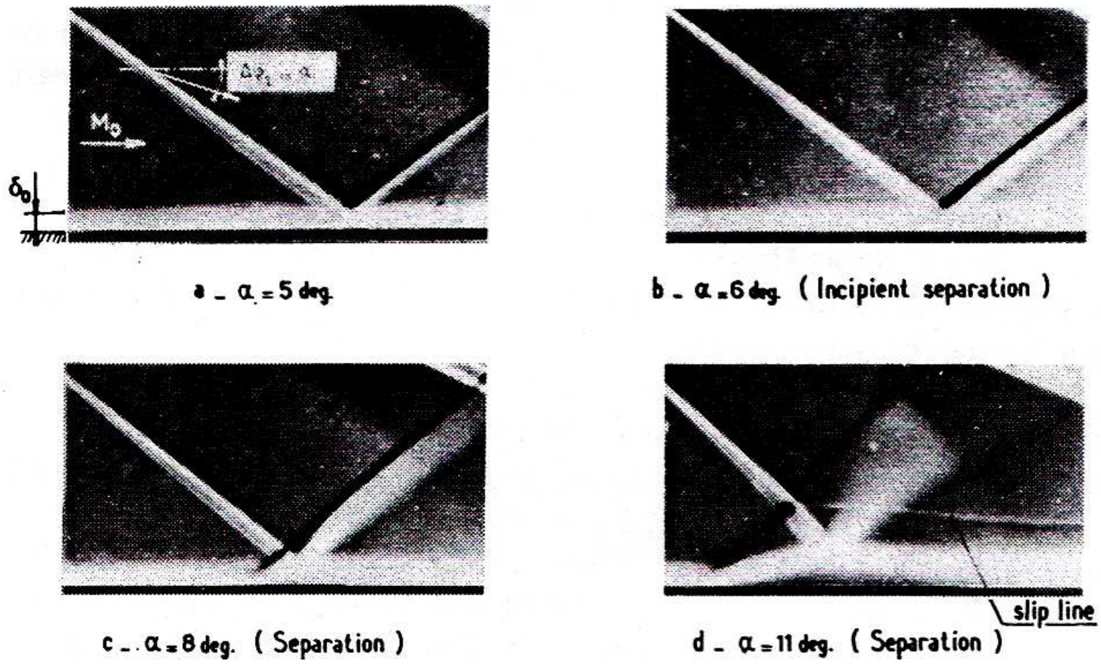

Figure 2.4: Schlieren visualizations for shock interactions at M_∞=1.93, with increasing shock strength (through increasing oblique shock angle) from a) to d). From Délery and Marvin (1986).

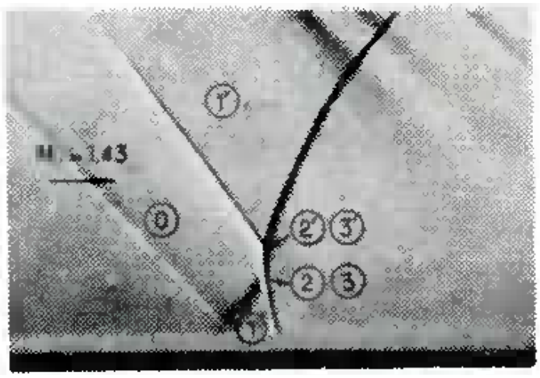

Figure 2.5: Schlieren visualization of a Mach reflection. From Délery and Marvin (1986).

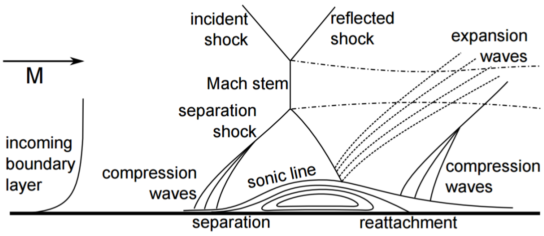

Figure 2.6: Mach reflection, whereby a normal shock (or Mach stem) forms between the incident shock and compression waves. From Campo (2014).

over time and oscillates. Piponniau, Dussauge, Debive and Dupont (2009) plotted the power spectral density of the vertical velocity of the reflected shock at three deflection angles, shown in Figure 2.7. Hereby, at the deflection angle of 5.5° some separation started to occur, and at 9.5°, more significant separation occurred. It is clear that when separation occurs, the peak intensity rises and is found at a lower frequency.

From another study, the variation of frequency along the x-axis in the interaction has been examined. In Figure 2.8, the variation of the frequency spectrum of Figure 2.7 with x is shown, albeit only for the deflection angle 8°. Although the frequencies of Figure 2.7 are based on the shock foot motion and those of Figure 2.8 on pressure measurements and their variation, the frequencies can still be compared. It is visible that at the interaction, the frequency spectrum is similar to the one in Figure 2.7. In Figure 2.7 the curve for 8° has its highest peaks between 1.5×10^2 and 6×10^2 Hz, and in Figure 2.8 there is a clear peak at 3×10^2 Hz. In Figure 2.8, what is visible from the rest of the chart is that while a low frequency peak is found at the interaction, a higher peak is found at x-locations further away from it. At the latter, a peak is found around 10^4 Hz and slightly higher than that for the incoming boundary layer, and at approximately $7 - 8 \times 10^3$ Hz for the downstream boundary layer. Erengil and Dolling (1991) studied the unsteadiness of a 28° compression ramp interaction and measured a peak of $0.3 - 1.0$ kHz due to

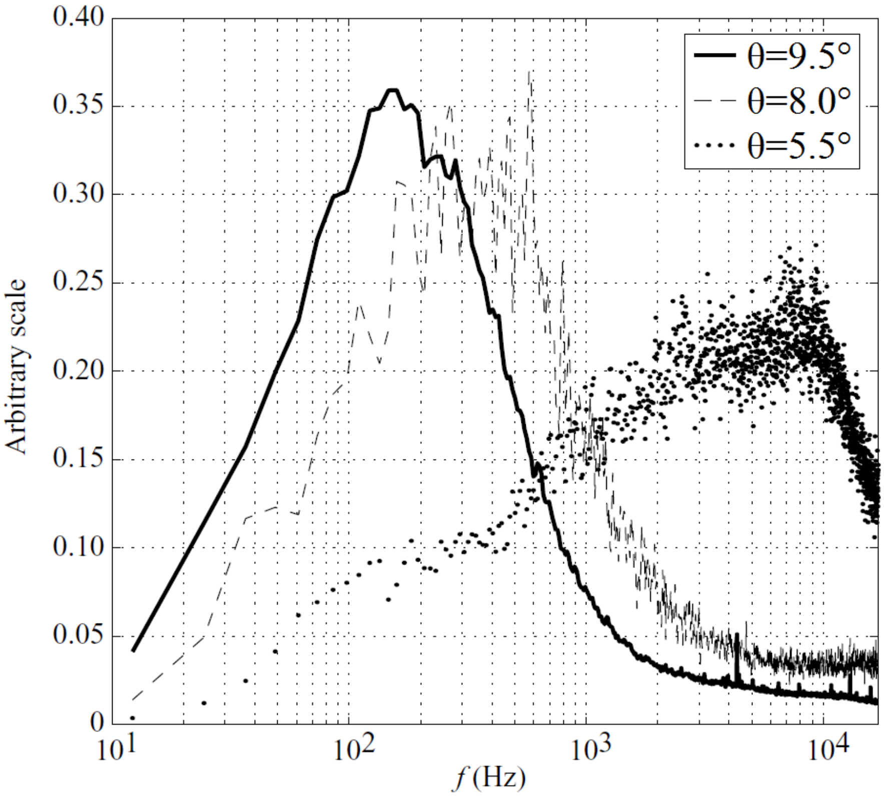

Figure 2.7: Power spectral density (on an arbitrary scale) vs. frequency for 3 different deflection angles. From Piponniau et al. (2009).

the shock foot motion, and a peak of $20 - 40$ kHz due to the boundary layer turbulence, results which lie close to the above.

Souverein (2010) investigated the frequencies of the oscillations of velocity measurements in an oblique SWBLI, by finding time scales over which significant autocorrelation was measured. This was done when the flow was deflected by 6.0° in an interaction at Mach 1.7. This was analyzed at specific locations in the interaction. At the incoming boundary layer, oscillations of 25 kHz were found. At the reflected shock 1.25 kHz was found. At the mixing layer, the layer above the separation bubble, a frequency of 12.5 kHz was found, and in the bubble itself, 4 kHz. Summarizing the above findings, it can be stated that in an oblique SWBLI the peak frequency of the reflected shock can range from 140 to 9000 Hz and is heavily dependent on deflection angle and that the peak of the incoming and downstream boundary layer can range from $10 - 25$ kHz. The main conclusion to draw is that these ranges are distinct from one another, that the unsteadiness of the reflected shock is of a frequency 2 to 3 orders lower.

2.4 Causes of SWBLI unsteadiness

There are two main theories about how these unsteady phenomena affect each other, which have been dubbed by some researchers as the 'upstream mechanism' and the 'downstream mechanism':

Upstream mechanism: According to this theory the velocity fluctuations in the turbulent boundary layer coming in from upstream cause the fluctuations in the position of the shock foot. In Figure 2.9 it is illustrated more clearly how a positive velocity fluctuation can cause a reluctance of flow to experience a shock and thus make the shock foot move downstream, and how a negative velocity fluctuation will have the opposite effect and shift the shock foot upstream. A model relating these effects was first proposed by Plotkin (1972). In his paper it was already concluded that this was the mech-

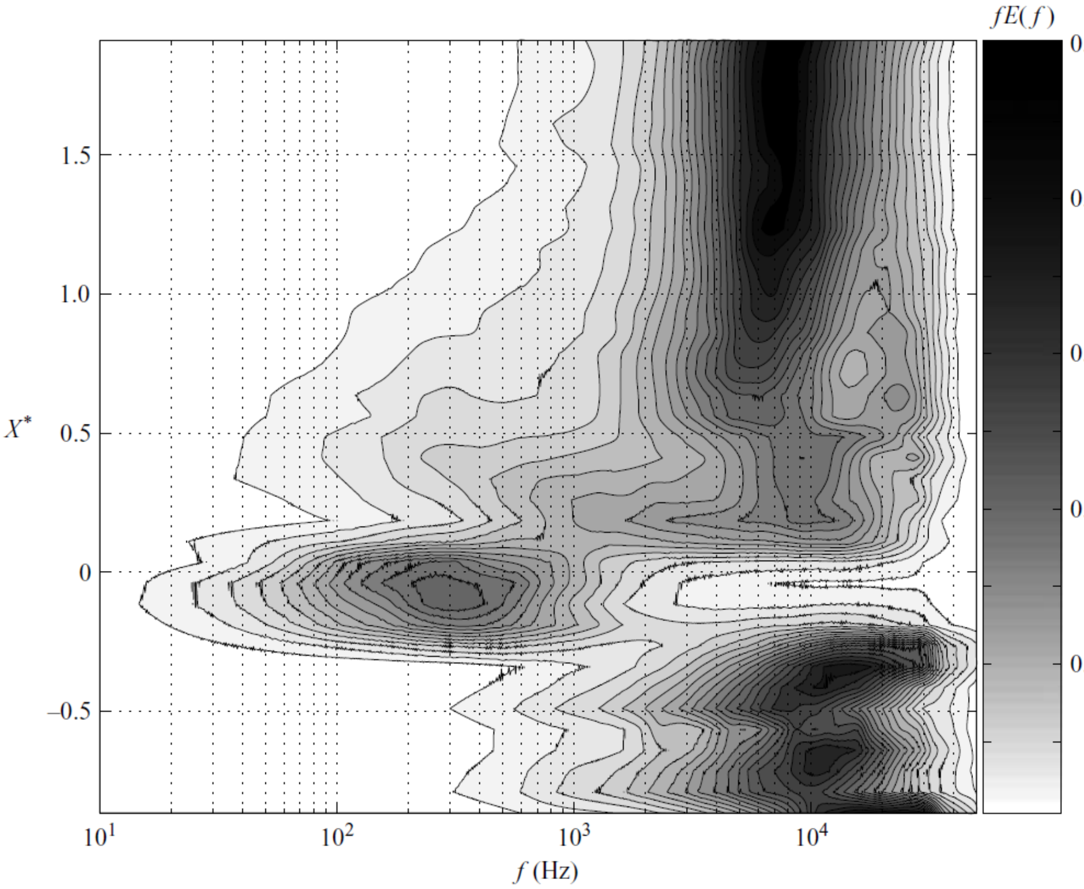

Figure 2.8: Power spectral density of pressure measurements (arbitrary scale) vs. frequency and x-location, for deflection angle 8°. From Dupont et al. (2006).

anism that explained the shock foot's movement because of the model's strong agreement with experimental data. More observations correlating the upstream boundary layer's velocity fluctuations with the shock foot's movement were later done by various researchers (Andreopoulos and Muck, 1987; Ünalmis and Dolling, 1994; Beresh, Clemens and Dolling, 2002; Ganapathisubramani, Clemens and Dolling, 2006, 2007; Humble, Elsinga, Scarano and Van Oudheusden, 2009).

Downstream mechanism: In this theory, the low-frequency motion of the shock foot occurs due to the pulsation of the size of the separation bubble. The bubble continually grows and shrinks, as air flows out of it as it sheds vortices and air flows in from the mixing layer. This explanation started to gain traction when two investigations weakened the evidence for the upstream mechanism and also highlighted a correlation between the separation bubble's size and the movement of the shock foot: (Erengil and Dolling, 1991; Thomas, Putnam and Chu, 1994). The phenomenon has been supported further in various papers with observations noting the correlation between the two oscillations: (Dupont et al., 2006; Wu and Martin, 2007, 2008; Touber and Sandham, 2008; Piponniau, 2009).

Some scholars have put forth the notion that the shock foot's motion is influenced by both the upstream and downstream mechanisms, as opposed to exclusively one of the two (Brusniak and Dolling, 1994; Souverein, Dupont, Debiève, Van Oudheusden and Scarano, 2010; Clemens and Narayanaswamy, 2014). The latter two of these specifically argued that the severity of the separation of the boundary layer determines which of the two mechanisms is more dominant:

that for a highly separated flow, the downstream mechanism is, and for a weakly separated flow, it is a combination of both. Some of the aforementioned studies have investigated the correlation between the upstream boundary layer or the pulsation of the separation bubble and the movement of the shock foot in a compression ramp interaction or a blunt-fin interaction (which are other cases of SWBLI, shown in Figure 2.10 and Figure 2.11), but these results are still interpreted as supportive of the downstream or upstream mechanism in general.

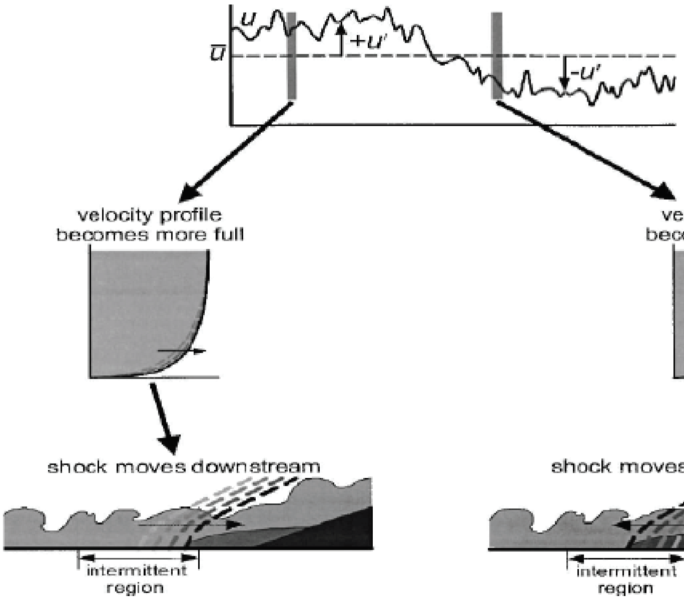

Figure 2.9: Turbulent boundary layer velocity fluctuations and their effect on the shock foot according to the upstream mechanism. From Beresh et al. (2002).

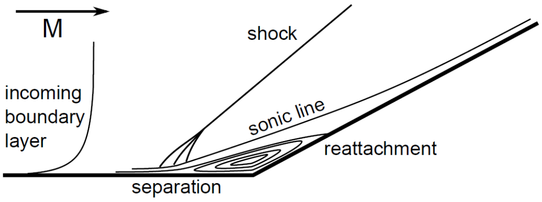

Figure 2.10: Compression ramp interaction. From Campo (2014)

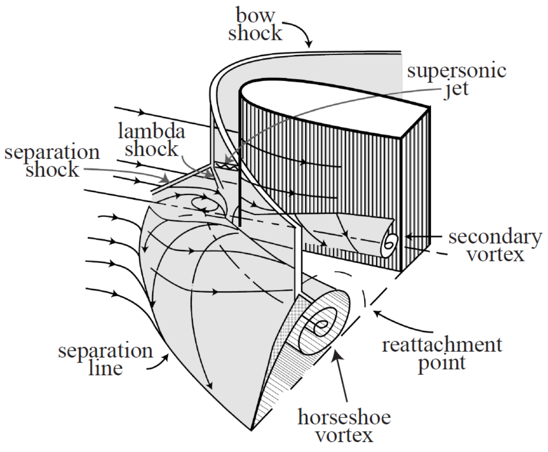

Figure 2.11: Blunt-fin interaction. From Houwing et al. (2001) as reported by Bueno et al. (2006)

2.5 Dependence of Reynolds number and Mach number

A visible effect of an increase in Reynolds number is shock focalisation. For small Reynolds numbers, the reflected shock (the compression waves emanating from the sonic line) is more distributed into separate waves, and at high Reynolds numbers it is more concentrated (Souverein, 2010). A visible effect of increasing Mach number is that the oblique shocks will make smaller angles with the horizontal. Another effect is that it decreases the growth rate of the thickness of the mixing layer (Papamoschou and Roshko, 1988). Also, in a paper which accepts the downstream mechanism, it is stated that the aforementioned growth rate is proportional to the characteristic Strouhal number of the separation bubble (Piponniau et al., 2009) (the Strouhal number is the non-dimensionalized frequency of the bubble's oscillations), which would mean that the Mach number correlates with the separation bubble's oscillating frequency. The pressure rise and interaction length have been verified to have a positive correlation with Reynolds number for laminar boundary layers. Concerning the streamwise extent of the interaction, for low to moderate Reynolds numbers ($Re_\delta < 10^5$) this increases with Reynolds number, At Re_δ higher than that, the extent decreases with increasing Reynolds number (Humble, 2009). The findings of Ginoux, shown in Figure 2.12, put forth a complex relationship between Reynolds number, Mach number, interaction length and pressure rise (Ginoux, 1973). The label on the y-axis indicates that interaction length and Reynolds number have a positive correlation in the laminar regime, a negative correlation in the transitional regime, and no correlation in the turbulent regime. For the laminar and transitional regimes, Mach number has a minimal effect, although for the turbulent regime, interaction length seems to decrease with an increase in Mach number.

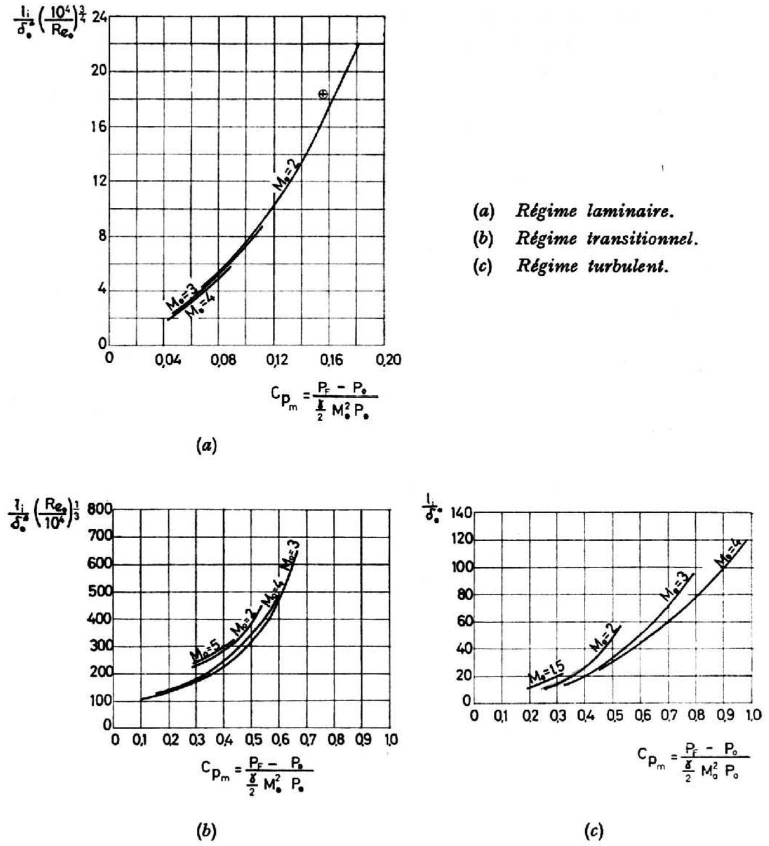

Figure 2.12: Interaction length relation pressure rise over complete shock system, for a) laminar regime b) transitional regime c) turbulent regime. From Ginoux (1973).

2.6 Flow control

Many investigations have been performed on how to apply flow control to SWBLIs to reduce their negative effects. Flow control is defined as manipulating a flowfield actively or passively to effect a desired change (Gad-el Hak, Pollard and Bonnet, 1998). Within the context of SWBLIs, the aims of flow control can be seen as to reduce drag, unsteadiness, or both. This is most often done by preventing or reducing the extent of flow separation. A clear distinction is made between passive flow control and active flow control. The former entails methods which don't auxiliary power, the latter those which do. Within active flow control methods, a distinction is made between pre-determined and reactive flow control. The former is one whereby the way in which flow control is applied is determined a priori, and the latter is one whereby the way flow control is applied depends on the flow itself, and is applied with sensors, actuators and a control loop. There are more distinctions and categorizations which can be made, (concerning the desired effect on the flow, the suction or injection of air, the type of control loop etc.), but concerning SWBLIs these distinctions are the most relevant (Gad-el Hak, 2001). Flow control methods which have been studied applied to SWBLIs include turbulators (Davidson and Babinsky, 2015), vortex generators (Giepman, 2016), vortex generator jets (Bueno et al., 2006), local surface deformations (Délery and Bur, 2000), and flexible walls (Willems, Gulhan and Esser, 2013). In the following subsections, only flow control methods relevant to the action of the porous plate-covered cavity are discussed, namely the application of a passive cavity, and that of boundary layer bleed and suction.

As a side note, SWBLIs can be successfully applied as a means of flow control themselves. Studies have shown that after interaction with a shock, the boundary layer will continue downstream with more turbulence (Anyiwo and Bushnell, 1982; Zang, Hussaini and Bushnell, 1984), which can make it more resistant to flow separation (Schofield, 1985). However, this is a method of flow control not discussed in this section and this thesis.

2.6.1 Passive cavity

SWBLI flow separation can also be counteracted by a passive cavity directly under the interaction. This is because circulation can occur within such a passive cavity and high-pressure flow can travel from downstream to the low-pressure region upstream, which can diminish the pressure rise and its effects. This situation is shown in Figure 2.13. An investigation by McCormick (1993) compared the effectiveness of a vortex generator and a porous wall with a cavity underneath, in preventing separation and pressure losses due to a normal shock. In the uncontrolled case, a large separation bubble formed. It was found that the vortex generators significantly suppressed separation, but still caused a significant total pressure loss, whereas the passive cavity was found to be more effective at retaining the total pressure.

Tests have also been performed whereby such a passive cavity has been employed, but enclosed by a type of cover only allowing a certain extent of air to flow through. Gefroh et al. investigated the effect of a passive cavity covered by mesoflaps, a set of flexible flaps rigidly fixed at one end and allowed to deflect at the other, on an oblique SWBLI (Gefroh, Loth, Dutton and McIlwain, 2002). The mesoflaps do not only limit mass flow, but also make the angle at which mass flow is bled and sucked highly aligned with the flow direction, which will be explained to be efficient in the next subsection. The most visible effect of the mesoflaps was that an oblique shock emanated from the first flap (understandably because the effective wall curvature changed there), which was more upstream than for the standard case with a flat plate. Furthermore, it was found that downstream of the interaction, the thinnest displacement and momentum boundary layer thicknesses occurred with the thinnest, most flexible array of mesoflaps which let through the most air. It was also found that the thinnest mesoflaps turned out to have the least stagnation pressure losses. The study also concluded that the performance of the method was limited by the bleeding of air in the upstream part of the cavity, and an extra injection of air upstream was recommended to improve performance.

A porous wall covering a cavity can function in the same way, enable passive suction downstream and bleeding upstream and diminish the effects of a shock. How this can happen is shown in Figure 2.15 for a near-normal shock over an airfoil. This specific method has not yet been tested for an oblique SWBLI, but it is expected that when applied, the thickening and separation of the boundary layer could be diminished whilst the total pressure loss could be slightly higher, similar to the results of the mesoflap array.

A 1998 study investigated such a porous wall covering a cavity on a turbulent boundary layer interacting with a normal shock in a channel flow (Bur et al., 1998). The effect of four different walls were tested by applying them under the boundary layer directly under the interaction. The effects were that a modest decrease in drag was achieved, and that the shock was more localized and its unsteadiness was decreased. Also, the boundary layer's turbulent shear stress

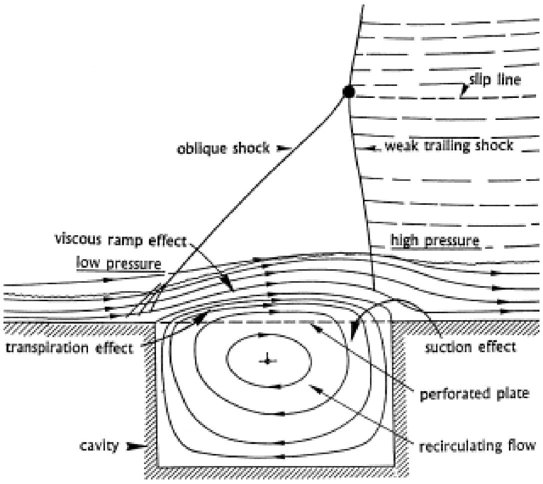

Figure 2.13: Passive cavity under a normal SWBLI. From Délery and Bur (2000).

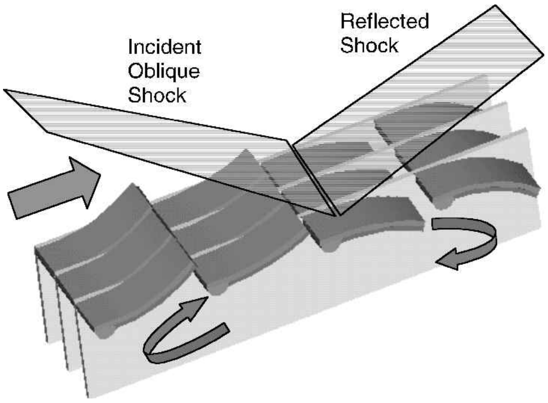

Figure 2.14: Mesoflap array covering a passive cavity, impinged upon by an oblique shock. From Gefroh et al. (2002).

and turbulent kinetic energy were increased, and so were the displacement and momentum thicknesses and its shape factor. Because the Mach number was as low as 1.3 no significant shock-induced separation even occurred in the reference case, and there is no evidence that this can prevent or reduce flow separation.

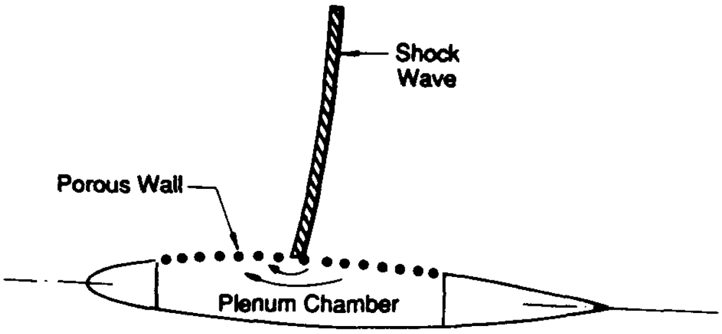

Figure 2.15: An airfoil with a porous wall on its upper surface. From Gad-el Hak and Bushnell (1991)

2.6.2 Boundary layer suction

A common active flow control method is (boundary layer) suction, whereby air is sucked into the wall. This leads to a fuller velocity profile (a lower shape factor H), which delays or prevent transition or separation, and can lead to an asymptotic turbulent boundary layer (i.e. one which has a constant momentum thickness and doesn't grow further). When suction is applied to a SWBLI, this can prevent flow separation and thus unsteadiness, but because the shock will be more localized the wave drag produced will be higher. What must also be taken into account is captation drag which arises from swallowing a part of the flow. Downstream a decrease in friction drag from the thinner boundary layer can be expected, but overall an increase in drag from the application of boundary layer suction is likely (Délery and Bur, 2000).

The prevention of flow separation has been found to have improved when the direction in which suction was applied was pointed 45° towards the incoming flow (Purohit, 1987). Specifically concerning the application of suction, it is advised to use separated chambers to contain the air drawn through each suction hole, to prevent that for individual holes, pressure in a hole might become larger than the external pressure and unintended bleeding might occur (Gad-el Hak and Bushnell, 1991).

A study investigated the influence of two methods, namely boundary layer suction, and boundary layer suction downstream of a porous wall, on the interaction of a normal shock with the boundary layer in channel flow (Benay, Bur, Corbel and Délery, 2000). The Mach number used was 1.4, which was too low to form a separation bubble, so that the effect on shock-induced separation could not be clearly seen. The effects that were noted were that boundary layer suction alone decreased the displacement thickness and momentum thickness significantly, and also decreased the turbulent shear stress and turbulent kinetic energy.

2.6.3 Boundary layer bleed / Injection

The opposite of suction is bleeding or injection, whereby air is added to the flow. The effectiveness of this method may seem contradictory as suction has just been explained to be an effective method to prevent separation. However, Délery & Bur mention that when injection takes place just before a separation bubble, beyond a certain amount of mass flow this will decrease the length of the separation region, in a configuration as shown in Figure 2.16. This is because the airspeed in the shear layer just above the separation bubble will be higher, causing it to reattach sooner.

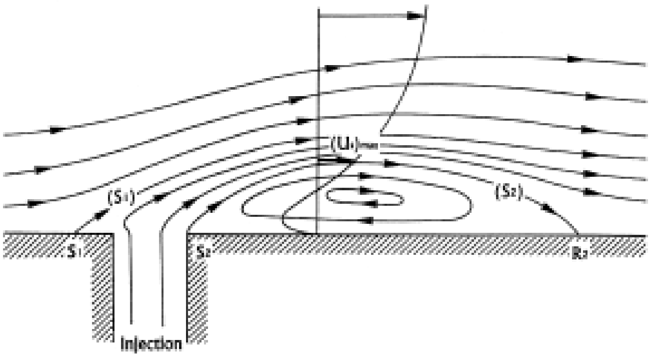

Figure 2.16: Mass injection just before a separation bubble. From Délery and Bur (2000)

A numerical simulation was aimed at applying bleed to preventing flow separation due to an oblique SWBLI, at a range of mass flow rates and bleed angles (Hamed, Yeuan and Shih, 1995). It found an optimum mass flow rate, and that the angle between the bleed direction and the streamwise direction could best be at 20° (the smallest angle tested) to be the most effective in preventing flow separation and obtaining the thinnest downstream boundary layer. The latter is understandable because this will likely increase the velocity of the air added to the near-wall part of the boundary layer.

When investigating a completely tangential flow injection at Mach 3.4, it was experimentally found that the optimal location for flow injection (out of those tested) for an oblique SWBLI were at 0.33δ height and between 5.5 and 7.1δ upstream of the interaction (Donovan, 1996), to limit downstream pressure and boundary layer velocity losses. It must be noted that this completely tangential injection could only take place by having a downwards step in the bottom wall.

Chapter 3

METHODOLOGY

3.1 Introduction

In this section the method by which the investigation has been performed is explained, and the rationale behind it. Firstly, the wind tunnel that has been used for the experiments is shown and discussed. Next, it is explained what plates have been tested, under what conditions, and why these have been chosen in this way. In section 3.4, the workings of the methods that have been used, Schlieren visualization and Particle Image Velocimetry (PIV) are made clear, and in section 3.5, the way the results from these methods have been processed is explained.

3.2 Experimental set-up

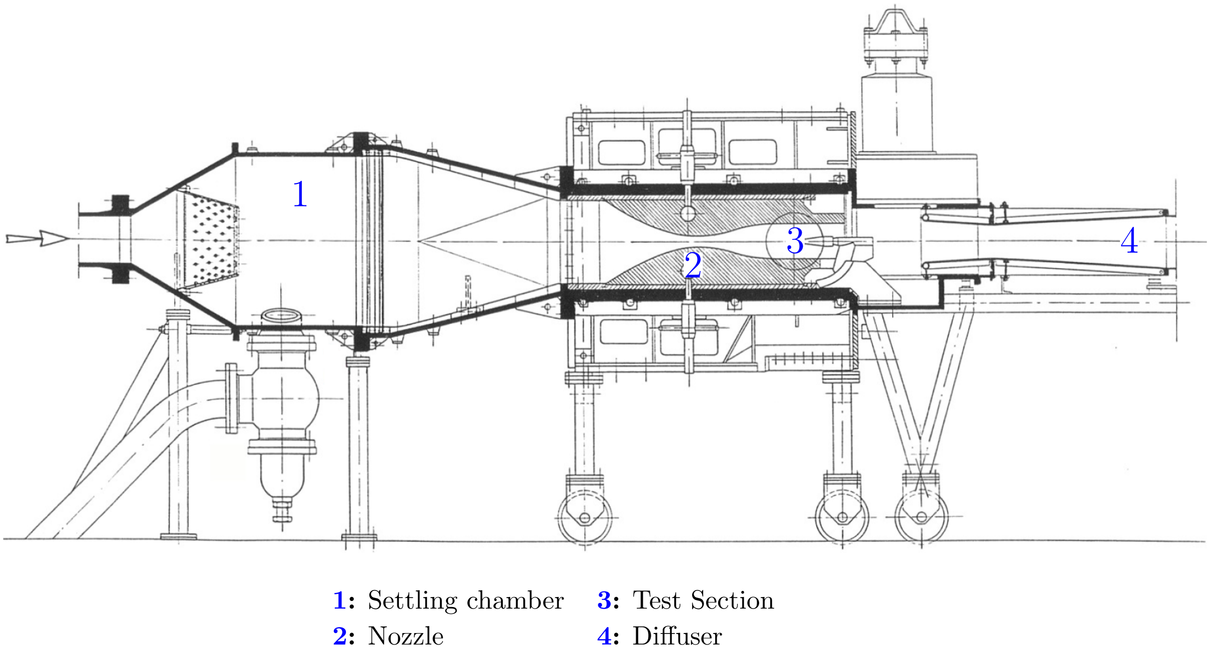

Figure 3.1: ST-15 wind tunnel

Experiments have been performed in the ST-15, a supersonic wind tunnel at Delft University of Technology, a cross-section of which is shown in Figure 3.1. The ST-15 is a blowdown wind tunnel, meaning that the flow does not travel in a closed loop but from a reservoir to the outside world. From the left, flow enters the settling chamber from a large reservoir of 300m^2 volume at a pressure of more than 40 bars. At the nozzle, sonic flow and beyond that, supersonic flow is reached. Different nozzle blocks can be applied at sections 2 and 3 to achieve different Mach numbers, namely 1.5, 2.0, 2.5 and 3.0. For the current investigations, only the set-up for the Mach number of 2.0 was applied. The test section for this set-up was 150mm wide and 151.9mm high. A wedge (or shock generator) was mounted to the ceiling of the test section, and two so-called 'inserts' were screwed to the floor of the section with which a 188mm long plate could be firmly clamped down. In Figure 3.2a), the test section with the wedge and both inserts installed (but without a plate) is shown. In this way, the effect of an oblique shock, arising from supersonic flow hitting the wedge, impinging on a porous plate covering a cavity could be tested.

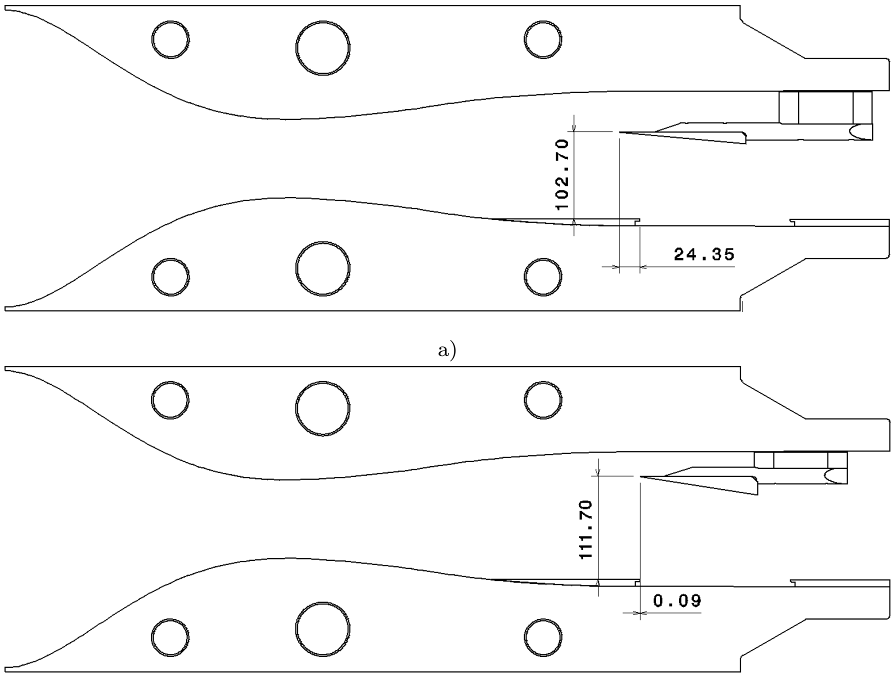

a)

b)

Figure 3.2: ST-15 nozzle and test section, with the plate clamped by the inserts and a) 5.0° wedge and b) 8.8° wedge mounted above.

3.3 Test matrix and rationale

The plates that were used were such that the downstream half of them was made porous and covered a cavity. The design was based on preliminary tests which showed this to be a configuration in which an oblique shock would impinge on the porous section. In the configurations used, the shock from the 5.0° wedge impinged at a distance of 44.8% along the porous section, and for the 8.8° wedge, it impinged 62.9% along the porous section. Top and bottom views of one of these plates can be seen in Figure 3.3. More elaborate drawings and dimensions of a typical plate are shown in Appendix A. The porous section stretched from 89mm to 168mm along the plate's length, and was 130mm wide. This section had a thickness of 1mm and covered a cavity of 7mm depth. The 7mm depth of the cavity was convenient because this was the space allowed by the inserts. Non-dimensionalizing this by the undisturbed boundary layer thickness δ_0 (using the value of 5.0mm found by similar investigations) makes the depth $h/\delta_0 = 1.4$. In a previous investigation of Chanetz and Pot (1987), it was found that upon decreasing the depth of a porous plate-covered cavity under a normal SWBLI from h/δ_0 =10 to 2, the operation of the cavity was hardly altered. Decreasing it to a value lower than 2 was not investigated. Also, half of the area covered by the holes ranged from 1.28×10^{-4} to $2.57 \times 10^{-4} \text{m}^2$, while the cross-sectional area of the cavity (measured perpendicular to the streamwise direction) was $9.10 \times 10^{-4} \text{m}^2$. Thus, the area formed by the depth of the cavity was 3.5-7.1 times larger than the area through which air would flow in or out of the cavity. These two factors make it that the depth of the cavity is considered to be sufficient for the proper working of the cavity.

Four such plates, varying in hole diameter and porosity of their surface, were tested. An overview of the plates' characteristics is shown in Table 3.1. In addition to these, a dummy plate was tested, which had no holes and no cavity. A cross-section of the set-up of the test section with a wedge and plate installed is shown in Figures 3.2a) and b), the first of which shows the 5° wedge and the second the 8.8° wedge. Shown are also the distances the wedge's tips are removed from the plate, which have been adjusted so as to allow the oblique shock from each wedge to impinge on the porous region. The 11 cases which together comprise the test matrix, consisting of the 4 plates and a dummy plate, tested for 2 different wedges, as well as a configuration testing the dummy plate without a wedge, are shown in Table 3.2. The first case is one where no shock generator and the dummy plate was installed. This case's measurements were used for the study of the undisturbed boundary layer in Chapter 4, but no other significant results of it are used in this report.

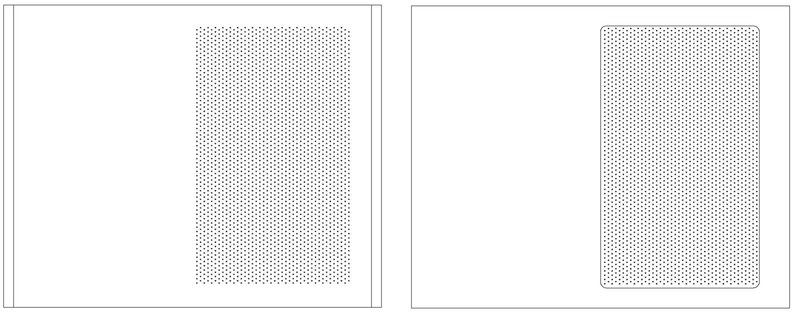

Figure 3.3: Top (left) and bottom (right) views of one of the 4 plates.

Plate #	Hole diameter [mm]	Porosity [%]
1	0.5	5
2	1.0	5
3	1.5	5
4	1.0	2.5

Table 3.1: Characteristics of the 4 different plates

Case #:	Wedge Angle [°]:	Plate:
1	N/A	Dummy
2	5.0	Dummy
3	5.0	1
4	5.0	2
5	5.0	3
6	5.0	4
7	8.8	Dummy
8	8.8	1
9	8.8	2
10	8.8	3
11	8.8	4

Table 3.2: Test matrix

The 5.0° and 8.8° wedges were used because the first angle causes a pressure jump large enough to cause a significant interaction, but just not large enough to cause separation of the turbulent boundary layer, while the second angle will cause separation. This is shown by Babinsky and Harvey (2011), who provided an equation for the necessary pressure jump for shock-induced separation of a turbulent boundary layer:

$$\frac{p_1}{p_0} = 1 + 6\frac{\gamma}{2}M_0^2\sqrt{\frac{2C_{f_0}}{(M_0^2-1)^{\frac{1}{2}}}}$$

Whereby p_1/p_0 is the pressure jump caused by a shock. Using the flow properties of Kallarbail (2016) as an example (an investigation of which the conditions are similar to the present one), the necessary pressure jump would have to be 1.79. The pressure jump caused by the incident and reflected shocks of the 5.0° and 8.8° wedges are 1.71 and 2.06 respectively, showing them to be just under and well above the necessary separation threshold respectively.

Concerning the porosity of the plates, 3 of them were set at 5%, a value similar to that of the similar investigation of Bur et al. (1998) (which was 5.67%) and one at 2.5%. This different porosity was chosen to be able to get an indication of the effect of varying porosity by a factor of 2, and 2.5% was chosen instead of 10% because this requires less holes and a shorter production time. Concerning the size of the holes, Bur et al. (1998) obtained significant flow through holes of 0.3mm diameter. The facilities present at Delft University of Technology could not produce holes smaller than 0.5mm in diameter. In order to see how this varied with a linear increase in hole size, diameters of 1.0mm and 1.5mm were also produced.

A few formulas to predict the flow through holes faced with a certain pressure difference could be applied to show the flow achieved through the holes would be significant. Three of these are Bohing & Doerffer's law (1995), the Isentropic law (Breitling, 1985) and Poll's law (1992).
With Bohning and Doerffer's law, a correlation is provided for the Mach number flowing through a hole in a plate covering a drop in pressure, from which one can find the corresponding velocity through that hole:

$$M_{hole} = 1.2\left(\frac{\Delta p}{p_0}\right)^{0.55}$$

$$v_w = p_{cor}\frac{M_{hole}\sqrt{\gamma R T_0}}{\sqrt{1+\frac{\gamma-1}{2}M_{hole}^2}}$$

whereby p_0 is the pressure before the pressure drop, and p_{cor} is the porosity of the plate. The Isentropic law is called so because it assumes isentropic flow through the holes, and is of the form:

$$v_{hole} = \sqrt{\frac{2\gamma}{\gamma-1}\frac{p_b}{\rho_b}\left[\left(\frac{p_a}{p_b}\right)^{\frac{\gamma-1}{\gamma}}-1\right]}$$

Finally, Poll's law is of the form:

$$Y = \frac{1}{K}(40.7X + 1.95X^2)$$

Whereby Y and X are defined by:

$$Y = \frac{(p_c - p)d^4}{\rho\nu^2 t^2}$$

$$X = \frac{m_f}{\mu e}$$

Whereby p_c is the pressure in the cavity, e is the plate thickness, d is the hole diameter, k is a coefficient related to inaccuracies in the hole's shape (and is in this case assumed to be 1, the value for a perfectly cylindrical hole, for simplicity), and $m_f = \rho\pi d^2 v_{hole}/4$, the mass flow through a hole. The above equation can be solved for X, from which v_{hole} can be found. The velocity through a hole can be related to the transpiration velocity of the entire porous surface by multiplying v_{hole} by the porosity percentage.
The above formulas predicted the v_w of the investigation of Bur et al. (1998) (shown in Figure 5.28 in chapter 5) with an average accuracy of 17.2%, 35.9% and 18.6% respectively. Based on these formulas, vertical velocities for the flow through the holes have been predicted as shown in Table 3.3. To make these predictions, a simple model has been assumed whereby an inviscid

oblique shock impinges exactly halfway along the porous section and the pressure rise occurs there discontinuously. This explains why one single velocity is predicted for each half, as this mainly depends on the pressure difference under and above the cavity. Since hole size is not a factor in Bohning and Doerffer's formula and the Isentropic law, some of the plates have the same values. The ratio of the largest vertical velocity from the plates to freestream velocity, v_w/U_∞, was 0.019 in the case of Bur et al. (1998), and 0.018, 0.031 and 0.025 in the case of these predictions, for each formula respectively. Based on this similarity, the present design is expected to give valuable results.

			Bohning and Doerffer:		**Isentropic law:**		**Poll's law:**	
Wedge angle [°]	Hole diameter [mm]	Porosity [%]	v_w upstream [m/s]	v_w downstream [m/s]	v_w upstream [m/s]	v_w downstream [m/s]	v_w upstream [m/s]	v_w downstream [m/s]
5.0	0.5	5.0	8.97	-7.95	10.4	-7.78	6.29	-6.29
5.0	1.0	5.0	8.97	-7.95	10.4	-7.78	6.34	-6.34
5.0	1.5	5.0	8.97	-7.95	10.4	-7.78	6.35	-6.35
5.0	1.0	2.5	4.48	-3.98	5.20	-3.89	3.17	-3.17
8.8	0.5	5.0	12.7	-10.6	15.4	-10.2	8.95	-8.95
8.8	1.0	5.0	12.7	-10.6	15.4	-10.2	9.00	-9.00
8.8	1.5	5.0	12.7	-10.6	15.4	-10.2	9.01	-9.01
8.8	1.0	2.5	6.37	-5.32	7.69	-5.09	4.50	-4.50

Table 3.3: Predicted vertical flow through holes based on 3 formulas

3.4 Measurement techniques

3.4.1 Schlieren visualization

Schlieren visualization is a method to visualize the density gradients in a flow as varying tints of gray. The underlying principle which it makes use of is that the density of a medium affects the way light is refracted through it. As the following equation shows, the refractive index n represents the relation between the speed of light in a vacuum c_0 and that in the specific medium c, and can be related to the density of the medium ρ and the Gladstone-Dale constant K:

$$n = \frac{c_0}{c} = 1 + K\rho$$

In a set-up as shown in Figure 3.4, light from a light source travels through a pin hole (to make the light source more properly defined), gets reflected by a mirror, passes through the test section, gets reflected by another mirror, and passes by a knife edge before it falls on the camera's sensor. Changes in density in the test section cause the light to refract differently, and this refraction causes either more or less of the light to be blocked by the knife edge and on the sensor. Hereby spatial gradients in density cause changes in grayscale in the final image obtained by the sensor. An example of an image obtained by this method is shown in Figure 3.5. At the top of the image, the wedge is visible, from which the incident shock emanates, and at the bottom-right, a reflecting shock can be seen. Density changes over the oblique shocks, and in the boundary layer can be visualized by their changes in grayscale.

3.4.2 Particle Image Velocimetry

The PIV method is one which can be used to obtain the velocity field in a flow. Particles are added to the flow and travel with it, and a laser sheet illuminates them along a plane at specific intervals. The images of the illuminated planes are captured by a camera, and together with the time interval between consecutive images, are used to obtain a velocity field. This is done by dividing the image into so-called *interrogation windows*, and finding the shift in pixels for which the cross-correlation is highest between consecutive images.

The laser first emitted its light as a concentrated beam, which was concentrated into a sheet by the use of a Laserprobe, shown in Figure 3.7. Some of the other important characteristics

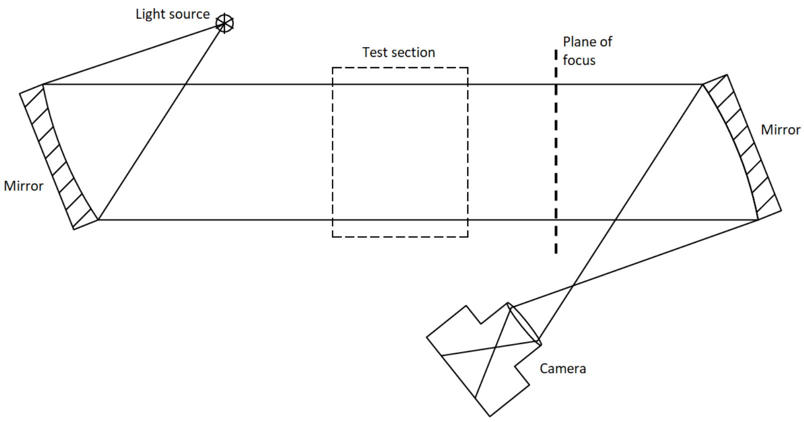

Figure 3.4: Top view of the Schlieren set-up. From Scarano (2013).

Figure 3.5: Example of a Schlieren image

of the PIV measurement campaign are shown in Table 3.4. The field of view (FOV) of each of these camera's and what part of the set-up they captured is shown in Figure 3.6. Each camera captured a region of 50mm wide and 38.05mm high. Because the cameras each have a resolution of 1624×1236, this means the images have a pixel-to-mm ratio of 32.5.

3.5 Data processing methods

3.5.1 Schlieren image processing

The camera used to obtain Schlieren images for the preliminary investigation (to determine in what configuration the shock impinged on the porous surface) was a LaVision BobCat camera. The images from this preliminary investigation did not need to be processed further than by simply inspecting them visually. Later, the Schlieren method was used again with a LaVision Photron high-speed camera. The images captured with the high-speed camera were intended to be used to analyze the unsteadiness of the reflected shocks. However, upon examining the images it turned out the flow field was too complex for a computational algorithm to identify the reflected shock accurately over a large set of images. Namely, compression waves emanated from the holes in the porous plates, which coalesced together to form the reflected shock, and an algorithm which correctly identified the reflected shock instead of other compression waves could

Characteristic	Value
Cameras used	3 × LaVision BobCat
Focal length of lenses	60mm
Aperture size ($f_{\#}$)	5.6
Image resolution	1624×1236
Field of view captured	50mm×38.05mm
Pixels per mm	32.5 pxmm^{-1}
Laser type	Quantel Evergreen Nd:YAG
Laser sheet thickness	1mm
Pulse separation time δt	1μs
Particle type	Di-Ethyl-Hexyl-Sebacat (DEHS)
Particle response time (τ_p)	1.92μs

Table 3.4: PIV measurement characteristics

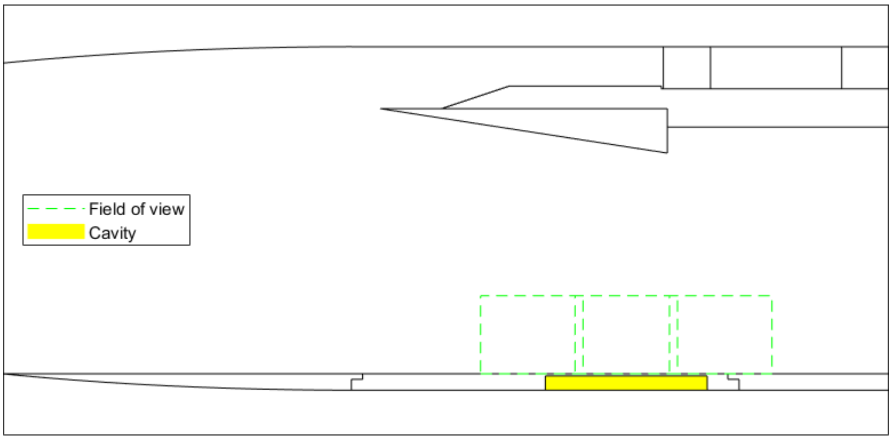

Figure 3.6: Fields of view captured by the PIV method

not be produced. However, in the images collected, the reflected shock could still be identified in individual images, and this information was used to calculate the interaction length. Hereby, the reflected shock was identified as one at the top of the image where numerous smaller shocks coalesced into, as in the diagram of Figure 2.2 in Chapter 2. If this was not visible, a line was plotted through where the band of compression waves was the most dense. A line was also drawn through the downstream edge of the incoming shock, and the interaction length was calculated as the length between the points at which the lines intersected the bottom wall. An example of how this was done for a single image is shown in Figure 3.8.

3.5.2 PIV processing

The images were captured and pre-processed with the help of LaVision DaVis 8.4.0. The first operation done was that at each pixel of the images captured, the minimum brightness found at that pixel's location in its set of (approximately 300) images was subtracted from it. This meant that the brightness at each pixel was relative to the lowest brightness found at that point over the whole set, which compensated, for example, an uneven distribution of the laser sheet's illumination. Also, a region at the bottom of the image was 'masked' i.e. designated as a region where no velocity calculation needed to take place. In this way it could be prevented that the plate, which occasionally showed reflections of particle contours, was not mistakenly identified as part of the flow. The velocity was then calculated by cross-correlating interrogation windows, as explained earlier, but in this case, using a multi-grid approach (Raffel, Willert, Wereley and Kompenhans, 2007) with the large interrogation windows being 96×96 pixels and the smaller being 24×24. After obtaining a velocity field, the universal outlier detection algorithm (Westerweel and Scarano, 2005) was applied to remove vectors that were deemed 'outliers'. To sum this algorithm up shortly, it identifies vectors as outliers if they differ from mean value of the

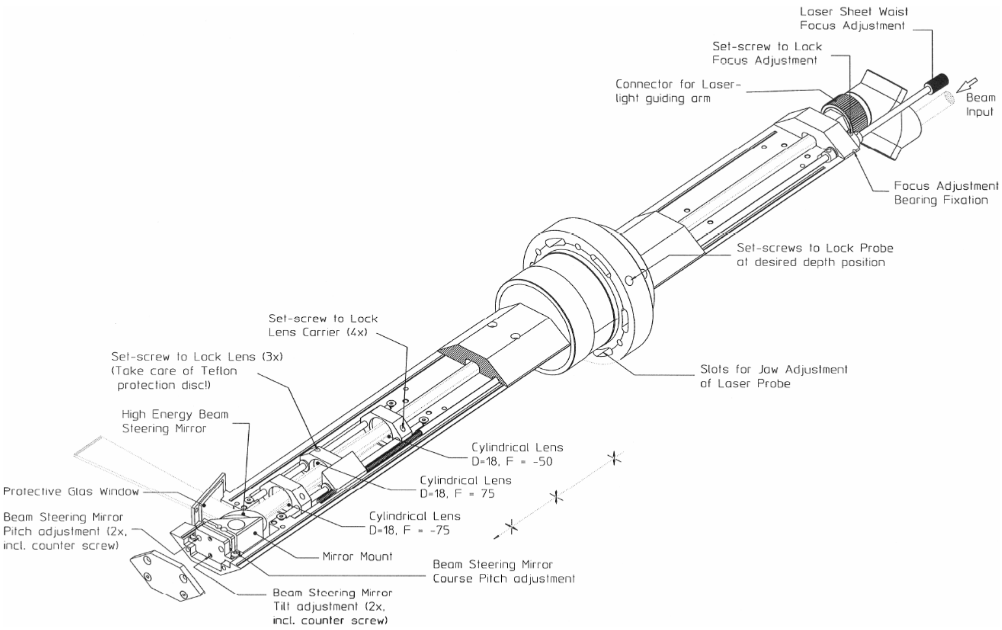

Figure 3.7: Diagram of the Laserprobe used to focus the laser's beam into a sheet (Donker Duyvis, 2005)

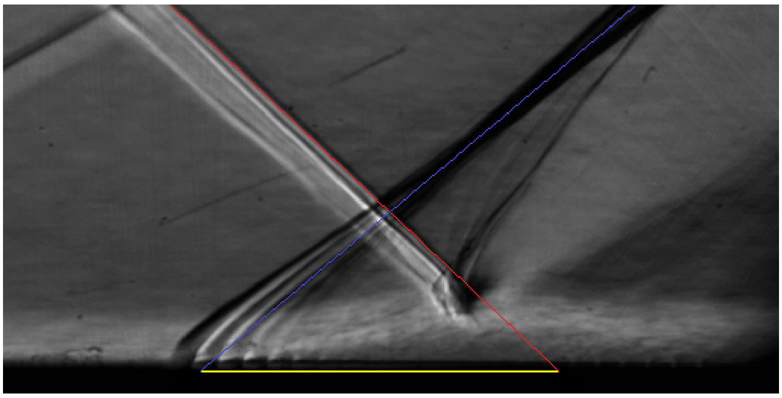

Figure 3.8: Interaction length (yellow) calculated from lines drawn through the incident shock (red) and reflected shock (blue)

surrounding vectors (in this case, the 24 vectors of the surrounding 5×5 matrix) by a threshold value. In this case, the universal outlier detection algorithm was applied with a threshold value of 2.

After the above was done with DaVis, further processing was done with Matlab. To calculate the mean velocity fields, for each vector, the average was calculated over all (approximately 300) images in the set. While this was done, outliers were once again identified, but instead of identifying them relative to surrounding vectors, this was now done relative to the mean value of the set, whereby vectors more than 3 standard deviations away from the mean were deemed outliers. This removed approximately 0.27% of the vectors. Calculating this required running a program past the 300 images twice, once calculating the mean and root mean square, and the second time, removing outliers and calculating the mean again. During this second run, the percentage of vectors with reverse flow, as well as the distribution of various turbulence stresses, were also calculated. These processed results are shown in Chapters 4, 5 and 6.

The PIV results were non-dimensionalized in order to make them more representative and easy to compare with other cases. Distances in x and y were divided by $\delta_{99,0}$ (the boundary layer height at which the streamwise velocity is 99% of that of the freestream), found upstream of the interaction (signifying the '0'). The way this was found is explained in Chapter 4. The origin of the coordinate system was set at the point of impingement of the incoming oblique shock. The velocities were divided by the freestream velocity.

3.5.3 Boundary layer integral parameters

One of the desired results was the spatial variation of displacement thickness (δ^*), momentum thickness (θ) and shape factor (H) over the cavity, to compare the results to that of Bur et al. (1998). The equations for δ^* and θ are as follows:

$$\delta^* = \int_0^\infty \left(1 - \frac{\rho u}{\rho_e U_e}\right) dy \tag{3.1}$$

$$\theta = \int_0^\infty \frac{\rho u}{\rho_e U_e} \left(1 - \frac{u}{U_e}\right) dy \tag{3.2}$$

Shown above are the compressible forms, but in section 4.3, they have also been applied in their incompressible form, to be able to compare the result to other investigations. The incompressible form discards changes in density, so $\rho = \rho_e$. Although the integrals in Equations 3.1 and 3.2 are shown to go to infinity, these are normally integrated up to a height at which they converge to a constant value. The height up to which this had to be done was not a straightforward matter, because in the case of the region over the cavity, convergence could not be expected when increasing the height up to which was integrated because of the oblique shock found above it. In order to determine a height, firstly, the value of du/dy was found at the height of δ_{99} of the undisturbed boundary layer upstream. This was determined to be approximately 0.08, in units of u/U_e per δ_{99}. Next, a contour was plot along which height this value was found. This contour was smoothed out by fitting a curve to it, which served as the basis for the height to which to integrate for δ^* and θ. Plots of the curves for each case are shown in Appendix C.

3.5.4 Density within the boundary layer

To calculate the displacement and momentum thicknesses' compressible form, density within the boundary layer as a function of free-stream density, ρ/ρ_e is calculated by a derivative of the Crocco-Busemann relation:

$$T = T_e + r\left(\frac{u_e^2 - u^2}{2c_p}\right)$$

Whereby r is the recovery factor. Because there is no significant pressure gradient in the y-direction, $\rho RT = \rho_e RT_e \Rightarrow \frac{T}{T_e} = \frac{\rho_e}{\rho}$:

$$\frac{\rho}{\rho_e} = \left(1 + r\frac{\gamma - 1}{2}M_e^2\left(1 - \left(\frac{u}{U_e}\right)^2\right)\right)^{-1}$$

Whereby the characteristics at e, of the freestream, were found at the heights discussed in the previous subsection. To be able to plot the velocity fluctuations in the boundary layer in section 4.4, ρ/ρ_w had to be calculated, and another derivative of the Crocco-Busemann relation was used:

$$T = T_w + (T_{aw} - T_w)\frac{u}{U_e} - r\frac{u^2}{2c_p}$$

the fact that the adiabatic wall temperature is calculated by:

$$T_{aw} = T_e(1 + r\frac{\gamma - 1}{2}M^2)$$

(whereby r is the recovery factor), and the assumption that $T_{aw} = T_w$, the adiabatic wall temperature is the wall temperature. The last assumption is assumed to be valid because the wind tunnel only runs for short periods of time, so heat transfer between the wall and the surroundings is minimal. Hence:

$$\begin{aligned}
T = T_w + (T_{aw} - T_w)\frac{u}{U_e} - r\frac{u^2}{2c_p} \\
T = T_w - r\frac{u^2}{2c_p} \\
\frac{T}{T_w} = 1 - \frac{ru^2}{2c_p T_{aw}} \\
\frac{T}{T_w} = 1 - \frac{ru^2}{2c_p T_e(1 + r\frac{\gamma-1}{2}M_e^2)}
\end{aligned}$$

Because there is no significant pressure gradient in the y-direction, $\rho RT = \rho_w RT_w => \frac{T}{T_w} = \frac{\rho_w}{\rho}$:

$$\begin{aligned}
\frac{\rho_w}{\rho} = 1 - \frac{ru^2}{2c_p T_e(1 + r\frac{\gamma-1}{2}M_e^2)} \\
\frac{\rho}{\rho_w} = \left(1 - \frac{ru^2}{2c_p T_e(1 + r\frac{\gamma-1}{2}M_e^2)}\right)^{-1}
\end{aligned}$$

Chapter 4

Boundary Layer Study

4.1 Introduction

In this section, the upstream boundary layer of an undisturbed case, without a wedge and with the dummy plate installed, is analyzed and compared to the upstream undisturbed boundary layer of similar investigations. This is done to give further assurance that the conditions created in the windtunnel were representative. In section 4.2, the velocity vs. height plot of this boundary layer is shown and compared. Then, the wall-friction velocity, as well as some other important parameters, are found and compared. Finally, the velocity fluctuations in the boundary layer are compared with those of other investigations.

4.2 Velocity profile

In Figure 4.1 the velocity profile, a plot of y vs. u/U_∞ is shown, which was obtained at a distance of 33.11mm upstream from the start of the cavity. For comparison, results from two similar investigation are shown (Kallarbail, 2016; van Pelt, 2013). The set-up used by van Pelt is similar to the present one because it also used inserts at the floor of the test section, and from the figure it is clear that its velocity profile is more similar to that of the present study as well.

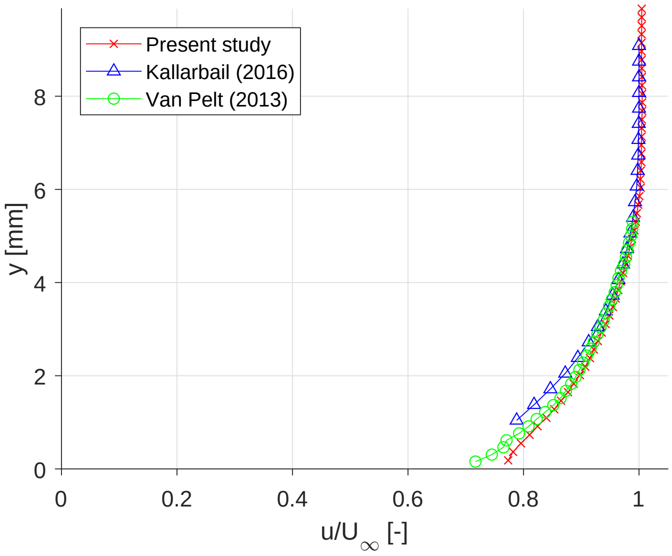

Figure 4.1: Velocity profiles of the undisturbed boundary layer

4.3 Boundary layer parameters

Next, the wall-friction velocity u_τ was determined. To do so, plots were made of u^+ vs. y^+ for a range of different u_τ, and it was sought for which u_τ the plotted curve obeyed the van Driest log-law the most. The van Driest log-law 1956 is expressed by:

$$u^+ = \frac{1}{\kappa} ln(y^+) + B \tag{4.1}$$

Whereby $\kappa = 0.41$ and $B = 5.0$. u^+ and y^+ are expressed and derived as follows:

$$\begin{aligned} u^+ &= \frac{u_{eq}}{u_\tau} \\ u_{eq} &= \frac{U_e}{a}(\sin^{-1}(\frac{a\overline{u}}{U_e})) \\ a &= \sqrt{1 - \frac{T_e}{T_w}} \\ T_w &= T_e(1 + r\frac{\gamma-1}{2}M_e^2) \end{aligned}$$

$$\begin{aligned} y^+ &= \frac{yu_\tau}{\nu_w} \\ \nu_w &= \frac{\mu_w}{\rho_w} \\ \rho_w &= \rho_e\frac{T_e}{T_w} \\ \rho_e &= \frac{\rho_0}{(1 + \frac{\gamma-1}{2}M_e^2)^{\frac{1}{1-\gamma}}} \end{aligned}$$

In the above relations, a recovery factor r of 0.89 was used. M_e, the free-stream Mach number was calculated from the velocity by:

$$\begin{aligned} T_e &= T_0 - \frac{U_e^2}{2c_p} \\ M_e &= \frac{U_e}{\sqrt{\gamma R T_e}} \end{aligned}$$

Hereby M_e was found to be approximately 1.86. Other investigations report it being 2.0, and this is likely due to the fact that the present investigation used inserts as well as that others likely just assumed it to be 2.0 because they used the wind tunnel blocks which correspond to that Mach number. The fact that inserts were used reduces the cross-sectional area of the test section, which also reduces the Mach number there. Through isentropic calculations, the Mach number when inserts are used is estimated at 1.94, if the Mach number without inserts would be exactly 2.0.

In Figure 4.2 the plot of u^+ vs. y^+ is shown together with the van Driest log-law for the u_τ which was eventually found, which was 19.9m/s. Also shown are the u^+ vs. y^+ data points for a similar investigation. How the value of u_τ, as well as of some other conditions characteristic of the boundary layer and the set-up, compares to that of similar investigations also performed in the ST-15 at Mach 2.0, are shown in Table 4.1. The displacement and momentum thicknesses and shape factor are shown both in their compressible and incompressible form, the incompressible forms being shown so that the values can be compared to those of other investigations, for which a compressible result of these parameters wasn't mentioned. The parameters which deviate the most from the other studies shown are the incompressible displacement and momentum thickness. A possible explanation for this is that the method by which this is calculated depends on a few assumptions which could have been made differently in other investigations. For example, the integral in Equations 3.1 and 3.2 was performed up to a height dictated by the curves in Appendix C for the current investigation, and the U_e used was also the u found at this height, but other investigations may have done this differently.

The δ_{99} shown in Table 4.1 is the boundary layer height, defined as the height at which 99% of the free-stream velocity is found, and it is used in the rest of the report to non-dimensionalize all lengths, where it is noted as $\delta_{99,0}$ to make clear it was obtained from the undisturbed case.

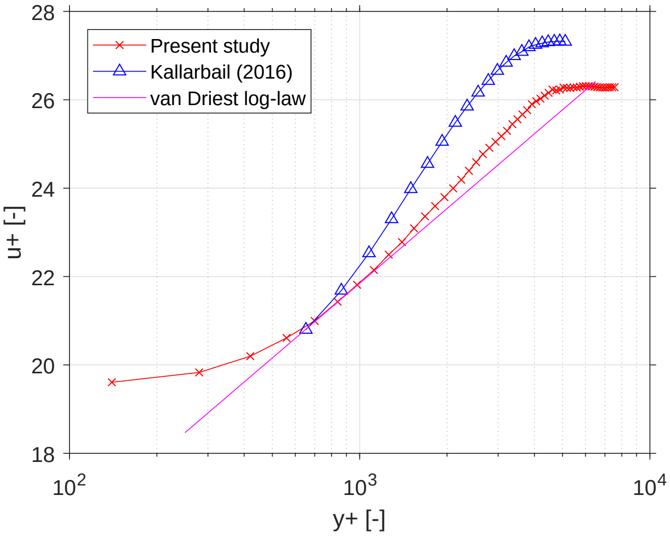

Figure 4.2: u^+ vs. y^+ and the log-law line

	Present Study	Giepman (2016)	Kallarbail (2016)	Tambe (2017)
M_∞ [-]	1.86	2.0	2.0	2.0
C_f [-]	2.11×10^{-3}	1.9×10^{-3}	1.9×10^{-3}	1.9×10^{-3}
τ_w [N/m^2]	259	237	211	N/A
T_0 [K]	283	290	278	266
U_∞ [m/s]	483	524	492	487.5
u_τ [m/s]	19.9	20.8	19.6	19.8
δ_{99} [mm]	5.06	5.2	5.2	5.2
δ^* [mm]	0.722	N/A	N/A	N/A
δ^*_{inc} [mm]	0.491	0.63	0.67	0.663
θ [mm]	0.390	N/A	N/A	N/A
θ_{inc} [mm]	0.420	0.52	0.51	0.524
$H[-]$	1.85	N/A	N/A	N/A
$H_{inc}[-]$	1.17	1.2	1.3	1.26
Re_∞ [1/m]	4.49×10^7	4.22×10^7	4.35×10^7	4.62×10^7
$Re_{\theta_{inc}}$ [-]	1.89×10^4	2.18×10^4	2.2×10^4	2.4×10^4

Table 4.1: Upstream boundary layer parameters obtained in present study and similar investigations

4.4 Velocity fluctuations

Finally, the velocity fluctuations in the boundary layer were compared to the velocity fluctuations in similar boundary layers. To be able to compare the velocity fluctuations with those of other investigations, including the results of Klebanoff (1955) for incompressible flow, the non-dimensional $\sqrt{\rho/\rho_w}\sqrt{\overline{u'}}/u_\tau$ was plotted, for the streamwise as well as the wall-normal directions. Hereby, the density within the boundary layer was calculated as explained in subsection 3.5.4. The results are shown in Figure 4.3, whereby it is visible that the velocity fluctuations of the present investigation are distributed comparably along the boundary layer's height.

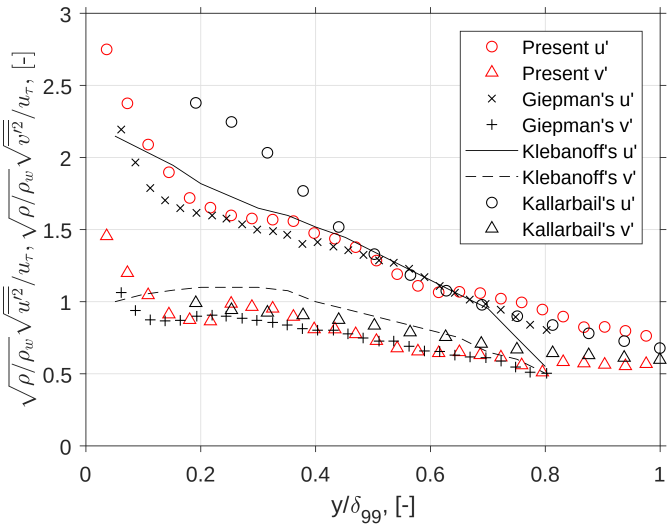

Figure 4.3: Velocity fluctuations across the boundary layer's height

Chapter 5

Mean flow field

5.1 Introduction

After having verified the accuracy of the undisturbed boundary layer in the previous chapter, the present and next chapters discuss the full range and significance of the PIV and Schlieren measurements. The present chapter discusses the results pertaining to the steady characteristics of the flow field. First, the Schlieren images are shown and it is discussed what phenomena can be observed. Secondly, the interaction length, which has been calculated from the Schlieren images, is discussed. Subsequently some results produced by the PIV measurements are discussed: the mean velocity fields, the percentage of backflow and how this is spatially distributed, and the separation area per case. Subsequently, some specific results are shown which are compared to those of the investigation by Bur et al. (1998): the displacement thickness, momentum thickness, shape factor and vertical velocity over the cavity. Finally, the conclusions that can be taken from these results are summed up.

5.2 Description of flow fields

5.0° wedge, dummy plate

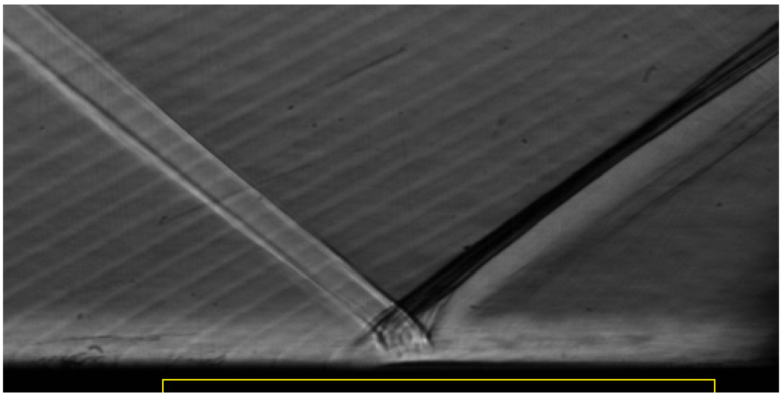

Figure 5.1: Schlieren image for 5.0° wedge, dummy plate. Location where cavity would be is marked in yellow.

A Schlieren image of the case of the 5.0° wedge and the dummy plate is shown in Figure 5.1. The flow runs from left to right, and the oblique shock coming from the wedge can be seen to run from the top left to the bottom of the image. The angle of the oblique shock with the horizontal is 39.9°, which is slightly higher than what the inviscid calculations predict, 37.1°. An explanation for this could be that the freestream Mach number is even lower than what was calculated in the previous chapter. When the oblique shock hits the bottom wall, a standard oblique shock wave-boundary layer interaction can be seen to take place, with an expansion fan following the reflected shock, seen as a bright band to the right of a dark band. Slightly more variations in grayscale can be seen in the downstream boundary layer compared to the upstream one, implying more large-scale fluctuations in the downstream boundary layer due to the interaction. The remaining faint diagonal lines that can be seen to run from the bottom left to the top right upstream of the interaction are Mach lines emanating from small, regularly spaced aberrations in the surface of the dummy plate, arising from its production method. No significant boundary layer growth can be observed in the image.

8.8° wedge, dummy plate

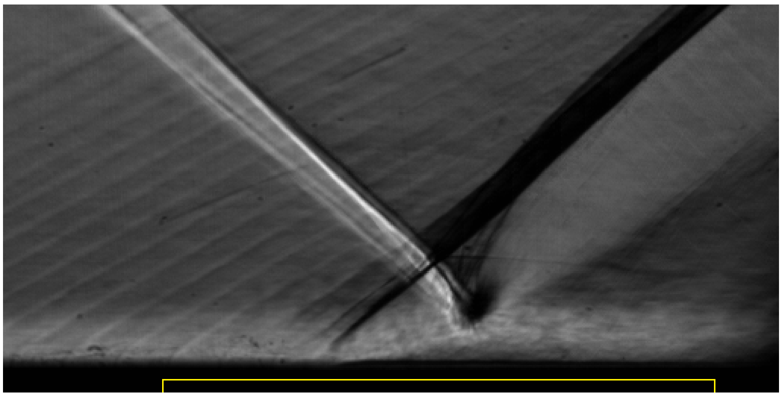

Figure 5.2: Schlieren image for 8.8° wedge, dummy plate. Location where cavity would be is marked in yellow.

In Figure 5.2, a Schlieren image of the case with the 8.8° wedge and the dummy plate is shown. The angle the oblique shock makes is 43.3°, which is larger than for the 5.0° wedge, but also larger than what is predicted by inviscid calculations for the 8.8° wedge, namely 41,1°. The point at which the incident shock impinges cannot be compared to Figure 5.1, as the wedge has been moved in the x- and y-direction. It can be seen that the interaction length has increased, by the fact that the reflected shock emanates more upstream (relative to the incident shock's impingement point) than the 5.0° case. This is apparently due to the increase in shock strength due to the higher wedge angle. Also, the incident shock stops at a higher height, which means the sonic line is found at a higher point. This is likely due to the boundary layer slowing down and increasing in height more than in the 5.0° case. The increased boundary layer height downstream due to the interaction can also be observed from the slightly larger height of the light downstream horizontal band. Also, more significant large-scale fluctuations in the downstream boundary layer can be observed than was the case in Figure 5.1, and slight boundary layer growth compared to the upstream case. Finally, the reflected shock angle can be seen to have increased.

5.0° wedge, porous plates

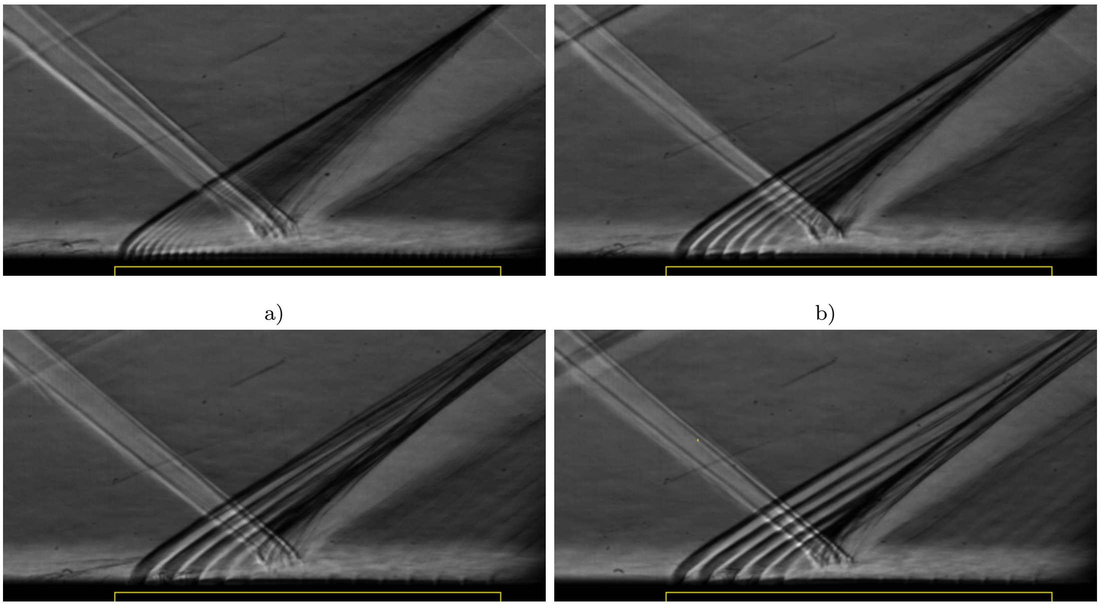

a)

b)

c)

d)

Figure 5.3: Schlieren images for 5.0° wedge, porous plate cases: a) 0.5mm holes & 5% porosity plate, b) 1.0mm holes & 5% porosity plate, c) 1.5mm holes & 5% porosity plate and d) 1.0mm holes & 2.5% porosity plate. Location of cavity is marked in yellow.

The cases with the 5.0° wedge and porous plates are shown in Figure 5.3. Firstly, 5.3a) shows the case with the plate with 0.5mm holes and 5.0% porosity. The incoming oblique shock has the same angle as for the dummy plate case with the 5.0° wedge, as this part of the region is unaffected by the difference in plate. As flow encounters the region above the porous plate and cavity, it first seems to encounter a strong compression shock (the strength being made clear by the darkness and width of the wave) emanating from the start of the cavity. The initial compression shock is likely due to flow emanating out of the holes of the cavity. Namely, the flow out of the holes increases the boundary layer thickness, making the streamlines (and thus also the sonic line) curve upwards, which makes the incoming flow experience an effective deflection upwards, causing a compression wave. After this initial compression wave, smaller compression waves can be seen to emanate from the holes. This is likely because each hole enforces the same effect again, but at a lesser magnitude, because the upward deflection of the sonic line is less, and because the Mach number decreases with each shock.

Figures 5.3b), c) and d) show the remaining cases for the 5.0° wedge, with holes of larger diameter or with lower porosity than the previous case. Compared to the previous case, the shocks are seen with more distance in between them (which is due to the higher spacing between the holes), and with a higher intensity due to the fact that they're darker. Also, in these cases it is visible that at the downstream end of the fan of compression shocks, these coalesce into a single dark line which forms the reflected shock.

For all subfigures of 5.3, no significant boundary layer growth can be observed. Also, it is visible that there are less variations in grayscale in the downstream boundary layer than for the dummy plate case, implying less velocity fluctuations.

8.8° wedge, porous plates

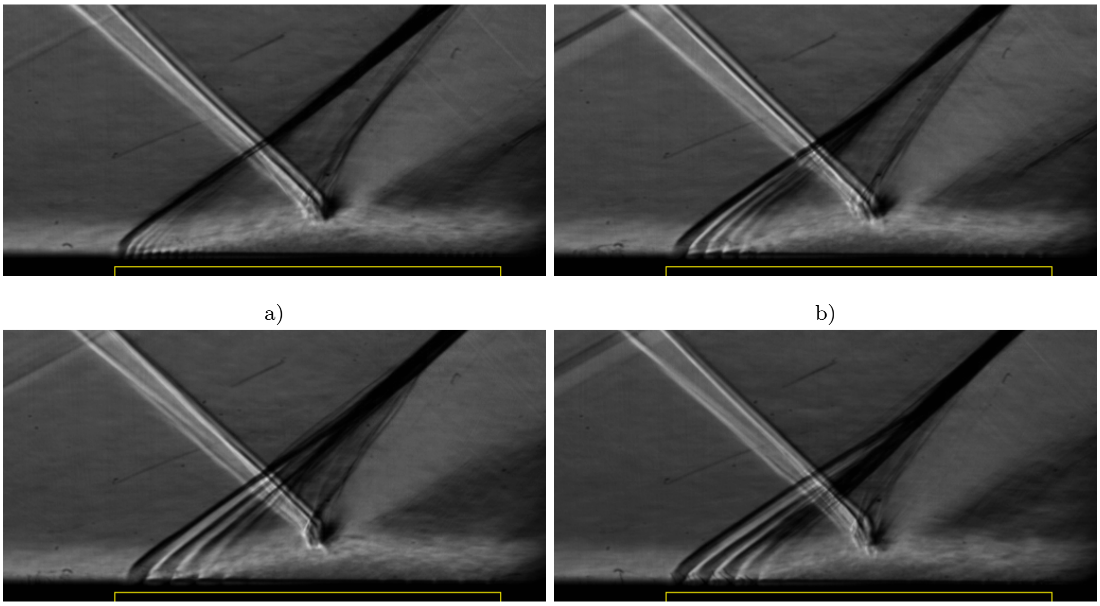

a) b) c) d)

Figure 5.4: Schlieren images for 8.8° wedge, porous plate cases: a) 0.5mm holes & 5% porosity plate, b) 1.0mm holes & 5% porosity plate, c) 1.5mm holes & 5% porosity plate and d) 1.0mm holes & 2.5% porosity plate. Location of cavity is marked in yellow.

In Figure 5.4, the same cases are shown as in Figure 5.3, but now with the 8.8° wedge. In the images, a shock can be seen to arise in the same way when the flow encounters the first hole, seemingly with the same angle as for the 5.0° wedge, which is understandable as this part of the flow is not influenced by the wedge. Beyond the first shock, weaker shocks from the other holes can again be seen, albeit only visible for a few holes. After that, the flow turns subsonic, or stated otherwise, the boundary layer has decelerated so much that the sonic line grows in height significantly. The fact that subsonic flow is achieved more quickly here than for the 5.0° wedge is likely due to two reasons. Firstly, as one already knew from Chapter 2, the pressure rise from the shock is transferred to the subsonic part of the boundary layer, where it'll already cause a deceleration of the boundary layer to occur upstream. Second of all, flow of air out of the holes is likely to be higher in the upstream part of the porous section (which will cause stronger compression shocks which decelerate the flow more) because the pressure above the downstream portion of the porous plate is higher and more air flows into the plate there. One can observe that the compression shocks coming from the holes continue on for a bit further (and subsonic flow is delayed a bit further) in the case of b), c) and d) than in a), so in the case of larger hole size and lower porosity. One can also see that the compression waves emanating from the holes coalesce more into a single reflected shock, than the cases of the 5.0° wedge.

For all images, one can also observe that after the incident shock hits the sonic line, another weak shock seems to emanate off the sonic line from the point where the incident shock intersects it. Under the point where the incident shock hits the sonic line is where the boundary layer seems thickest, and it is also here that the boundary layer's seems the most gray. That the velocity gradient is so high here means the flow can have separated here, although this is impossible to tell from these images. In the downstream boundary layer, significant boundary layer growth and large-scale fluctuations can be observed.

5.3 Interaction lengths

Wedge angle [°]:	Plate :	Interaction length [mm]:
5.0	Dummy	21.5 ± 0.762
5.0	0.5mm holes, 5% porosity	34.4 ± 3.00
5.0	1.0mm holes, 5% porosity	26.7 ± 1.51
5.0	1.5mm holes, 5% porosity	26.0 ± 2.02
5.0	1.0mm holes, 2.5% porosity	26.0 ± 1.18
8.8	Dummy	36.1 ± 1.10
8.8	0.5mm holes, 5% porosity	52.8 ± 1.17
8.8	1.0mm holes, 5% porosity	50.1 ± 0.607
8.8	1.5mm holes, 5% porosity	44.2 ± 1.94
8.8	1.0mm holes, 2.5% porosity	39.5 ± 0.682

Table 5.1: Interaction lengths for each case, with 95% confidence interval shown

The interaction lengths are shown for each case in Table 5.1. The way these have been calculated has been explained in section 3.5.1. 5 images have been used to calculate the result for each case. The lines which have been drawn through the images, which have been used to produce these values, can be seen in Appendix B. The table shows, as was already clear from the images of the previous section, that interaction length is generally higher for the higher shock angle. Also, the table shows that for both wedges, the presence of a porous plate increases the interaction length for all plates tested. Concerning variation caused by the plates, it appears that interaction length decreases with increasing hole size and with decreasing porosity.

However, some care must be taken when interpreting these results. In the case where there is a porous plate, the horizontal location of the reflected shock largely seems to be influenced by the location where the holes start. In some cases, like in Figure 5.4a), the reflected shock seems completely determined by the location of the start of the holes i.e. the reflected shock emanates from the first hole. In the other porous plate cases of the 8.8° wedge, multiple holes seem to coalesce to form the reflected shock, so the location of the start of the holes isn't as decisive, although it is still the main factor. The results shown in Table 5.1 are likely very specific to the set-up, mainly the shock impingement location with respect to the start of the porous section, that has been tested.

5.4 Mean velocity fields and profiles

In Figures 5.5 to 5.14 various time-averaged velocity plots are shown for each case. Each figure shows mean velocity fields in the horizontal and vertical directions, as well as boundary layer velocity profiles found at $x/\delta_{99,0} = -5, 0, 3$ and 5.

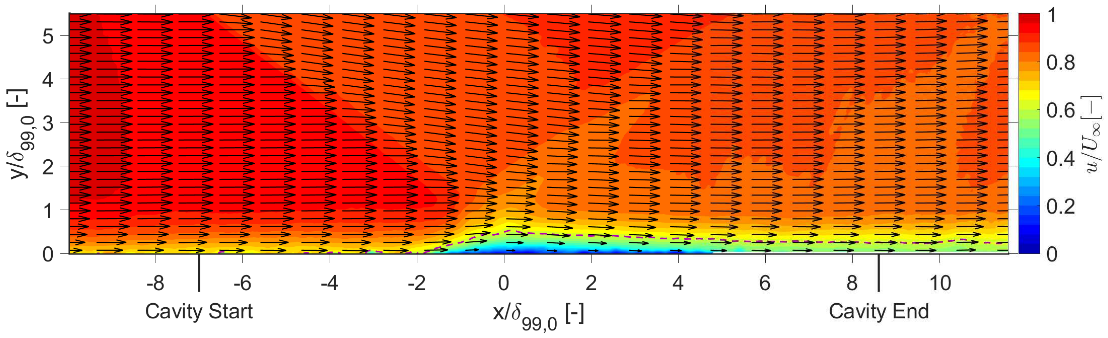

(a) Mean horizontal velocity field. Sonic line shown as dashed purple line

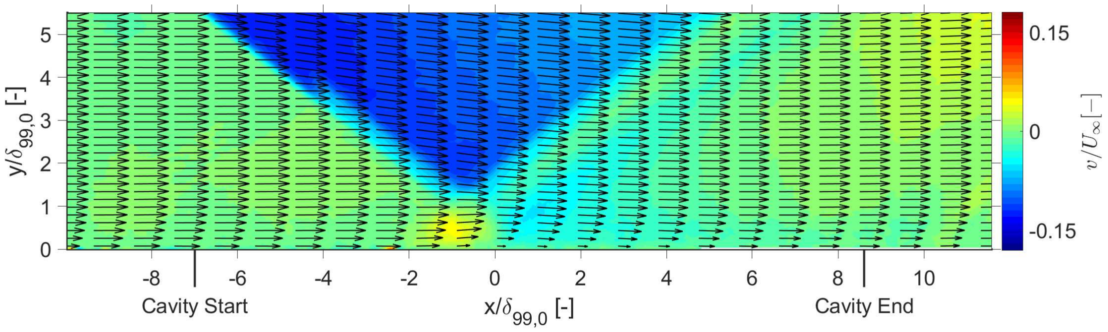

(b) Mean vertical velocity field

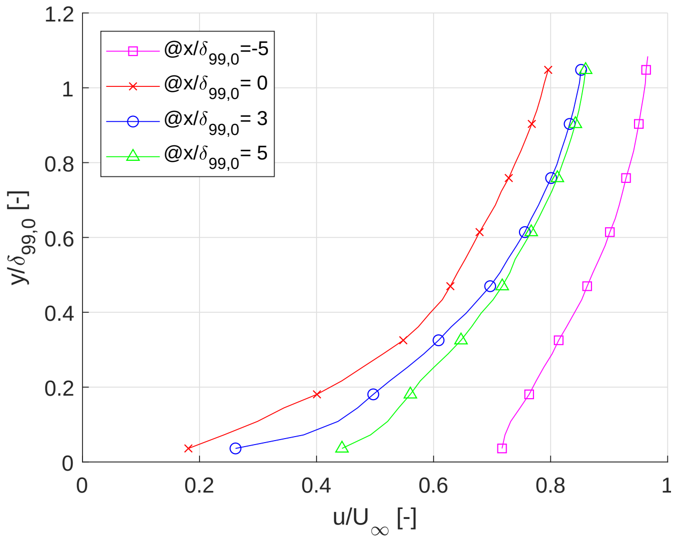

(c) Boundary layer velocity profiles

Figure 5.5: 5.0° wedge and dummy plate

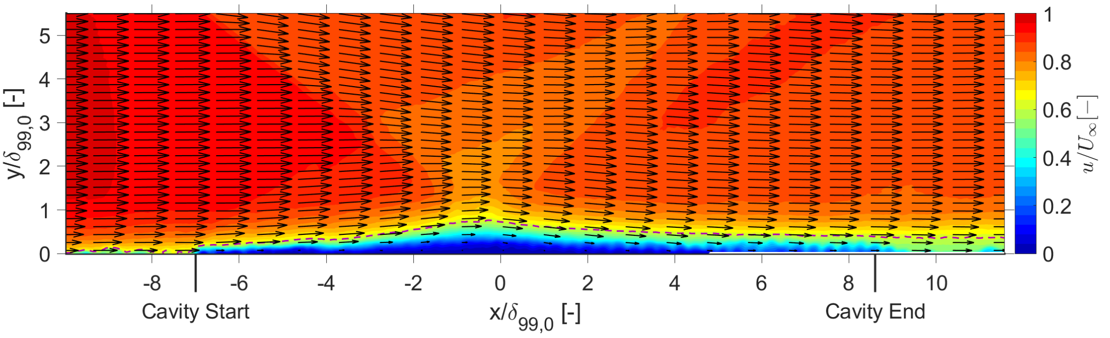

(a) Mean horizontal velocity field. Sonic line shown as dashed purple line

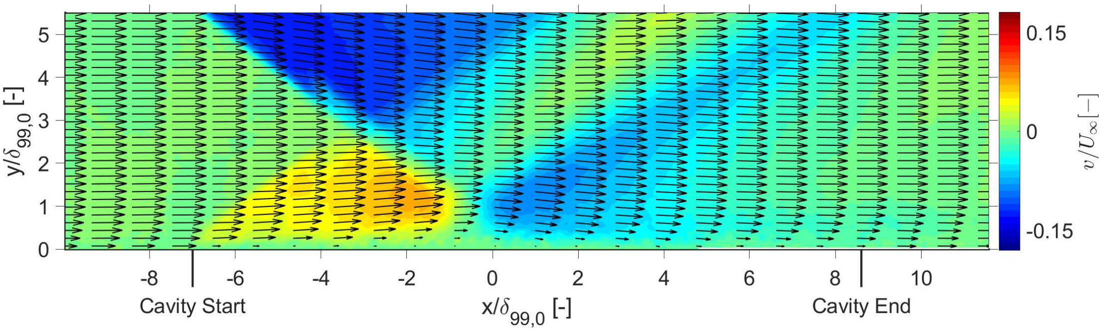

(b) Mean vertical velocity field

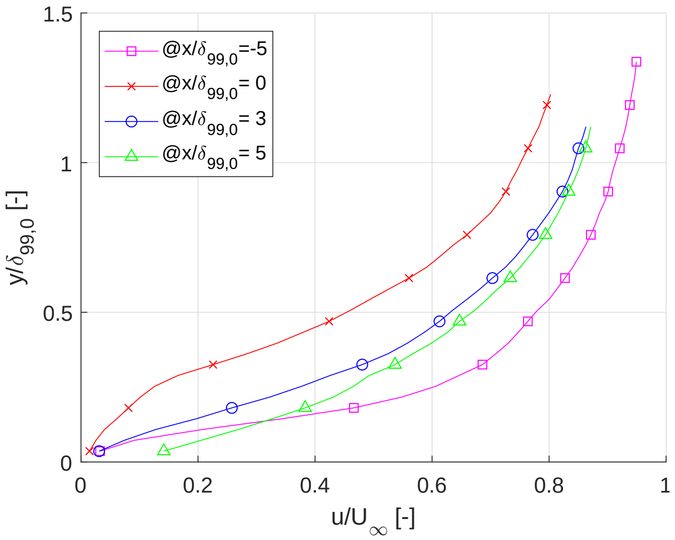

(c) Boundary layer velocity profiles

Figure 5.6: 5.0° wedge and 0.5mm holes, 5.0% porosity plate

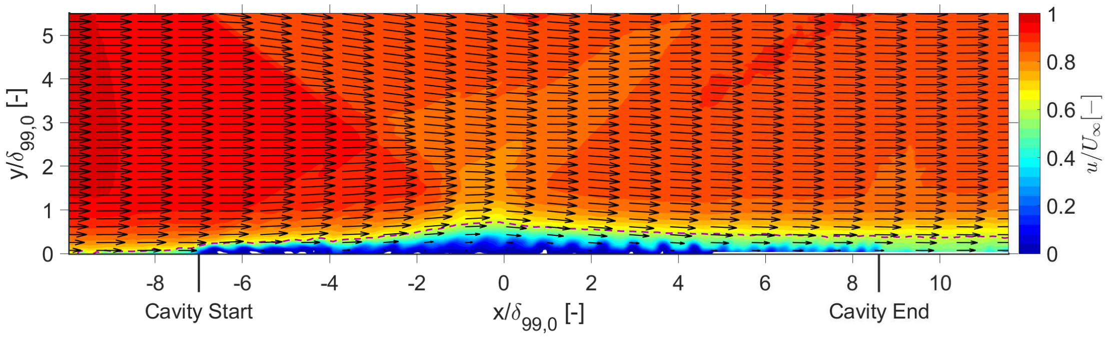

(a) Mean horizontal velocity field. Sonic line shown as dashed purple line

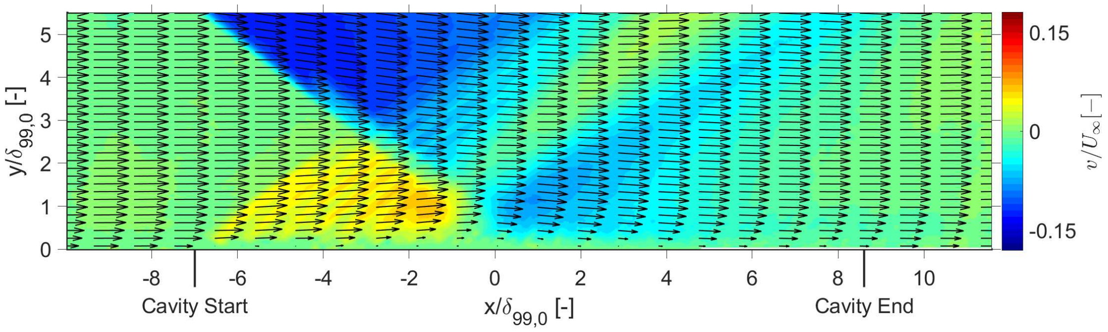

(b) Mean vertical velocity field for 5.0° wedge and 1.0mm holes, 5.0% porosity plate

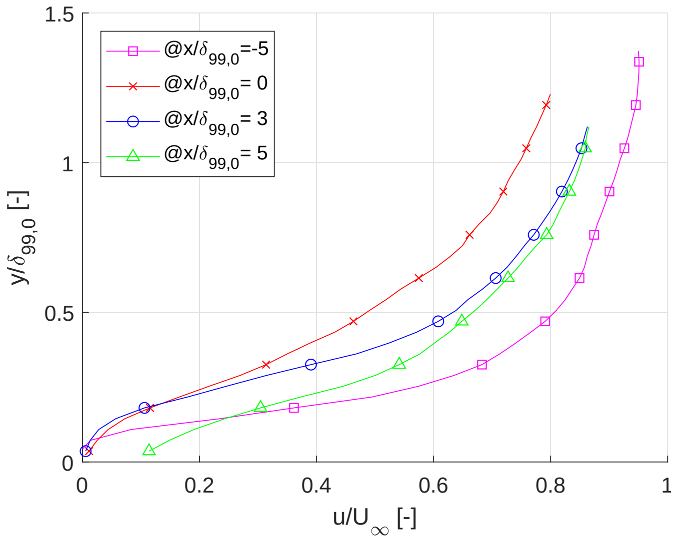

(c) Boundary layer velocity profiles

Figure 5.7: 5.0° wedge and 1.0mm holes, 5.0% porosity plate

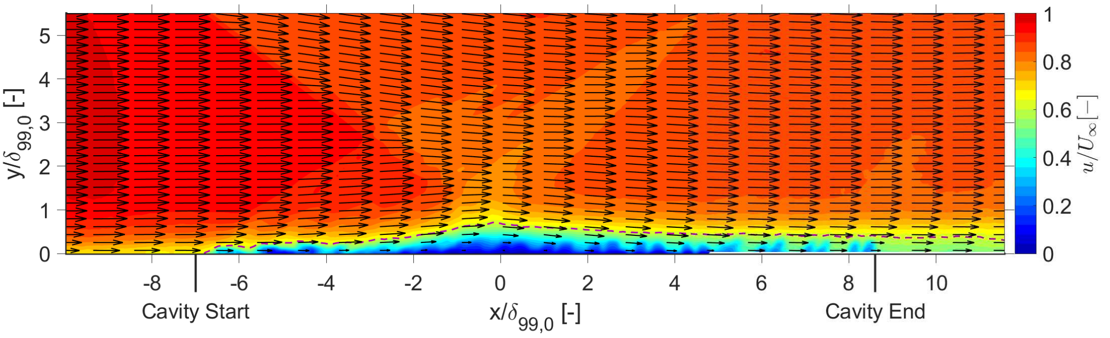

(a) Mean horizontal velocity field. Sonic line shown as dashed purple line

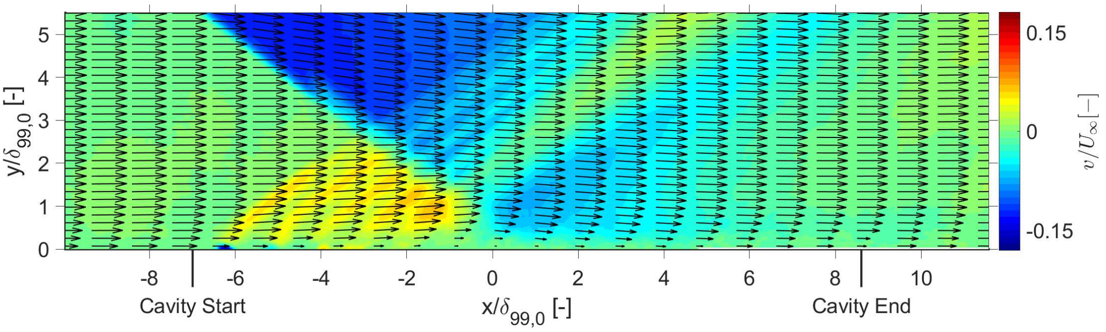

(b) Mean vertical velocity field

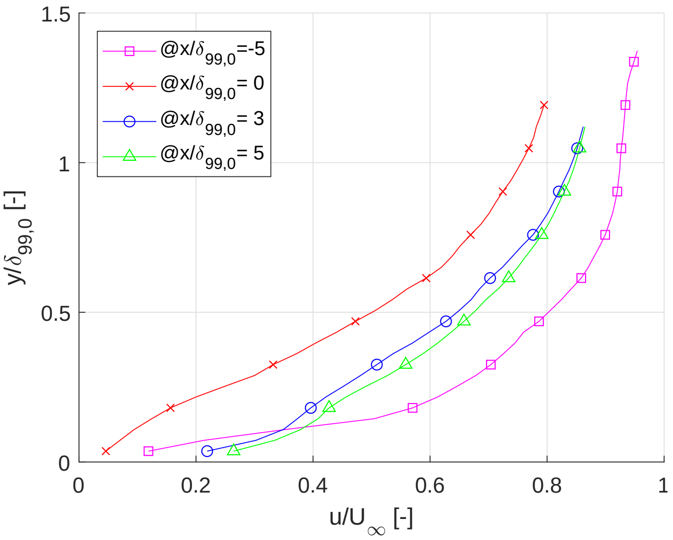

(c) Boundary layer velocity profiles

Figure 5.8: 5.0° wedge and 1.5mm holes, 5.0% porosity plate

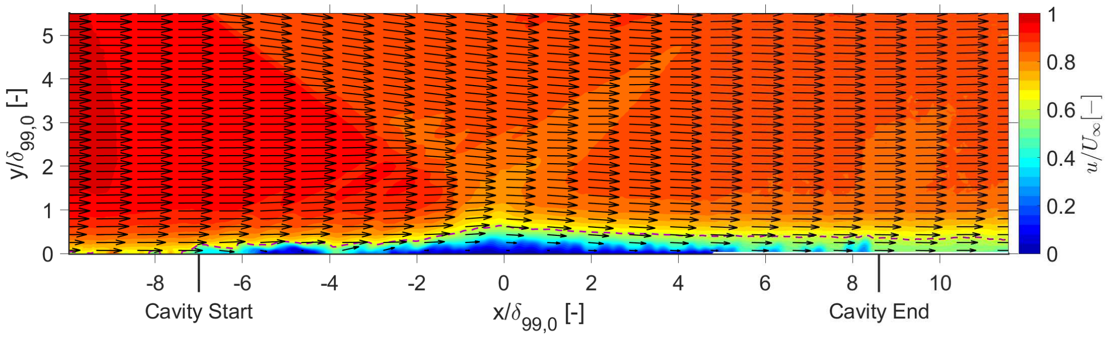

(a) Mean horizontal velocity field. Sonic line shown as dashed purple line

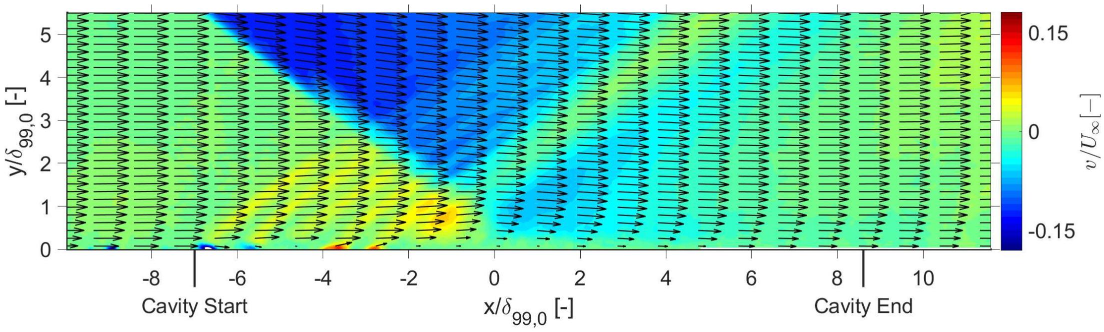

(b) Mean vertical velocity field

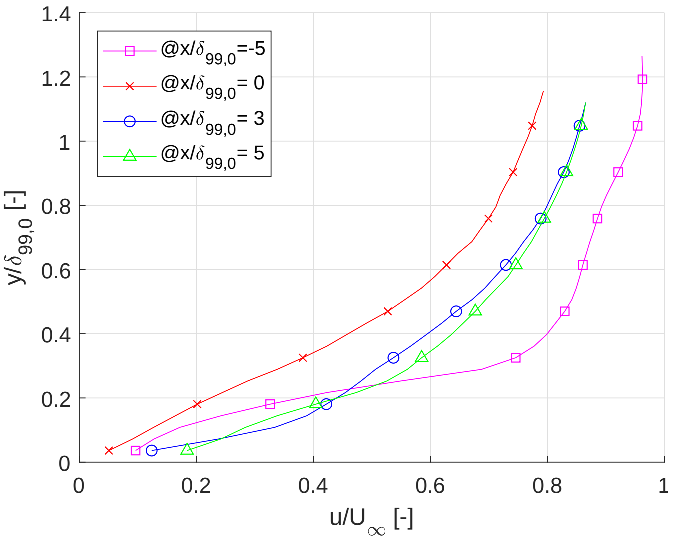

(c) Boundary layer velocity profiles

Figure 5.9: 5.0° wedge and 1.0mm holes, 2.5% porosity plate

Comparing the mean horizontal velocity plots, Figure 5.5a, to 5.6a, 5.7a, 5.8a and 5.9a, it is clear that the dummy plate case has a much smaller region of subsonic flow. Of the porous plates, the 1.0mm holes, 2.5% porosity plate seems to have the smallest region of subsonic flow. Apart from these two observations, there isn't much difference between the plots.

Concerning the vertical velocity plots, in Figures 5.5b, the dummy plate case, a small upward velocity region can be seen, followed by a small downward velocity region, which is likely due to the growth and decline of the boundary layer height, associated to the compression and subsequent expansion of the flow over the interaction, with corresponding upwards and downwards velocity components. In the other vertical velocity plots, 5.6b, 5.7b, 5.8b and 5.9b, larger such regions with larger velocity magnitudes can be observed, likely due to a combination of the outflow from the cavity upstream and inflow downstream, as well as the growth and decline of the boundary layer. The region with an upwards velocity component seems much more continuous in the case of the 0.5mm holes plate in Figure 5.6b, while in Figures 5.7b, 5.8b and 5.9b, pairs of compression and expansion waves can be seen, seemingly arising from the flow from individual holes. The 2.5% porosity plate in Figure 5.9b seems to have the lowest magnitudes of vertical velocity.

From the boundary layer profiles in Figures 5.5c, 5.6c, 5.7c, 5.8c, 5.9c, it is clear that although the dummy plate's velocity profile has quite a high shape factor H which makes it prone to separation (compared to the undisturbed case), this is much more the case for the velocity profiles with porous plates. Concerning variation at the locations of these velocity profiles, the magenta line in the figures show that after having encountered the cavity, the porous plate causes a vast deceleration of the flow at low height near the wall, with relatively less at a larger height. The velocity profile appears lowest across its entire height at the shock impingement location, as well as most prone to separation (due to its low velocity near the wall), and as one goes further downstream, it seems to slowly get back to its original speed. The regeneration of the boundary layer (it becoming more full) seems to occur the most for the plate with 1.5mm holes.

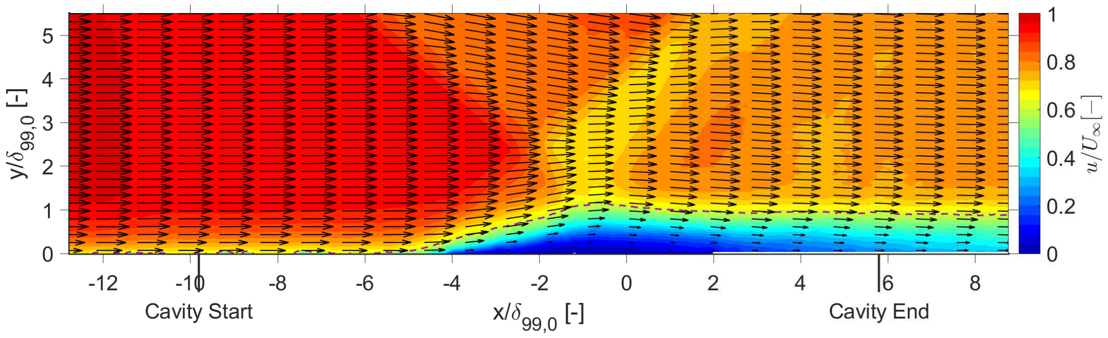

(a) Mean horizontal velocity field. Sonic line shown as dashed purple line

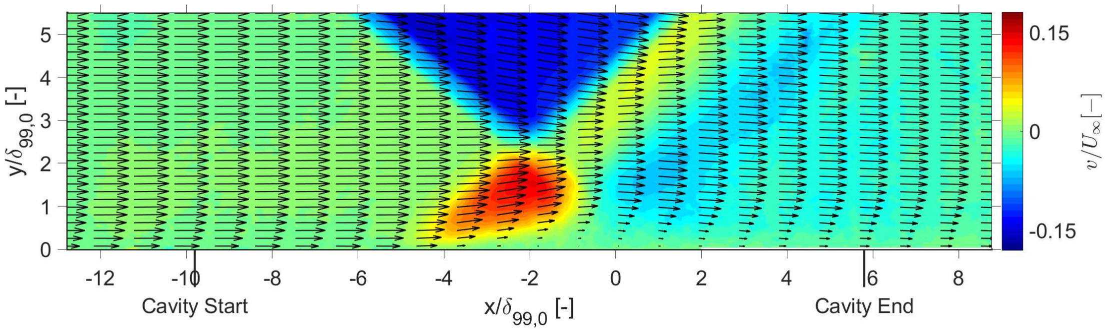

(b) Mean vertical velocity field

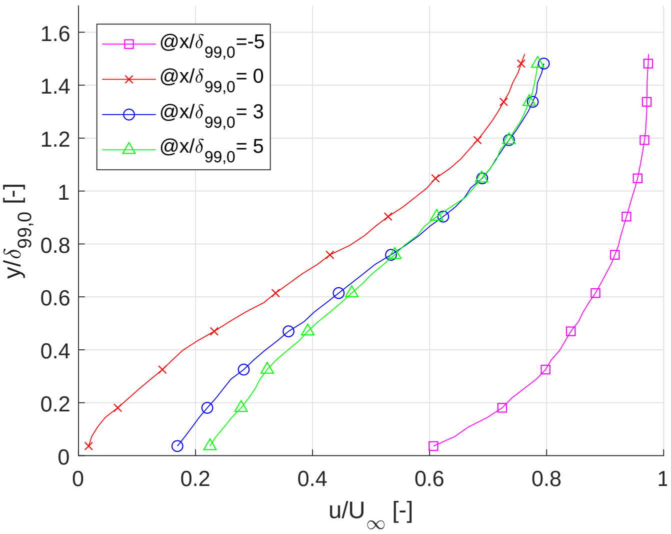

(c) Boundary layer velocity profiles

Figure 5.10: 8.8° wedge and dummy plate

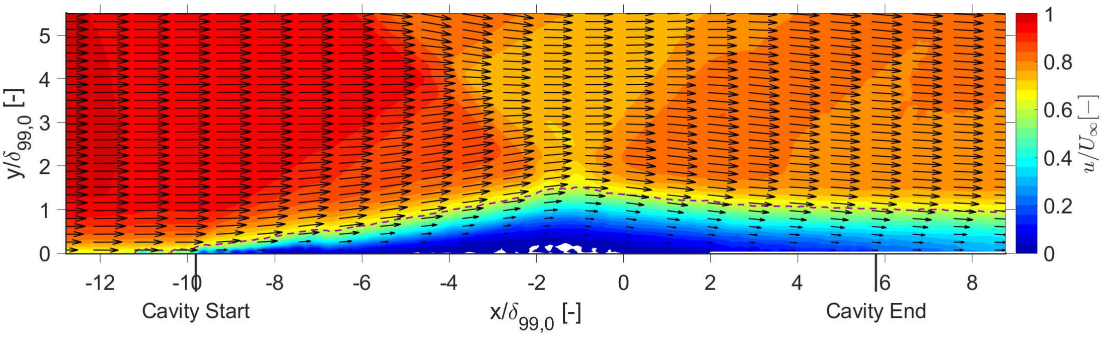

(a) Mean horizontal velocity field. Sonic line shown as dashed purple line

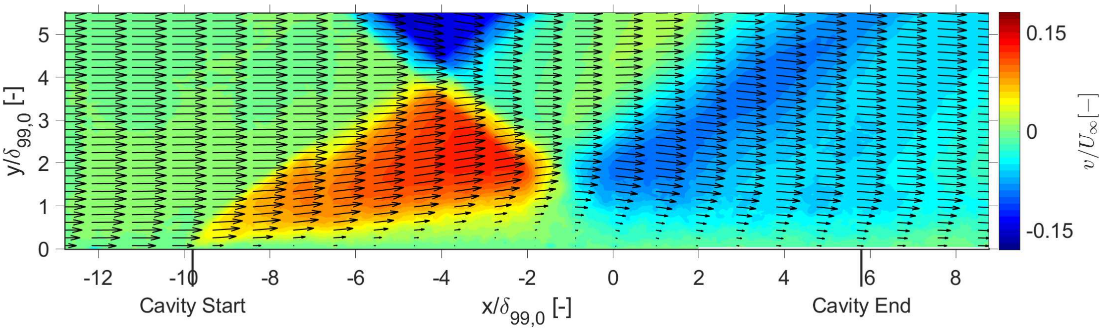

(b) Mean vertical velocity field

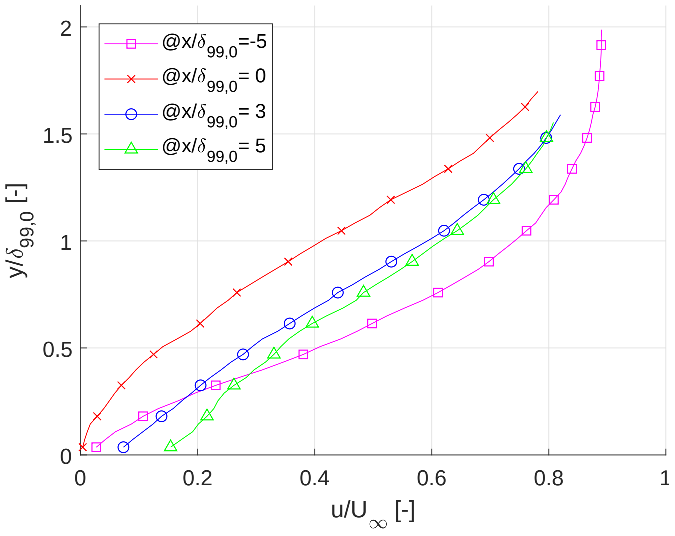

(c) Boundary layer velocity profiles

Figure 5.11: 8.8° wedge and 0.5mm holes, 5.0% porosity plate

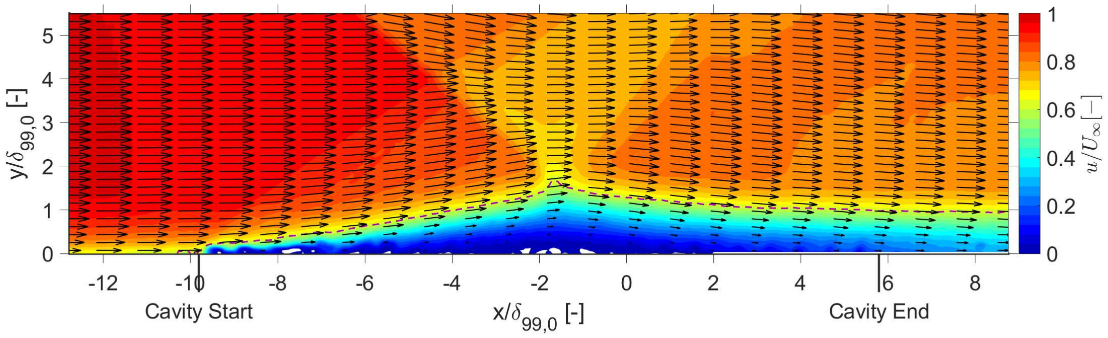

(a) Mean horizontal velocity. Sonic line shown as dashed purple line

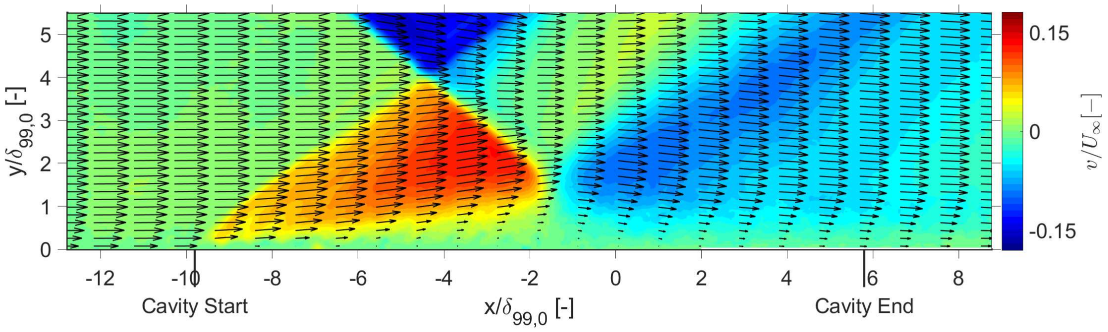

(b) Mean vertical velocity field

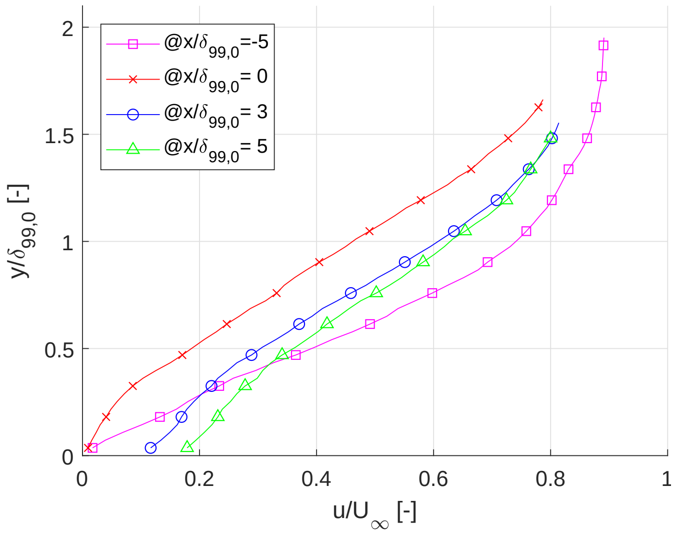

(c) Boundary layer velocity profiles

Figure 5.12: 8.8° wedge and 1.0mm holes, 5.0% porosity plate

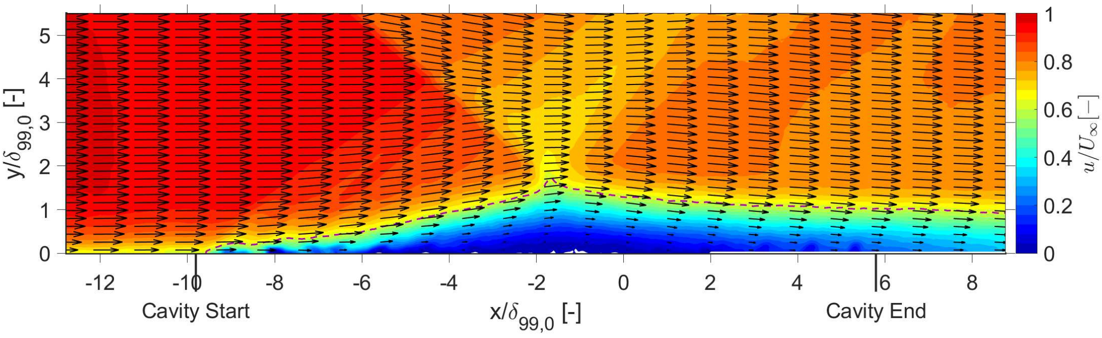

(a) Mean horizontal velocity field. Sonic line shown as dashed purple line

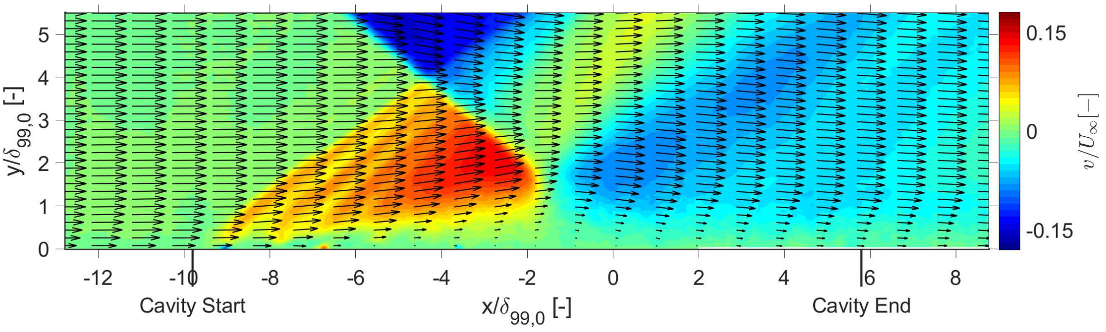

(b) Mean vertical velocity field

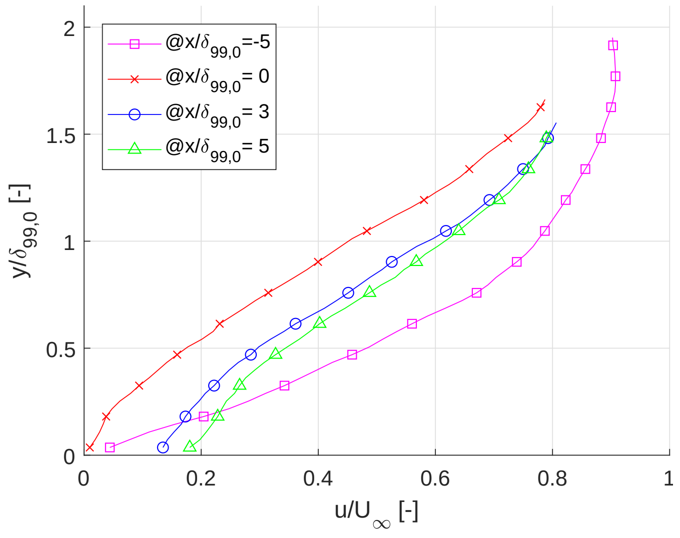

(c) Boundary layer velocity profiles

Figure 5.13: 8.8° wedge and 1.5mm holes, 5.0% porosity plate

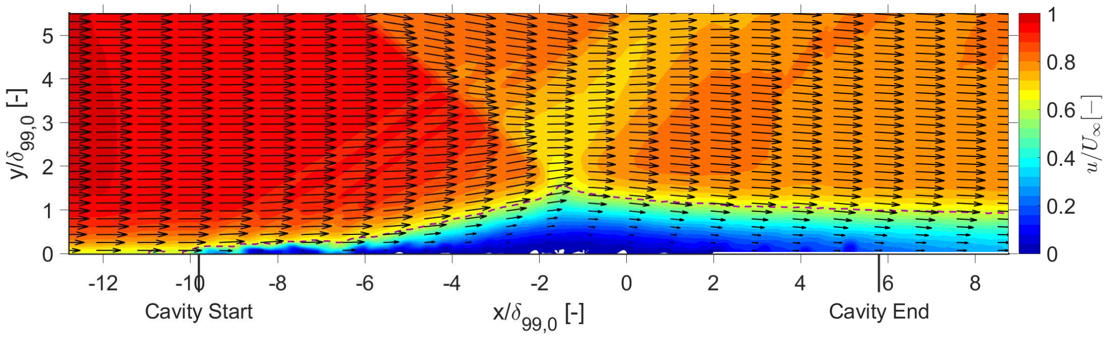

(a) Mean horizontal velocity field for 8.8° wedge and 1.0mm holes, 2.5% porosity plate. Sonic line shown as dashed purple line

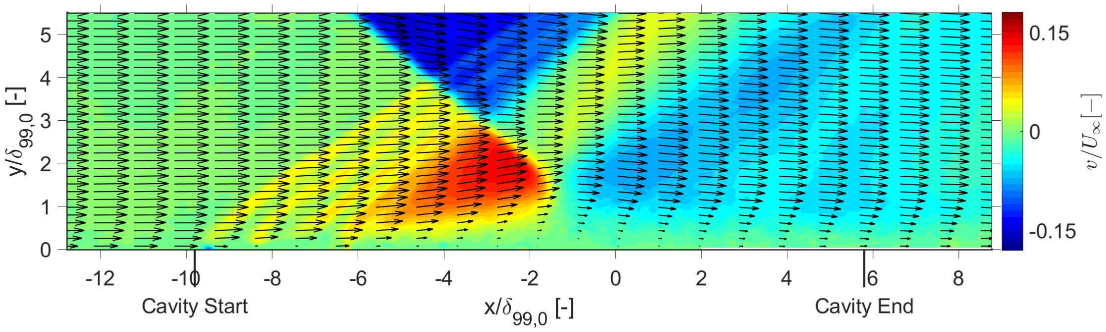

(b) Mean vertical velocity field for 8.8° wedge and 1.0mm holes, 2.5% porosity plate

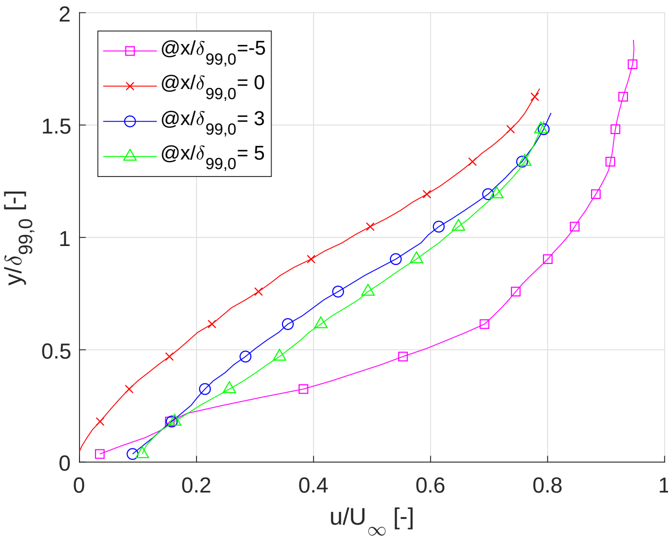

(c) Boundary layer velocity profiles for 8.8° wedge and 1.0mm holes, 2.5% porosity plate

Figure 5.14: 8.8° wedge and 1.0mm holes, 2.5% porosity plate

The horizontal velocity plots for the 8.8° wedge are shown in Figures 5.10a to 5.14a. These show a larger subsonic region, implying more boundary layer deceleration, than all of the 5.0° cases. In turn each of the porous plate cases, shown in Figures 5.11a to 5.14a, show more deceleration than the dummy plate case in Figure 5.10a, even so much that regions where the mean velocity is negative (i.e. separation areas) are present, visible as white spots.

Concerning the mean vertical velocity fields in Figures 5.10b, 5.11b, 5.12b, 5.13b, and 5.14b, it is clear that again, like in the 5.0° cases, regions with upwards velocity are present above the start of the plate, followed by regions with downwards velocity downstream. For the dummy plate case, this is likely only due to the growth and decline of the boundary layer, and for the porous plate cases, also due to the in- and outflow from the holes. For the porous plate cases, the velocities have a higher magnitude than for the dummy plate, and for all the 8.8° wedge cases, the magnitude is higher than for the 5.0° wedge cases. The region with a positive velocity component looks very continuous for the 0.5mm holes, 5.0% porosity plate. For the other plates, pairs of compression and expansion waves can be seen to emanate from the holes. For the 2.5% porosity plate, the region with upwards vertical velocity seems smaller than for the other 5% porosity plates. Perhaps this indicates that the amount of outflow through the holes is limited by the porosity. Another difference with the 5.0° wedge cases that is visible in the vertical velocity plots is the fact that there is a much larger region behind the interaction with negative vertical velocity. It seems to be the case that the interactions arising from the 8.8° wedge cause for more momentum to be transferred upwards, taking a longer distance to move back down. This could also be seen in the higher H of the downstream boundary layer and its slower regeneration.

Comparing the velocity profiles of the 8.8° wedge, it is visible that for the dummy plate case in Figure 5.10c, the boundary layer has a more empty profile and has experienced more deceleration than all of the 5.0° wedge cases. Again, like for the 5.0° wedge cases, the porous plates' presence causes more deceleration (especially at low y), and the boundary layer regenerates slowly downstream of the shock impingement point. Concerning variation of the velocity profiles for different porous plates in the 8.8° wedge case, the downstream boundary layers of the 1.0mm and 1.5mm holes, 5% porosity plates appear to regenerate more quickly, although not much variation can be seen.

5.5 Percentage of backflow

In Figures 5.15a to 5.16e, contour plots show how the percentage of vectors that had a negative horizontal component is distributed, thus effectively for what percentage of the time there was backflow. The only region that is plotted is the middle of the porous cavity, to a limited height above it, as the percentage of backflow outside of this region was negligible in all cases.

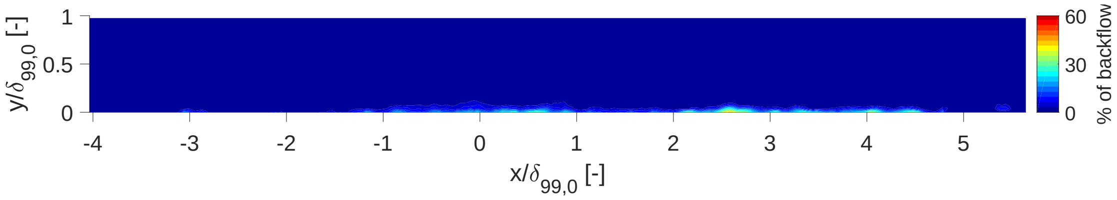

(a) Dummy plate

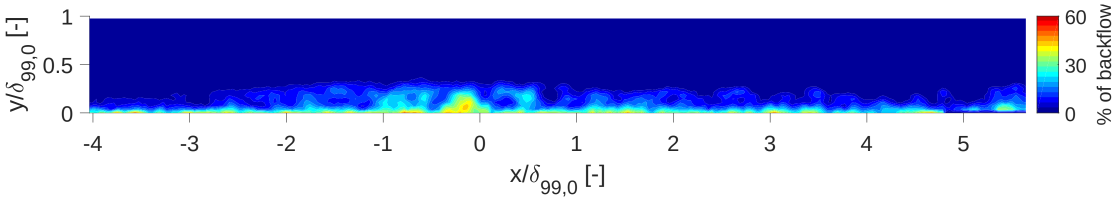

(b) 0.5mm holes, 5.0% porosity plate

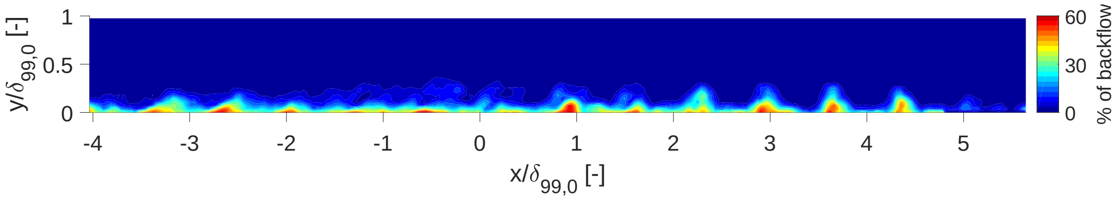

(c) 1.0mm holes, 5.0% porosity plate

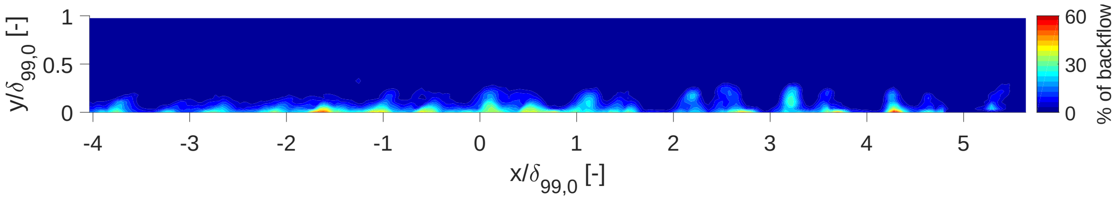

(d) 1.5mm holes, 5.0% porosity plate

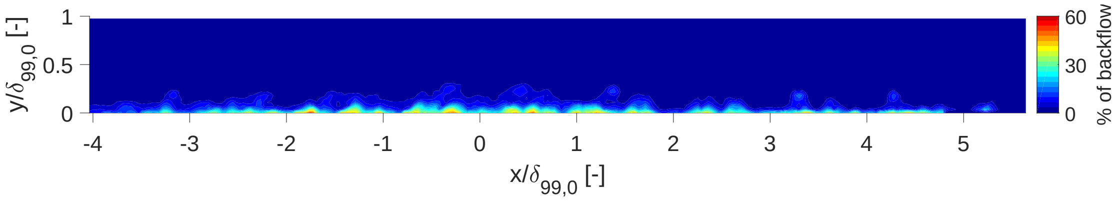

(e) 1.0mm holes, 2.5% porosity plate

Figure 5.15: Percentage of backflow for 5.0° wedge cases

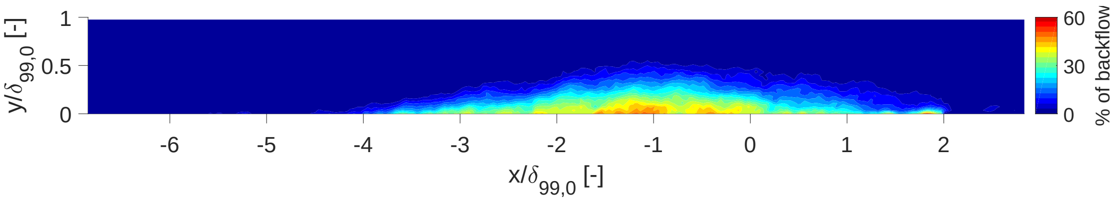

(a) Dummy plate

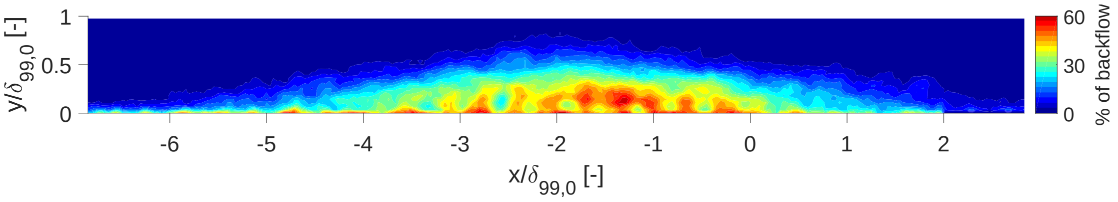

(b) 0.5mm holes, 5.0% porosity plate

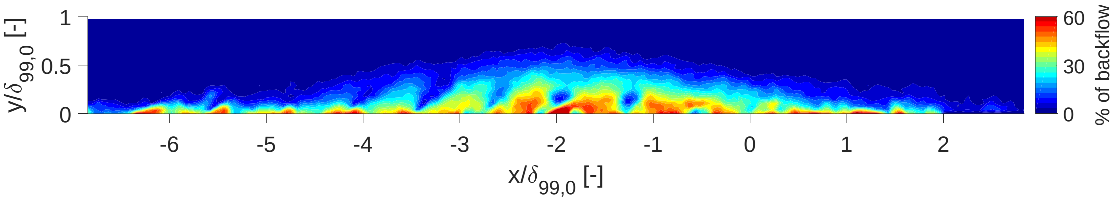

(c) 1.0mm holes, 5.0% porosity plate

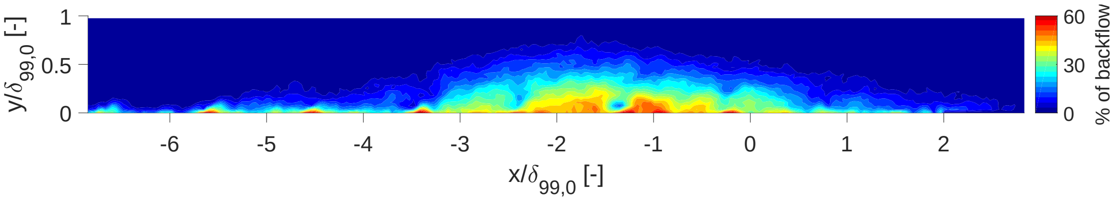

(d) 1.5mm holes, 5.0% porosity plate

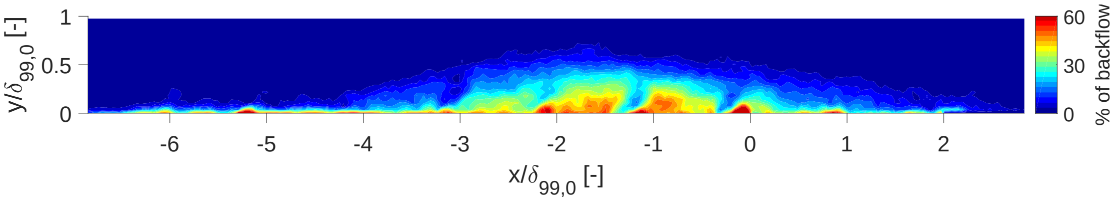

(e) 1.0mm holes, 2.5% porosity plate

Figure 5.16: Percentage of backflow for 5.0° wedge cases

From the figures it is clear that the 5.0° wedge, dummy plate case, shows negligible amounts of backflow. The 5.0° wedge cases with porous plates show more, although significant difference between them is difficult to conclude. For the 8.8° wedge there is generally more backflow for all cases, and specifically more for the porous plate cases. The most significant backflow seems to occur in the 8.8° wedge, 0.5mm hole size, 5.0% porosity case. Although in general, spots with high amounts of backflow can be seen at locations just above holes in the upstream part of the plots, the most significant backflow is generally found in the middle of the plot region, just before and up to the shock impingement point at $x/\delta_{99,0} = 0$.

5.6 Separation area

Wedge angle [°]:	Plate :	Separation area [$\delta_{99,0}^2$]:
5.0	Dummy	0.0470
5.0	0.5mm holes, 5% porosity	0.548
5.0	1.0mm holes, 5% porosity	0.585
5.0	1.5mm holes, 5% porosity	0.270
5.0	1.0mm holes, 2.5% porosity	0.294
8.8	Dummy	0.442
8.8	0.5mm holes, 5% porosity	1.088
8.8	1.0mm holes, 5% porosity	0.892
8.8	1.5mm holes, 5% porosity	0.709
8.8	1.0mm holes, 2.5% porosity	0.757

Table 5.2: Separation areas for each case

In Table 5.2 the separation areas are shown, found by integrating the percentages of backflow over their area (i.e. integrating the plots of Figures 5.15a to 5.16e). The area over which was integrated was from $y/\delta_{99,0} = 0$ to 2.0, and from $x/\delta_{99,0} = -13.5$ to 12.8 for the 5.0° wedge and from -16.3 to 10.0 for the 8.8°. For every plate, the influence of the wedge angle can be seen to have increased the separation area (in some cases much more than others). Comparing between the different plates per wedge, the dummy plate can be seen to have the lowest separation area. The plates with 0.5mm and 1.0mm holes and 5% porosity seem to have the largest separation area, followed by the 1.5mm holes, 5% porosity and 1.0mm holes, 2.5% porosity plates.

5.7 Boundary layer integral parameters over the cavity

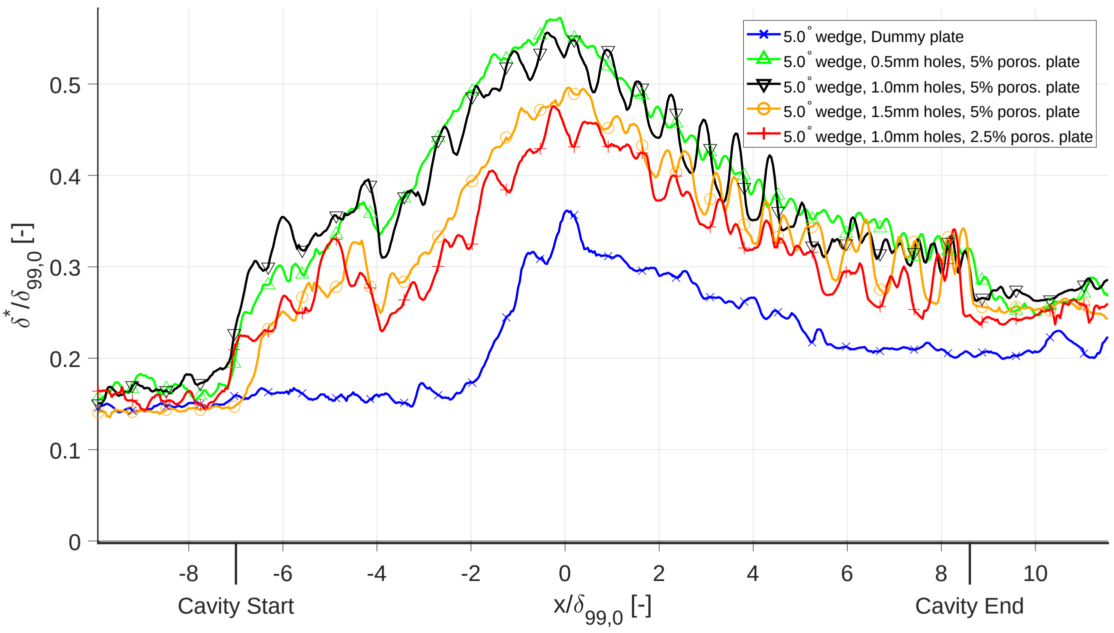

Figure 5.17: Displacement thickness over the cavity, for the cases of the 5.0° wedge

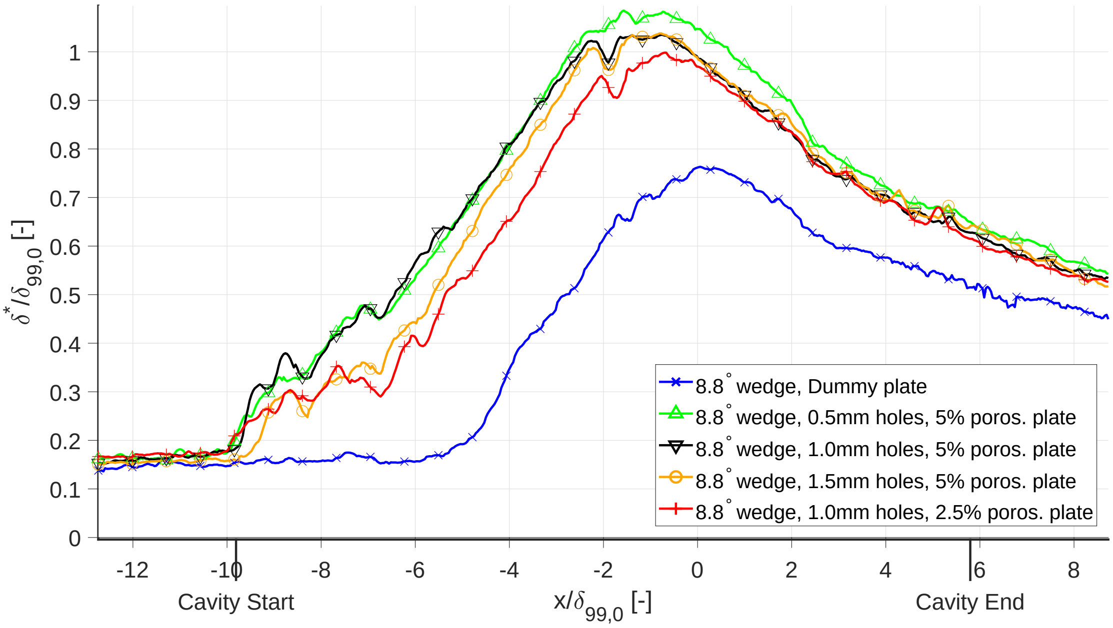

Figure 5.18: Displacement thickness over the cavity, for the cases of the 8.8° wedge

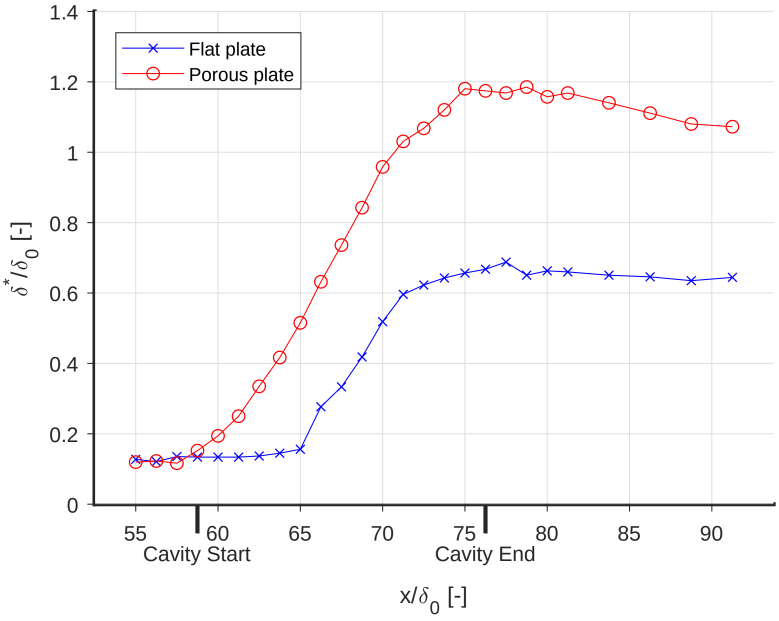

Figure 5.19: Displacement thickness over the cavity, in the study of Bur et al. (1998)

In Figure 5.17 and 5.18, the displacement thickness over the cavity is shown. The heights which have been used up to which to integrate to obtain these values are shown in Appendix C. In every case, the evolution of δ^* portrays the same shape, starting at a low value upstream, to a peak value at around $x/\delta_{99,0} = 0$, to a lesser (but still larger than the upstream) value downstream. The 8.8° wedge cases have, in their entirety, higher displacement thicknesses than the 5.0° wedge cases. Concerning variation within the set of porous plates, it can be observed that generally, the 0.5mm hole plate has the highest displacement thickness, followed by the one with 1.0mm holes and 5% porosity, followed by the 1.5mm hole plate, and followed finally by the one with 1.0mm holes and 2.5% porosity. These all have higher displacement thicknesses than the dummy plate. Especially in the 5.0° wedge case, sharp peaks and troughs can be observed, which are caused by the flow from holes in the plate.

In Figure 5.19 the displacement thickness of the investigation by Bur et al. (1998) is shown whereby a lambda shock took place over a porous plate covering a cavity. The values (as well as those of Figures 5.22, 5.25 and 5.22) are difficult to compare, one of the reasons likely being that Bur et al. (1998) did not have to decide on a distinct height up to which to integrate, because an oblique shock did not impinge directly on the boundary layer in the cavity in their case, so the integral in Equation 3.1 likely converged. Another reason is the fact that the flow situation is basically quite different: their case had the two feet of a lambda shock found at the two ends of the plate, which caused for an approximately constant horizontal pressure gradient over the plate. In the case of the present investigation, a more localized pressure jump is found at the position of the shock impingement location.

Despite these differences, similarities can still be seen in the fact that the distributions in this figure experience a peak within the region above the cavity, and that they decrease to a lesser value afterwards. Like in the case of the present investigation, the porous plate has a higher displacement thickness. Comparing the ratio of the downstream displacement thickness with the porous plate to that of the dummy plate, it is visible that this is approximately 1.67 in the case of Bur et al. (1998), and approximately 1.2 in the case of the present investigation, a significant difference.

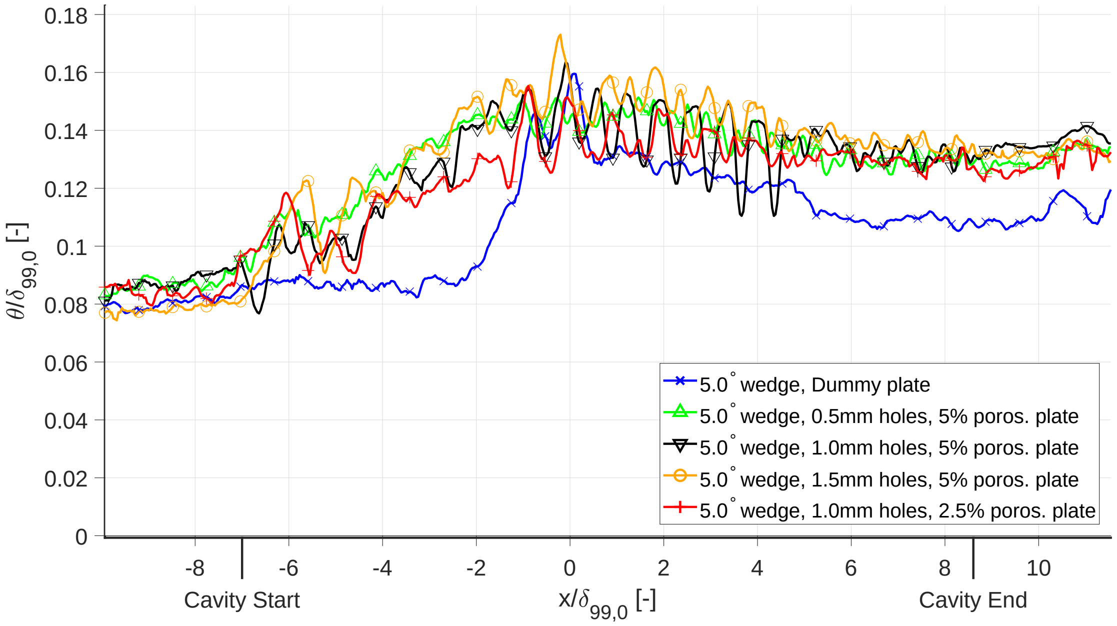

Figure 5.20: Momentum thickness over the cavity, for the cases of the 5.0° wedge

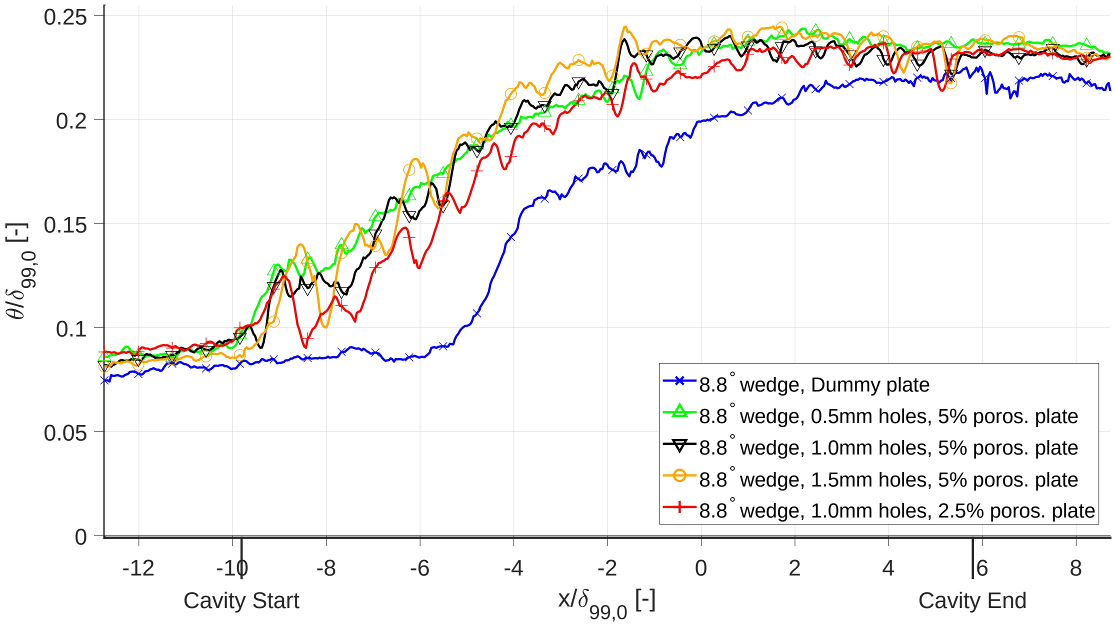

Figure 5.21: Momentum thickness over the cavity, for the cases of the 8.8° wedge

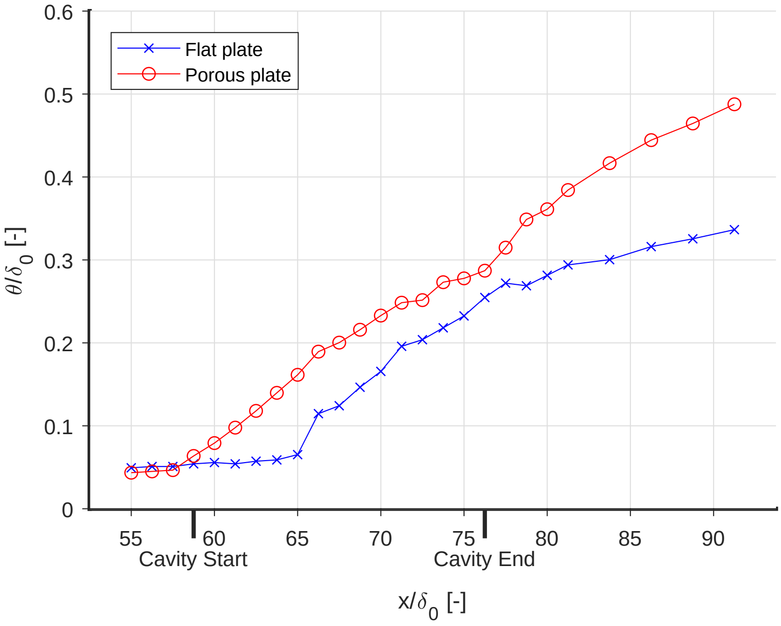

Figure 5.22: Momentum thickness over the cavity, in the study of Bur et al. (1998)

In Figures 5.20, 5.21 and 5.22 the momentum thicknesses over the cavity are shown, whereby the heights of Appendix C have also been used to calculate them. The distributions that can be observed are different from those of the displacement thickness shown in Figures 5.17, 5.18 and 5.19, as less of a peak in the middle and decrease in the downstream section occurs. The increased wedge angle again seems to have a larger effect on increasing momentum thickness than the variation caused by different plates. Concerning variation due to the plates themselves, the 1.5mm holes plate seems to have the highest distribution, followed by the 0.5mm holes plate and 1.0mm holes, 5% porosity plate (which are approximately equal in magnitude), finally followed by the 1.0mm holes, 2.5% porosity plate. All porous plates have significantly larger momentum thicknesses than the dummy plate. As was the case for displacement thickness, sharp peaks and troughs are visible from the flow through the holes in the plate.

Comparing the shape with the curves of Figure 5.22, the shape of the curves is again similar in the way that little (in this case no) decrease beyond the end of the cavity can be observed, and the porous plate also has a higher momentum thickness. The factor of downstream momentum thickness with a porous plate to the dummy pate is approximately 1.45 in the case of Bur et al., and approximately 1.1 in the case of the present investigation.

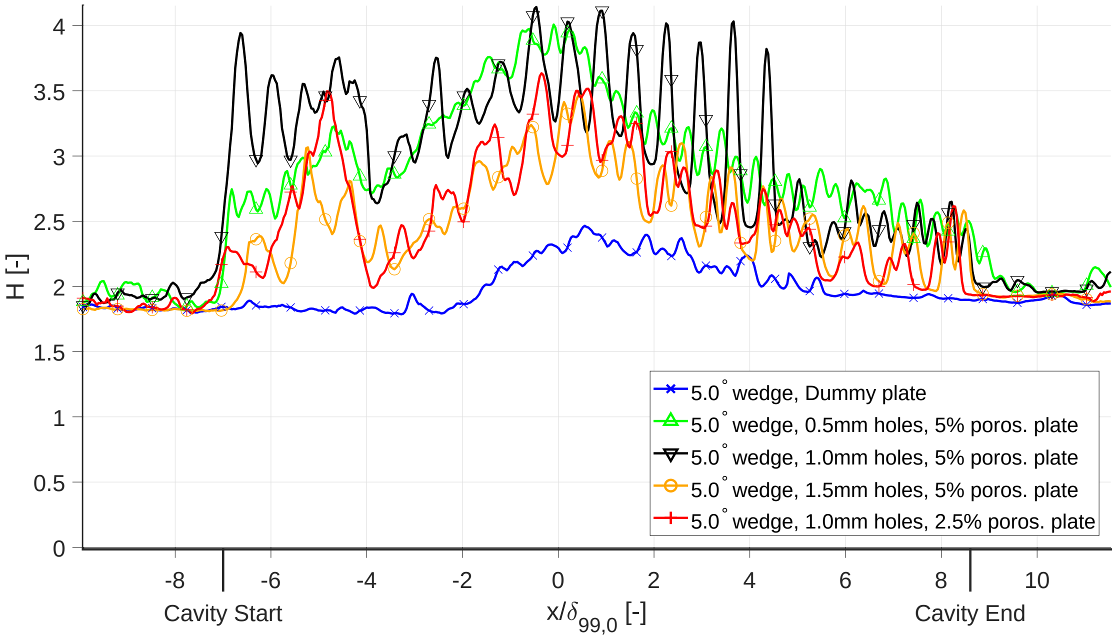

Figure 5.23: Shape factor over the cavity, for the cases of the 5.0° wedge

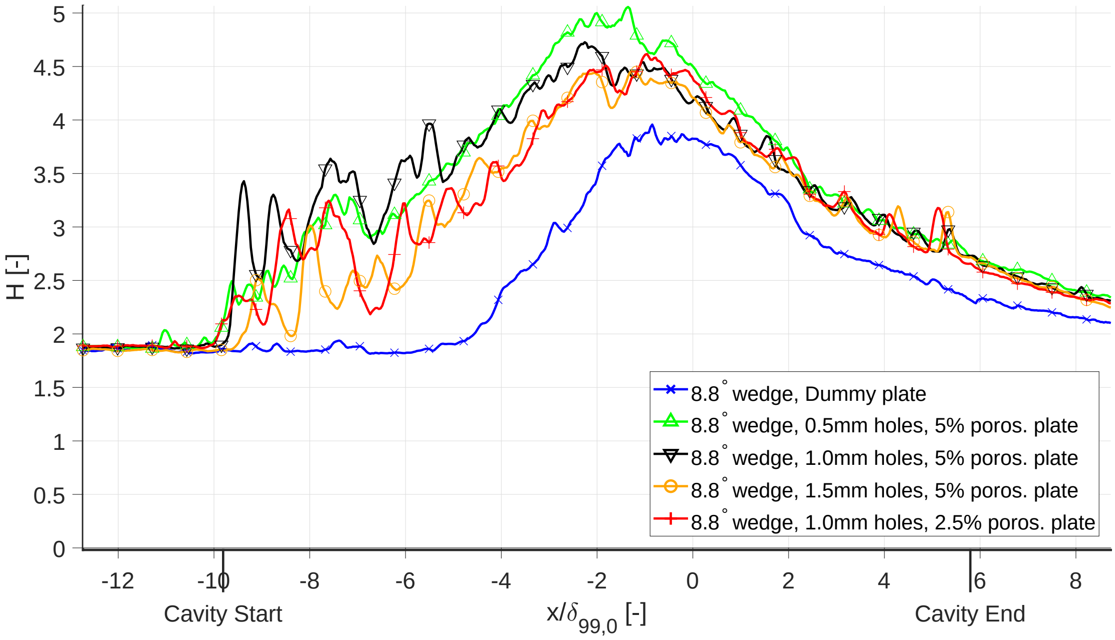

Figure 5.24: Shape factor over the cavity, for the cases of the 8.8° wedge

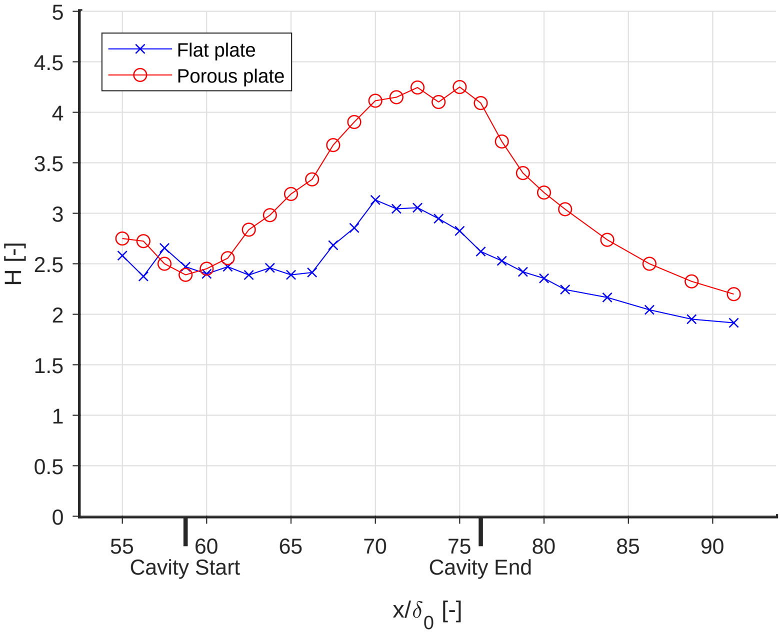

Figure 5.25: Shape factor over the cavity, in the study of Bur et al. (1998)

In Figures 5.23, 5.24 and 5.25, the distribution of the shape factor over the cavity is shown, obtained by dividing the curves of Figures 5.17, 5.18 and 5.19 by those of 5.20, 5.21 and 5.22. It could already be seen in the velocity profiles previously plotted that the boundary layers of the 8.8° wedge cases were at a high risk of separating, which is proven again here due to their high shape factors, which are all higher than their respective cases for the 5.0° wedge. The order from high to low concerning the different plates seems to be: the 0.5mm holes, 5% porosity plate, the 1.0mm holes, 5% porosity plate, the 1.0mm holes, 2.5% porosity plate, the 1.5mm holes, 5% porosity plate, and the dummy plate.

The results from Bur et al. (1998) in Figure 5.25 show that the value of H starts off much larger at the upstream end of what has been plotted than with the present investigation. With Bur et al. one foot of the lambda shock was found at the Cavity Start, and the influence of this (the growth of the boundary layer and increase in its shape factor H) undoubtedly has an effect upstream already. Downstream, the boundary layer even seems to become more full (decrease to a lower H) than what has been plotted of it upstream. Because it is expected the distribution of Bur et al. started out with a lower H-value upstream, the curves as they have been plotted cannot be compared well.

5.8 Vertical velocity over the cavity

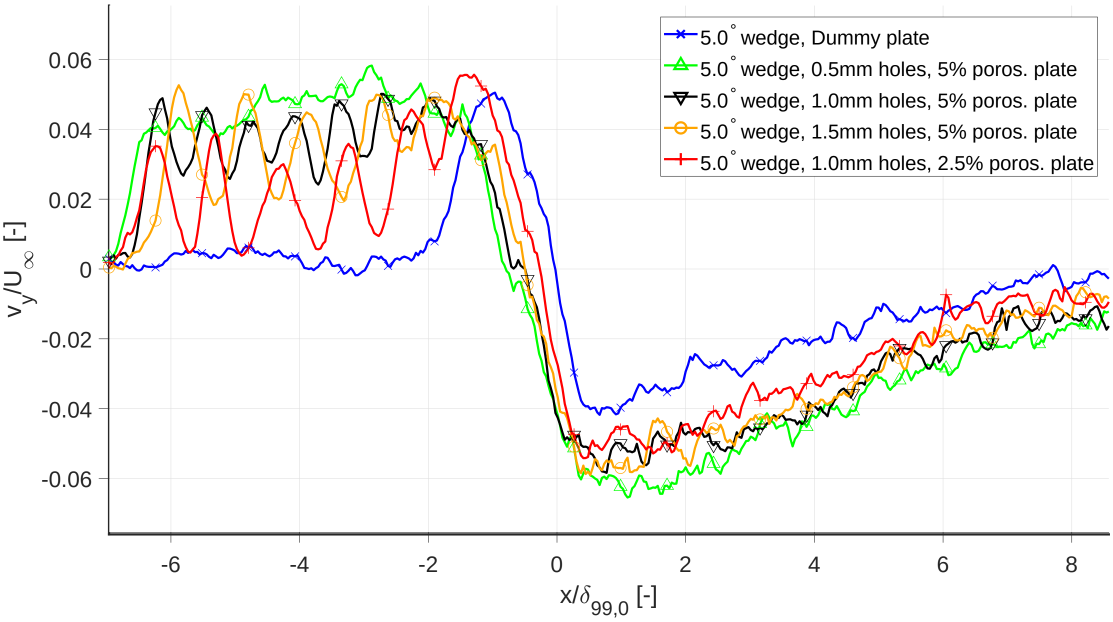

Figure 5.26: Vertical velocity component over the cavity at a height of $y/\delta_{99,0} = 0.506$, for the cases of the 5.0° wedge

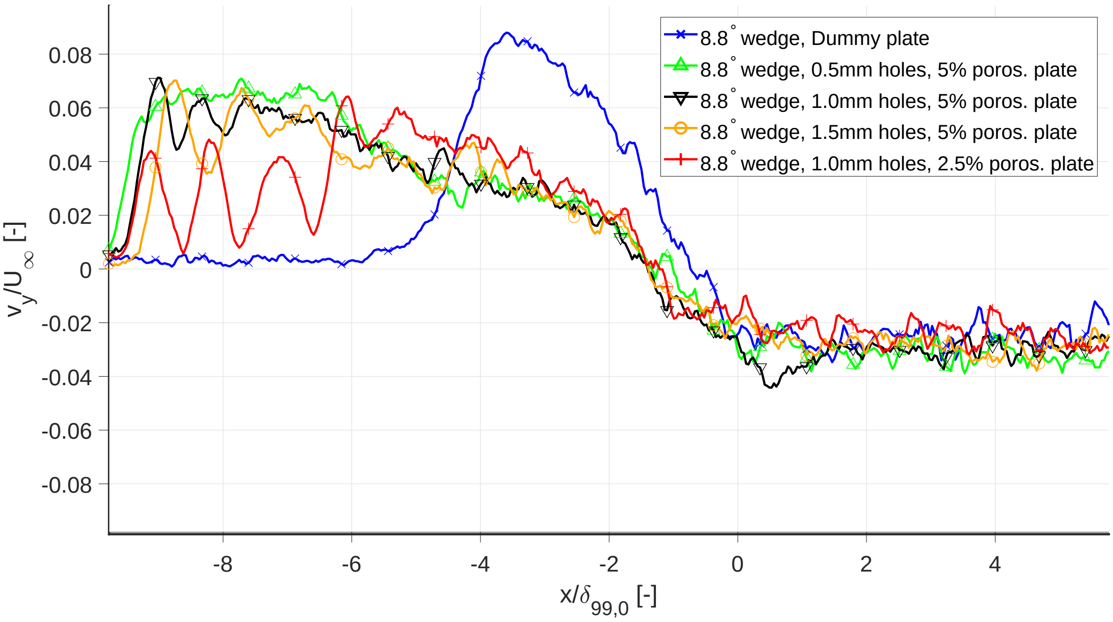

Figure 5.27: Vertical velocity component over the cavity at a height of $y/\delta_{99,0} = 0.506$, for the cases of the 8.8° wedge

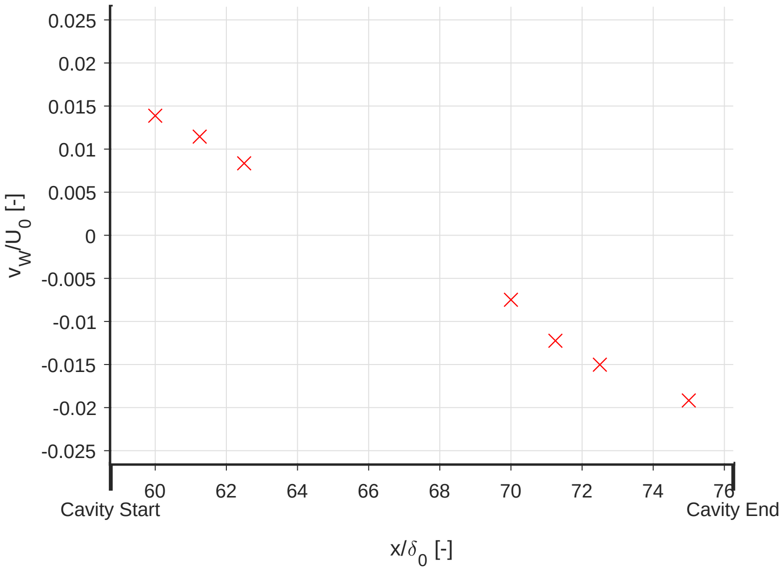

Figure 5.28: Vertical velocity component over the cavity, in the study of Bur et al. (1998)

In Figures 5.26 and 5.27 the vertical velocity has been plotted as found over the cavity at a height of $y/\delta_{99,0} = 0.506$. Positive values can be seen to occur in the upstream part above the cavity and negative values in the downstream part. The blue curve represents the dummy plate, and the fact that the other curves have more positive values upstream and more negative values downstream suggests that significant airflow out of the cavity through the holes upstream and flow into the cavity downstream took place. The distributions shown in the curves give suggest that air flowed through the plates themselves. An attempt to calculate the mass flux through the plates, as well as the results of this attempt, are shown in Appendix D.

In Figure 5.28 the vertical velocity from Bur et al., measured at the holes themselves, is plotted. The plots are difficult to compare as these values have been plotted based on measurements at a height of $y = 0$, and Figures 5.26 and 5.27 also include the vertical component of the growth and decline of the boundary layer. The only significant observation that can be made is that flow seemingly arising from the cavity in Bur et al.'s investigation is of the same order ($v/U_\infty = 0.01$) as the present investigation.

Chapter 6

Flow field fluctuations

6.1 Introduction

In this chapter, the second part of the set of results are discussed, namely those pertaining to flow field fluctuations, and thus the unsteady aspects of the flow field. The turbulent kinetic energy $1/2(u'^2 + v'^2)/U_\infty^2$ for the entire flow field are shown for each case in Figures 6.1 to 6.10.

6.2 Turbulent kinetic energy plots

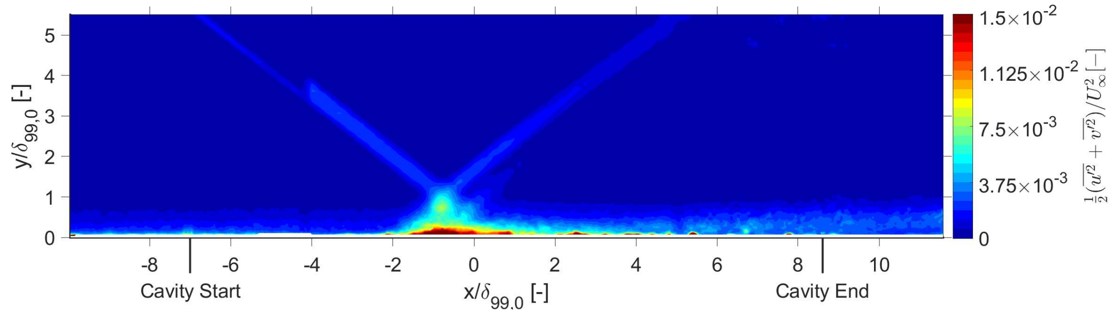

Figure 6.1: Turbulent kinetic energy flow field for 5.0° wedge and dummy plate

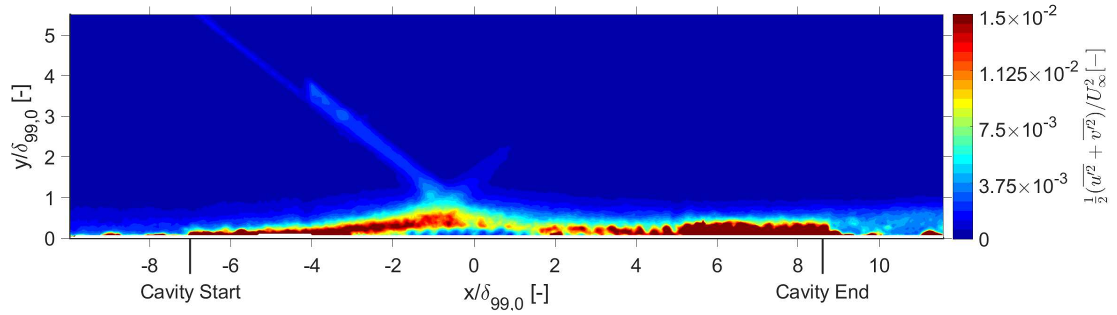

Figure 6.2: Turbulent kinetic energy flow field for 5.0° wedge and 0.5mm holes, 5% porosity plate

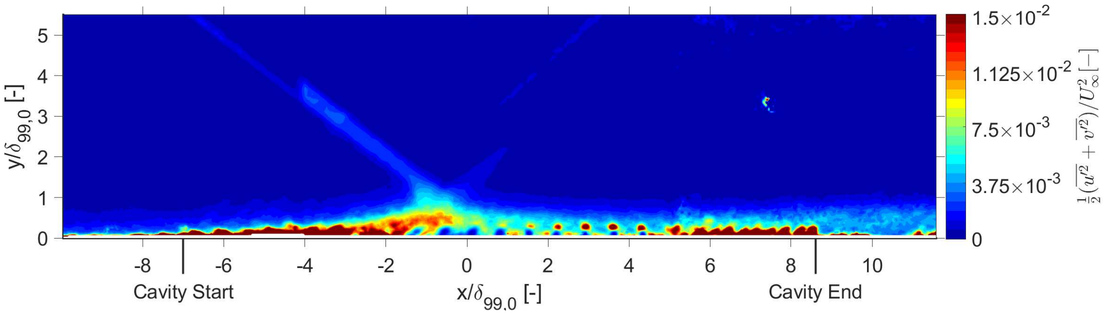

Figure 6.3: Turbulent kinetic energy flow field for 5.0° wedge and 1.0mm holes, 5% porosity plate

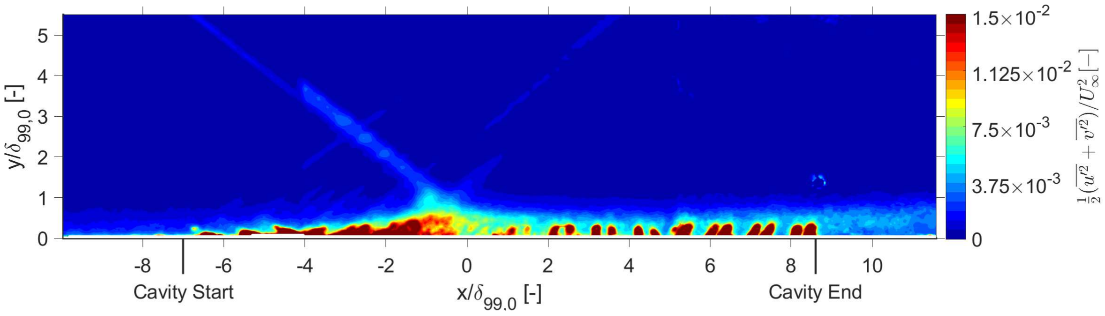

Figure 6.4: Turbulent kinetic energy flow field for 5.0° wedge and 1.5mm holes, 5% porosity plate

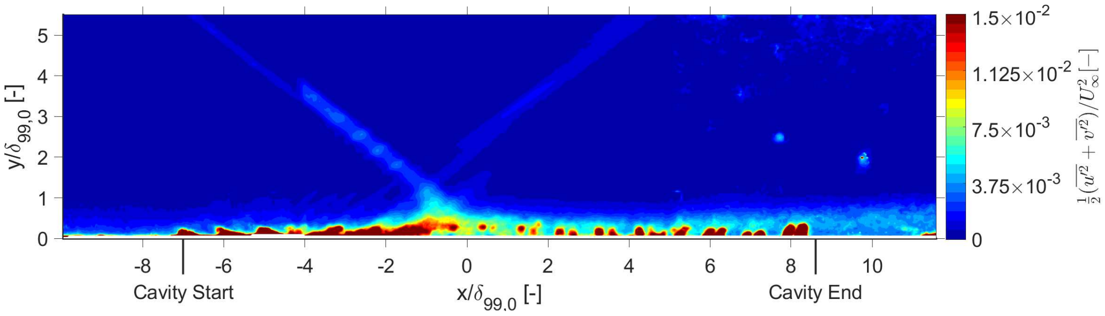

Figure 6.5: Turbulent kinetic energy flow field for 5.0° wedge and 1.0mm holes, 2.5% porosity plate

First of all, it must be stated that the right-most frame seems to show a structural discrepancy in each Figure, whereby the TKE values are higher. This is more visible in some frames (e.g. Figure 6.6) than others (e.g. Figure 6.1). It might be tempting to suspect the camera may have been moved, or something similar might have occurred, during the experiments, but this seems unlikely as the cameras were focused so precisely that even a small change in its location would mean its images would have become blurry, which would have been noticeable. It is assumed that the discrepancy shown by the right-most frame is of a constant nature, so that the TKE values found there can still be compared, although it might be less accurate to compare values of the right-most frame to those found upstream.

Looking at the plots for the 5.0° wedge in Figures 6.1 to 6.5, it is clear that the dummy plate case is hardly turbulent, at the impingement point as well as in the downstream boundary layer. In the porous plate cases, higher turbulent kinetic energy is found over the whole of the interaction, and also in the downstream boundary layer. The level of turbulence in the downstream boundary layer doesn't look significantly different between the porous plate cases to draw any significant conclusions.

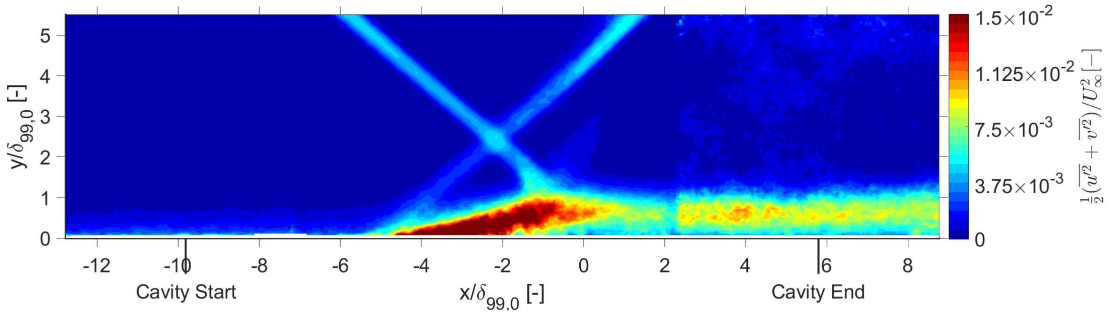

Figure 6.6: Turbulent kinetic energy flow field for 8.8° wedge and dummy plate

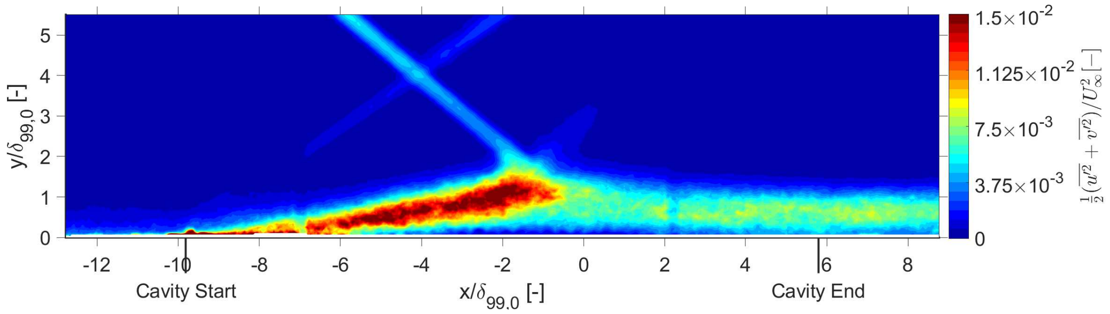

Figure 6.7: Turbulent kinetic energy flow field for 8.8° wedge and 0.5mm holes, 5% porosity plate

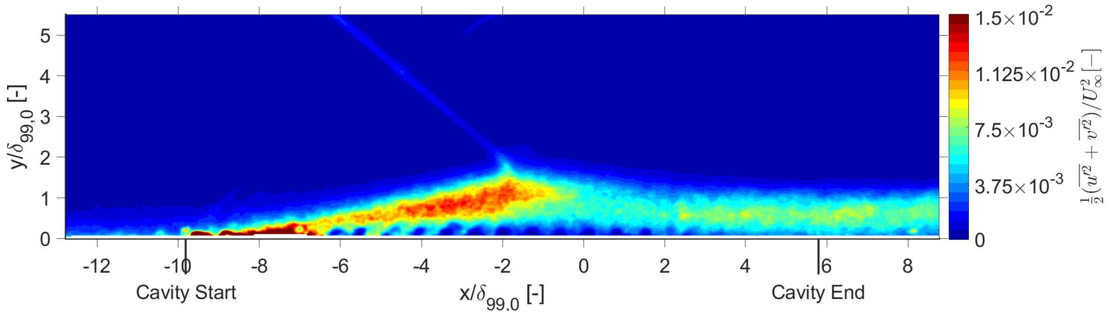

Figure 6.8: Turbulent kinetic energy flow field for 8.8° wedge and 1.0mm holes, 5% porosity plate

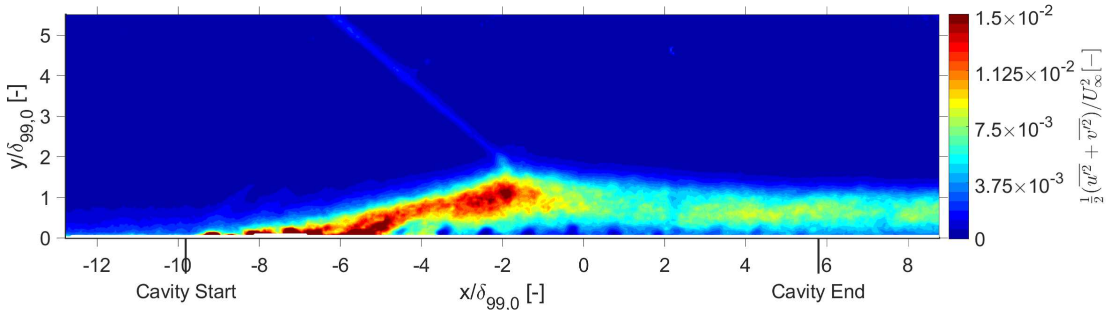

Figure 6.9: Turbulent kinetic energy flow field for 8.8° wedge and 1.5mm holes, 5% porosity plate

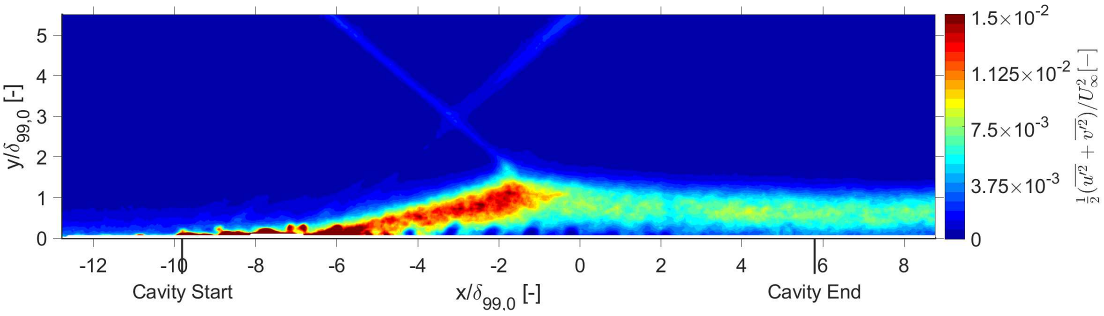

Figure 6.10: Turbulent kinetic energy flow field for 8.8° wedge and 1.0mm holes, 2.5% porosity plate

Judging by the plots for the 8.8° wedge in Figures 6.6 to 6.10, the dummy plate case seems to have a region just before where the incident shock impinges of high turbulence, while this seems to be more spread out for the porous plate cases. Concerning the downstream boundary layer, the level of turbulence of the porous plate cases seems to have decreased compared to that of the dummy plate.

Plots showing other turbulent stress components, namely the turbulent normal stresses u'^2/U_∞^2, v'^2/U_∞^2 and turbulent shear stress $u'v'/U_\infty^2$ are shown in Appendix E. These generally provide for the same conclusions as listed above.

Chapter 7

Conclusion

7.1 Introduction

In this chapter, the conclusions that can be made from the results that have been previously shown and discussed are summarized, and it is attempted to answer the research questions. Also, some recommendations are made for future studies that are to be done on SWBLIs with porous plate-covered cavities.

7.2 Conclusions and answers to the research questions

The research questions that were brought forth in Chapter 1 are answered in this section. The first four are repeated and answered, while simultaneously answering the last three (concerning the effects of hole size, porosity and shock strength), for each.

The first research question was: "How is the effect of the interaction on the downstream boundary layer affected by the presence of the porous plate-covered cavity?" From the figures in section 5.7 it was clear that the porous plate-covered cavity caused a thicker downstream boundary layer due to it causing a higher displacement and momentum thickness. From the Schlieren images of section 5.2 this was already suspected, but the PIV results provide a more accurate indication of this. The changing of hole size and porosity seems to have a small effect on boundary layer thickness, so small that it is too uncertain to draw any conclusion regarding their influence on boundary layer thickness. It seems that higher shock strength, although it is of influence on the downstream boundary layer's thickness due to an interaction in general, does not influence the effect the porous plate-covered cavity has, as the factor by which the downstream boundary layer was thicker did not change significantly with the larger wedge angle.

The second research question was: "How is the level of turbulence downstream of the interaction affected by the presence of the porous plate-covered cavity?". From the plots in Chapter 6, it could be seen that for a low shock strength, the TKE in the downstream boundary layer increased with a porous plate-covered cavity, but that for a high shock strength the TKE in the downstream boundary layer decreased. This prompts the conclusion of an inverse correlation between shock strength and TKE in the downstream boundary layer. The results did not vary significantly between different plates, meaning that nothing can be concluded concerning the effect of hole size and porosity. Also, it can be concluded that under specific circumstances (high shock strength), a porous plate-covered cavity can function as a flow control device for the reduction of turbulence in the downstream boundary layer.

The question "How is the flow separation region affected by the presence of the porous plate-covered cavity?" can be answered by the results of Table 5.2. Flow separation seems to generally increase due to the presence of a porous plate-covered cavity, and the prospects of it being used as a flow control device for reducing or preventing separation seem dim. One would expect that the flow from the holes in the upstream part of the plate would act as boundary layer bleed (as discussed in subsection 2.6.3), make the boundary layer profile more full, and prevent or reduce separation, but the opposite seems true. Concerning the effect of hole size and porosity, it seems that large hole size and low porosity values cause for less flow separation, and perhaps a design for a succesful flow control device reducing separation can be found more in this direction. Concerning shock strength, it seems to be the case that a higher shock strength causes a larger area of separation, for regular flow as well as the cases with the porous plate-covered cavity.

Some light can be shed on the fourth question, ”How is the interaction length affected by the presence of the porous plate-covered cavity?” by the results of Table 5.1. However, as was already mentioned in the accompanying section, these must be interpreted with care. The interaction length is determined by the distance between the impingement location of the incident shock and the location at which the reflected shock emanates. The former of these is determined by the position of the wedge, and the latter by the thickening of the boundary layer (which is in turn determined by shock strength) in a regular, dummy plate interaction, while it is heavily influenced by the x-location of the start of the porous plate-covered cavity in the case this is present. In the case of a plate with small holes (e.g. 0.5mm), the start of the porous plate-covered cavity seems to singly determine the location of the reflected shock. In the case of larger holes, it seems to *mostly* influence it, because the fan of compression waves start here and the reflected shock is formed by these waves' convergence. This effect is also visible in the results of Table 5.1: for larger hole sizes, the interaction length is smaller, because the compression waves from the holes are stronger and continue on for longer downstream, making the location where the reflected shock converges move more downstream. Concerning porosity, it is also visible that a decrease in porosity decreases interaction length, albeit only with a significant effect for the higher shock strength. Judging from the Schlieren images this seems to be because at the downstream end of the fan of compression waves, the waves are darker, and the converged reflected shock is more downstream. Concerning the influence of shock strength, it seems to be the case that a higher shock strength causes more rapid deceleration to subsonic flow and that less compression waves will emanate from the holes, namely, only from the upstream holes. As stated earlier, the reflected shock is formed by the convergence of these compression waves, so a higher shock strength causes a higher interaction length, which is also visible in the results of Table 5.1. However, finally it must be reiterated that more than the effects stated thus far, the streamwise position of the start of the porous plate-covered cavity is the most influential factor on the interaction length.

7.3 Recommendations

As can be read above, a few general correlations can be concluded from the results that have been obtained. However, each of these correlations are described with respect to shock strength, plate hole size or plate porosity, or the location of the start of the plate, meaning they have been drawn from 1, 2, or maybe 3 data points. More research definitely needs to be done in order to bring the necessary certainty to the conclusions. Therefore, this investigation recommends additional investigations to be done over a wider range of wedge angles, plate hole sizes, and plate porosities. Performing the investigation again with approximately 5 such values would be a huge improvement for the certainty of establishing a correlation. This means that a future investigation can likely only focus on one of these variables, but the present investigation, which had never been performed before, has in any case provided an impetus for such a detailed study.

Because the location of the start of the plate seems to be of overarching importance, it is recommended that a future investigation focuses itself on a range of cases whereby this is altered. Simultaneously, it is assumed best to keep the impingement location of the incident shock in the middle of the plate, to allow inflow downstream and outflow upstream. Thus, a design is recommended whereby the porous cavity is located in the middle of the plate and whereby its start and end are shifted upstream and downstream over various plates. An example of what such plates would look like if the same test section was used as for the present investigation is shown in Figure 7.1.

The Schlieren images used to compute the interaction lengths in section 5.3 were quite zoomed in, so that it was sometimes difficult to see what straight line could be drawn over the reflected shock. In other words, at the edge of the image, the reflected shock had not always completely coalesced into a straight line. If a further investigation attempts to calculate interaction lengths in the same way, it is advised that it does this with Schlieren images that are more zoomed out

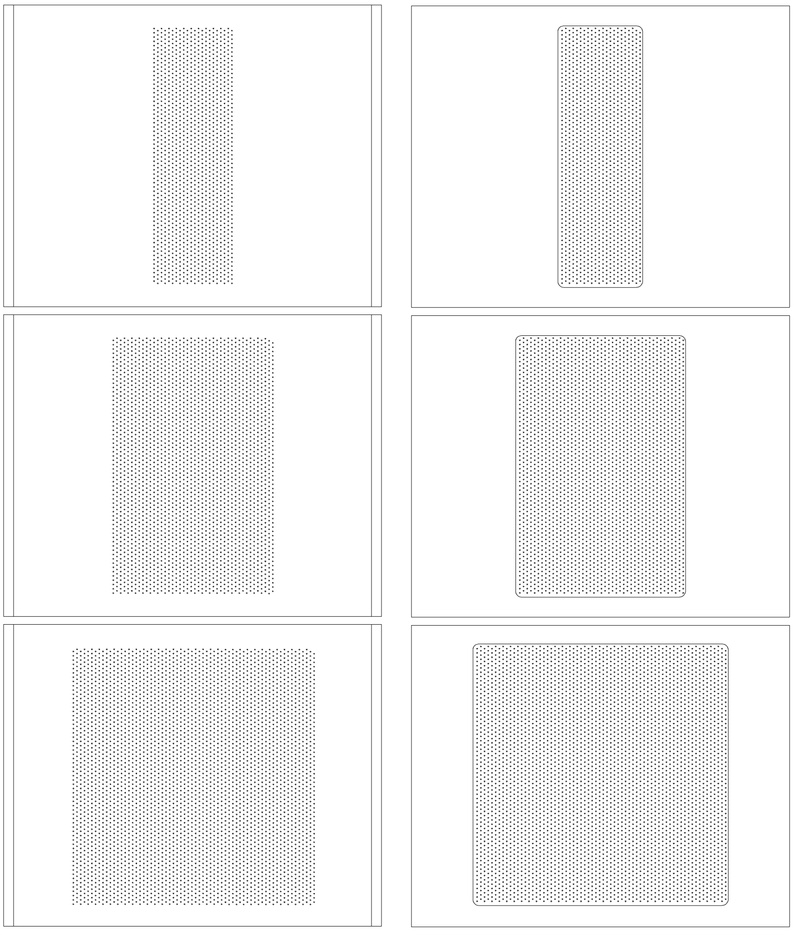

Figure 7.1: Top (left) and bottom (right) views of 3 plates for a recommended investigation.

to a larger field of view.

As Figure 6.6 showed in comparison with Figures 6.7 to 6.10, a highly turbulent region just before the shock impingement point has been spread out by the presence of a porous plate-covered cavity, so that the maximum values of turbulent kinetic energy have been reduced. This was not an aspect thoroughly looked at and discussed by the present investigation, but perhaps a future investigation would want to focus itself on how turbulence behaves just before the shock impingement point, and how a porous plate-covered cavity can reduce this.

BIBLIOGRAPHY

Akeret, J., Feldmann, F. and Rott, N. (1947), *Investigations of compression shocks and boundary layers moving in gases moving at high speed*, number 1113, NACA TM.

Allen, J., Heaslet, M. A. and Nitzberg, G. E. (1947), *The interaction of boundary layer and compression shock and its effect upon airfoil pressure distributions*, number A7A02, NACA RM.

Andreopoulos, J. and Muck, K. (1987), 'Some new aspects of the shock-wave/boundary-layer interaction in compression-ramp flows', *Journal of Fluid Mechanics* **180**, 405–428.

Anyiwo, J. and Bushnell, D. (1982), 'Turbulence amplification in shock-wave boundary-layer interaction', *AIAA Journal* **20**, 893–899.

Babinsky, H. and Harvey, J. (2011), *Shock Wave-Boundary-Layer Interactions.*, Cambridge University Press., Cambridge, United Kingdom.

Benay, R., Bur, B., Corbel, B. and Délery, J. (2000), Physical study of shock-wave/boundary-layer interaction control in transonic flow, *in* '38th Aerospace Sciences Meeting and Exhibit', American Institute of Aeronautics and Astronautics, Reno, Nevada, USA.

Beresh, S. J., Clemens, N. T. and Dolling, D. S. (2002), 'Relationship between upstream turbulent boundary-layer velocity fluctuations and separation shock unsteadiness', *AIAA Journal* **40**, 2412–2422.

Bohning, R. and Doerffer, P. (1995), 'Wind tunnel tests of shock/boundary layer interaction with passive control. porous wall flow investigation. numerical simulation of the wind tunnel tests'.

Breitling, T. (1985), Berechnung transsonischer, reibungsbehafterer Kanal- und Profilstr omungen mit passiver Beeinflussung, PhD thesis, Karlsruhe, Germany.

Brusniak, L. and Dolling, D. (1994), 'Physics of unsteady blunt-fin-induced shock wave/turbulent boundary layer interactions', *Journal of Fluid Mechanics* **273**, 375–409.

Bueno, P. C., Wagner, J. L., Searcy, J. A., Ganapathisubramani, N. T., Clemens, N. T. and Dolling, D. S. (2006), 'Experiments in unsteady forcing of mach 2 shock wave-boundary layer interactions', pp. 1–21.

Bur, B., Corbel, B. and Délery, J. (1998), 'Study of passive control in a transonic shock-wave/boundary-layer interaction', *AIAA Journal* **36**, 394–400.

Campo, L. M. (2014), *Effects of Shock Strength, Confinement, and Geometric Perturbations on Shock Boundary Layer Interactions*, Stanford University Press, Redwood City, CA, United States of America.

Chanetz, B. and Pot, T. (1987), Experiences fondamentales sur le controle passif de l'interaction onde de choc-couche limite en transsonique, *in* '24eme Colloque d'Aerodynamique Appliquee de l'AAAF', Office National D'Études et de Recherches Aerospatiales, Poitiers, France.

Chen, Y. (2008), 'Reflection of oblique shock wave', `http://doc.solvcon.net/en/latest/gas/oblique_shock_reflection.html`.

Clemens, N. T. and Narayanaswamy, V. (2014), 'Low-frequency unsteadiness of shock wave/-turbulent boundary layer interactions', *Annual Review of Fluid Mechanics* **46**, 469–492.

Davidson, T. S. and Babinsky, H. (2015), *Transition location effects on normal shock wave-boundary layer interactions*, Cambridge University Press, Cambridge, United Kingdom.

Délery, J. M. and Bur, R. (2000), *The Physics of shock wave/boundary layer interaction control: last lessons learned*, ECCOMAS 2000, Barcelona, Spain.

Délery, J. M. and Marvin, J. G. (1986), *Shock-wave boundary layer interactions*, number 280, AGARDograph.

Donker Duyvis, F. J. (2005), 'Laser sheet probe design for piv in high-speed wind tunnels'.

Donovan, J. F. (1996), 'Control of shock wave/turbulent boundary layer interactions using tangential injection', pp. 1–22.

Dupont, P., Haddad, C. and Debive, J. F. (2006), 'Space and time organization in a shock induced boundary layer', *Journal of Fluid Mechanics* **559**, 255–277.

Edney, B. (1968), *Anomalous heat transfer and pressure distributions on blunt bodies at hypersonic speeds in the presence of an impinging shock*, number 115, FFA Report, Stockholm, Sweden.

Erengil, M. E. and Dolling, D. S. (1991), 'Unsteady wave structure near separation in a mach 5 compression ramp interaction', *AIAA Journal* **29**, 728–735.

Fage, A. and Sargent, R. F. (1947), Shock-wave and boundary-layer phenomena near a flat surface, *in* 'Proceedings of the Royal Society', Vol. 190, pp. 1–20.

Gad-el Hak, M. (2001), *Flow Control*, CRC Press.

Gad-el Hak, M. and Bushnell, D. (1991), Status and outlook of flow separation control, *in* '29th Aerospace Sciences Meeting', American Institute of Aeronautics and Astronautics, Reno, NV, United States of America.

Gad-el Hak, M., Pollard, A. and Bonnet, J. (1998), *Flow Control: Fundamentals and Practices*, Springer-Verlag, Berlin, Germany.

Ganapathisubramani, B., Clemens, N. T. and Dolling, D. S. (2006), Planar imaging measurements to study the effect of spanwise structure of upstream turbulent boundary layer on shock induced separation, *in* '44th AIAA Aerospace Sciences Meeting and Exhibit', Reno, NV, United States of America.

Ganapathisubramani, B., Clemens, N. T. and Dolling, D. S. (2007), Effects of upstream coherent structures on low-frequency motion of shock-induced turbulent separation, *in* '45th AIAA Aerospace Sciences Meeting and Exhibit', Reno, NV, United States of America.

Gefroh, D., Loth, E., Dutton, C. and McIlwain, S. (2002), Control of an oblique shock/boundary-layer interaction with aeroelastic mesoflaps, *in* 'AIAA Journal', Vol. 40, pp. 2456–2466.

Giepman, R. H. (2016), Flow control for oblique shock wave reflections, PhD thesis, Delft, the Netherlands.

Ginoux, J. J. (1973), 'Interaction entre ondes de choc et couches limites', *Chocs et Ondes de Choc* **II**, 1–65.

Graham, R. H. and Miller, J. K. (2008), *Flying the SR-71 Blackbird: In the Cockpit on a Secret Operational Mission*, MBI Publishing Company, Washington DC, United States of America.

Hamed, A., Yeuan, J. J. and Shih, S. H. (1995), 'Shock-wave/boundary-layer interactions with bleed part 1: Effect of slot angle', *Journal of Propulsion and Power* **11**, 1231–1235.

Houwing, A. F., Smith, D. R., Fox, J. S., Danehy, P. M. and Mudford, N. R. (2001), 'Laminar boundary layer separation at a fin-body junction in a hypersonic flow', *Shock Waves* **11**, 31–42.

Humble, R. A. (2009), Unsteady Flow Organization of a Shock Wave-Boundary Layer Interaction, PhD thesis, Delft, the Netherlands.

Humble, R. A., Elsinga, G. E., Scarano, F. and Van Oudheusden, B. W. (2009), 'Three-dimensional instantaneous structure of a shock wave/turbulent boundary layer interaction', *Journal of Fluid Mechanics* **622**, 33–62.

Kallarbail, S. N. (2016), 'The 3d separation behaviour of a micro-ramp controlled oblique shock-wave reflection'.

Klebanoff, P. S. (1955), *Characteristics of Turbulence in a Boundary Layer with Zero Pressure Gradient*, number 1247, National Advisory Committee for Aeronautics.

McCormick, D. C. (1993), 'Shock/boundary-layer interaction control with vortex generators and passive cavity', *AIAA Journal* **31**.

Papamoschou, D. and Roshko, A. (1988), 'The compressible turbulent shear layer: an experimental study', *Journal of Fluid Mechanics* **197**, 453–477.

Piponniau, S. (2009), *Instationnarités dans les décollements compressibles: cas des couches limites soumises ondes de choc*, Université de Provence Aix-Marseille 1, Marseille, France.

Piponniau, S., Dussauge, J. P., Debive, J. F. and Dupont, P. (2009), 'A simple model for low-frequency unsteadiness in shock-induced separation', *Journal of Fluid Mechanics* **629**, 87–108.

Plotkin, K. J. (1972), *Shock Wave Oscillations Driven By Turbulent Boundary Layer Fluctuations*, National Aeronautics and Space Administration, Huntsville, AL, United States of America.

Poll, D. I. A., Danks, M. and Humphreys, B. E. (1992), The aerodynamic performance of laser drilled sheets. paper 92-02-02, *in* 'First European Forum on Laminar Flow Technology', Hamburg, Germany.

Purohit, S. (1987), *Effect of Vectored Suction on a Shock-Induced Separation*, Vikram Sarabhai Space Center, Trivandrum, India.

Raffel, M., Willert, C., Wereley, S. and Kompenhans, J. (2007), *Particle Image Velocimetry: A Practical Guide*, Springer-Verlag, Berlin, Germany.

Scarano, F. (2013), *Experimental Aerodynamics*, 1 edn, Delft University of Technology, Aerospace Engineering Department, Delft, The Netherlands.

Schofield, W. H. (1985), 'Turbulent-boundary-layer development in an adverse pressure gradient after an interaction with a normal shock wave', *Journal of Fluid Mechanics* **154**, 43–62.

Sino Defence Forum (2012), 'Sdf aerospace and aerodynamics corner', `https://www.sinodefenceforum.com/sdf-aerospace-and-aerodynamics-corner.t5801/page-24`.

Souverein, L. J. (2010), On the scaling and unsteadiness of shock induced separation, PhD thesis, Delft, the Netherlands.

Souverein, L. J., Dupont, P., Debiève, J.-F., Van Oudheusden, B. W. and Scarano, F. (2010), 'Effect of interaction strength on unsteadiness in shock-wave-induced separations', *AIAA Journal* **48**, 1480–1493.

Tambe, S. (2017), 'Effect of geometry on the downstream flow topology of micro ramps in supersonic turbulent boundary layer'.

Thomas, F., Putnam, C. and Chu, H. (1994), 'On the mechanism of unsteady shock oscillation in shock wave/turbulent boundary layer interaction', *Experiments in Fluids* **18**, 69–81.

Touber, E. and Sandham, N. (2008), 'Oblique shock impinging on a turbulent boundary layer: low-frequency mechanisms', *38th AIAA Fluid Dynamics Conference* .

Ünalmis, O. and Dolling, D. (1994), Decay of wall pressure field structure of a mach 5 adiabatic turbulent boundary layer, *in* '25th AIAA Fluid Dynamics Conference', American Institute of Aeronautics and Astronautics, Colorado Springs, CO, United States of America.

van Driest, E. R. (1956), 'On turbulent flow near a wall', *Journal of the Aeronautical Sciences* **23**, 1007–1011, 1036.

van Pelt, H. (2013), *Flow modelling in supersonic flows over surfaces with large roughness heights*, Delft University of Technology, Delft, the Netherlands.

Visbal, M. (2014), *Viscous and inviscid interactions of an oblique shock with a flexible panel*, United States Air Force Research Laboratory, Wright-Patterson Air Force Base, Ohio.

von Neumann, J. (1943), *Oblique reflection of shocks, Explosive Research Report No. 12*, Navy Department Bureau of Ordinance, Washington DC, United States of America.

Weber, A., Schreiber, H., Fuchs, R. and Steinert, W. (2002), '3-d transonic flow in a compressor cascade with shock-induced corner stall', *Journal of Turbomachinery* **124**, 358–366.

Westerweel, J. and Scarano, F. (2005), 'Universal outlier detection for piv data', *Experiments in Fluids* **39**, 1096–1100.

Willems, S., Gulhan, A. and Esser, B. (2013), 'Shock induced fluid-structure interaction on a flexible wall in supersonic turbulent flow', *Progress in Flight Physics* **5**, 285–308.

Wu, M. and Martin, M. P. (2007), 'Direct numerical simulation of supersonic turbulent boundary layer over a compression ramp', *AIAA Journal* **45**, 879–889.

Wu, M. and Martin, M. P. (2008), 'Analysis of shock motion in shockwave and turbulent boundary layer interaction using direct numerical simulation data', *Journal of Fluid Mechanics* **594**, 71–83.

Zang, T. A., Hussaini, M. Y. and Bushnell, D. M. (1984), 'Numerical computations of turbulence amplification in shock-wave interactions', *AIAA Journal* **22**, 13–21.

Appendix A

Technical drawing porous plate 1

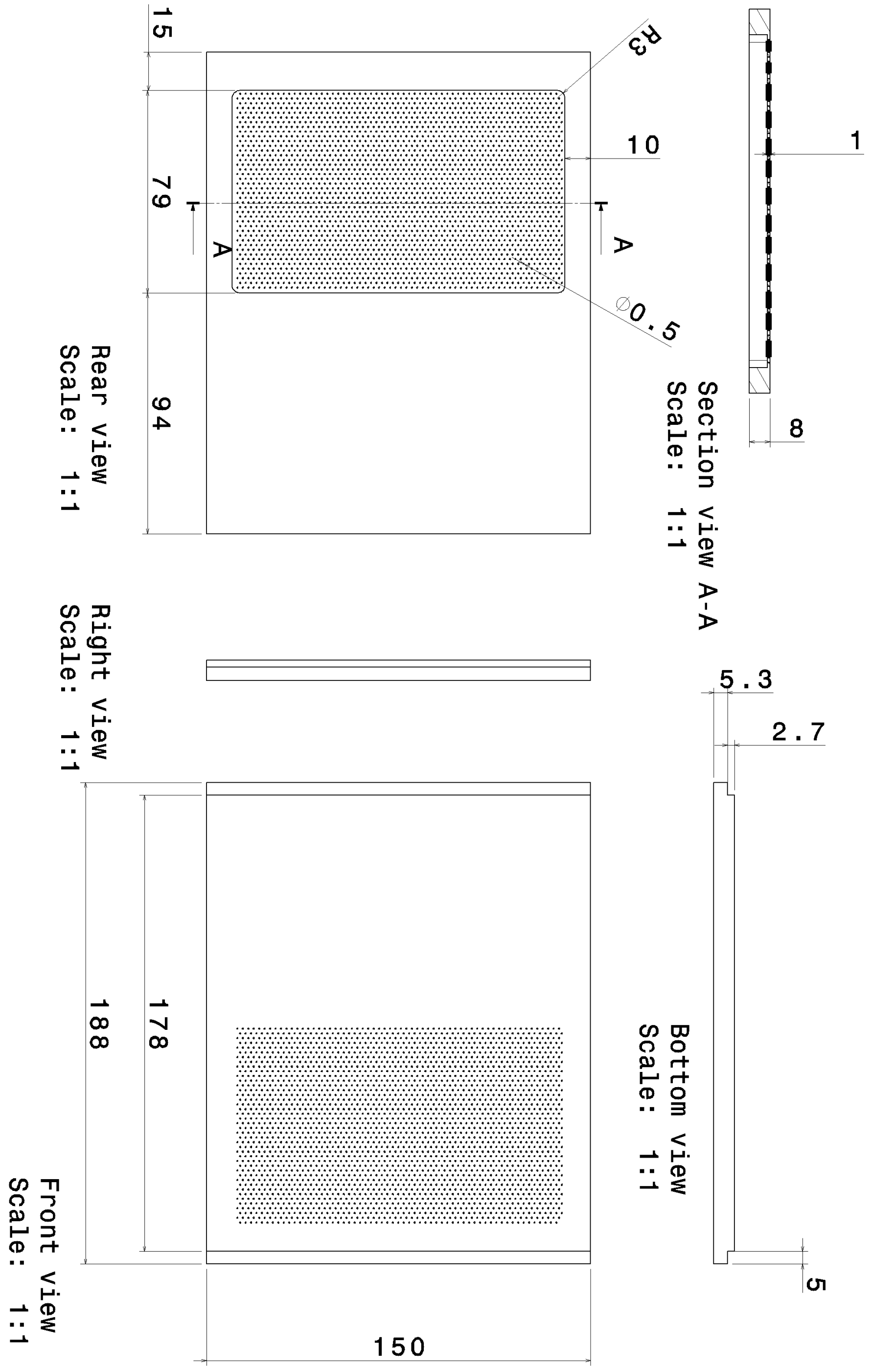

Appendix B

SHOCK IDENTIFICATION IMAGES

Wedge 5.0°, Dummy Plate

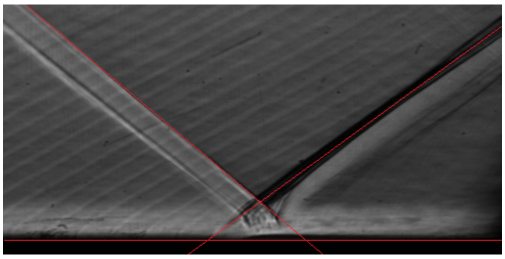

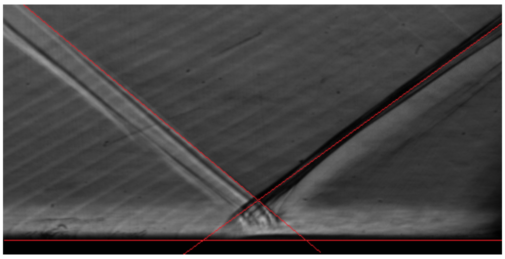

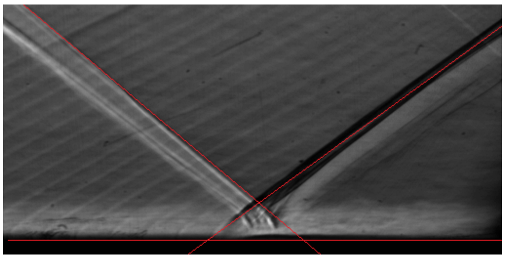

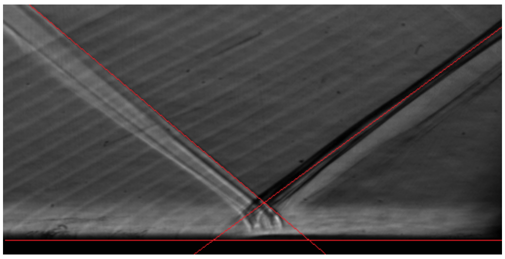

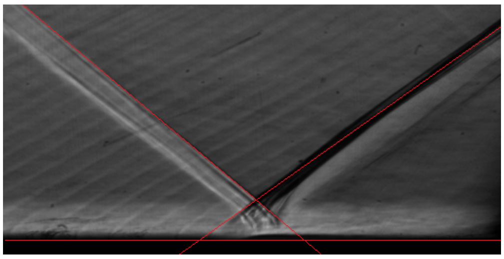

Wedge 5.0°, 0.5mm holes, 5% porosity plate

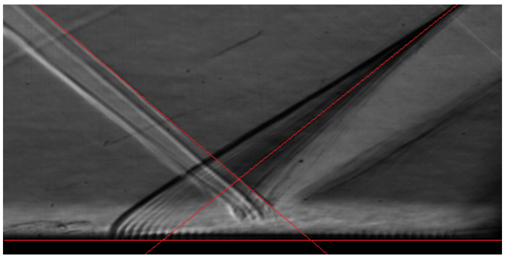

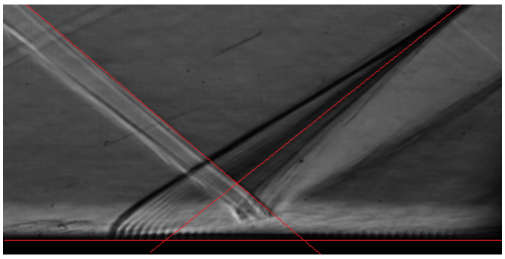

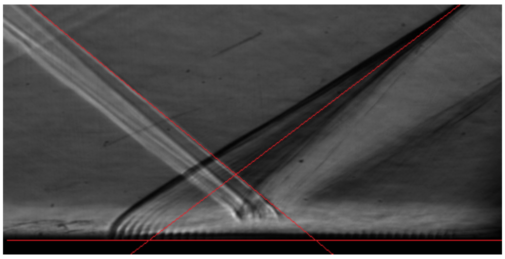

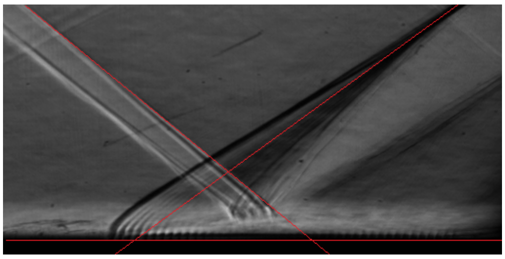

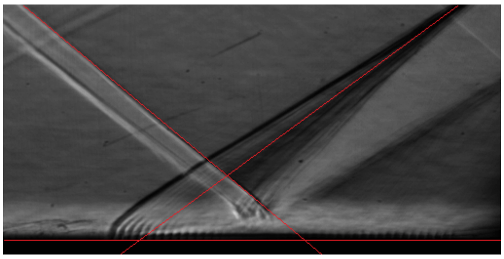

Wedge 5.0°, 1.0mm holes, 5% porosity plate

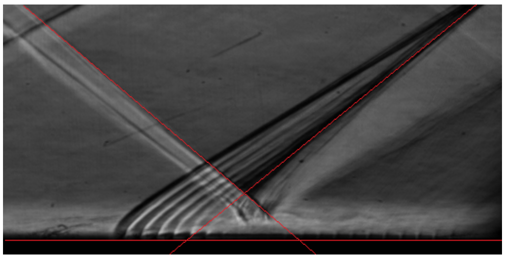

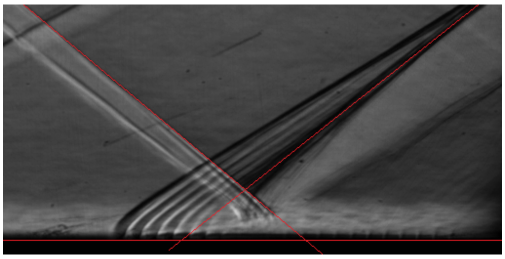

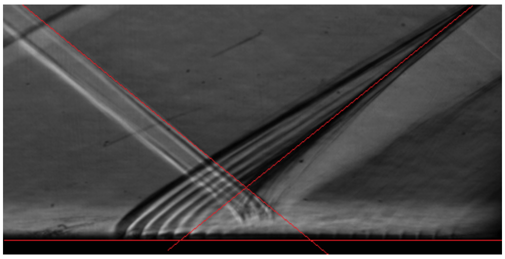

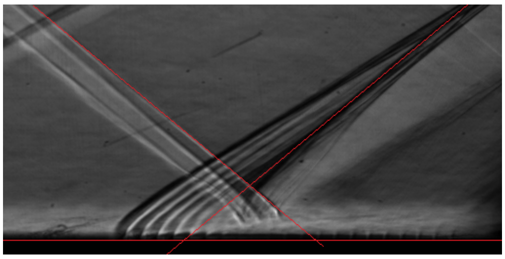

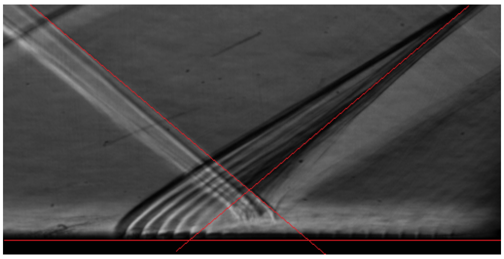

Wedge 5.0°, 1.5mm holes, 5% porosity plate

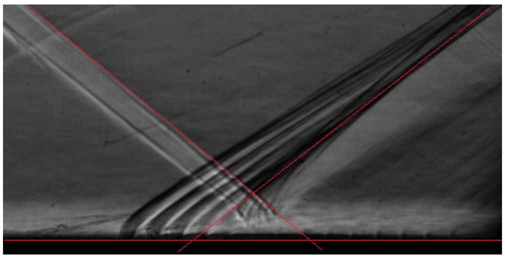

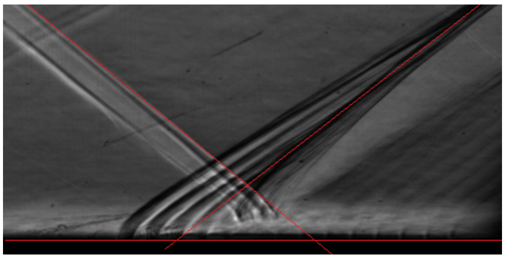

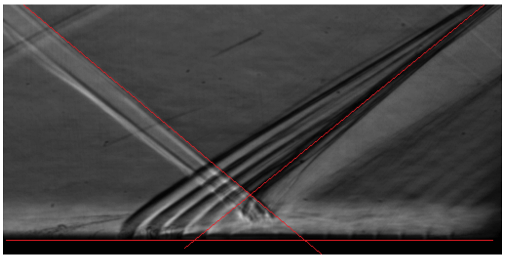

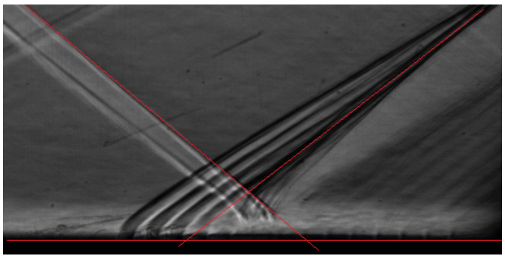

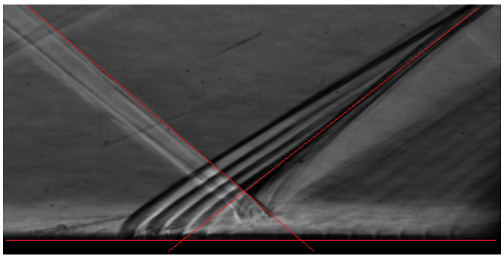

Wedge 5.0°, 1.0mm holes, 2.5% porosity plate

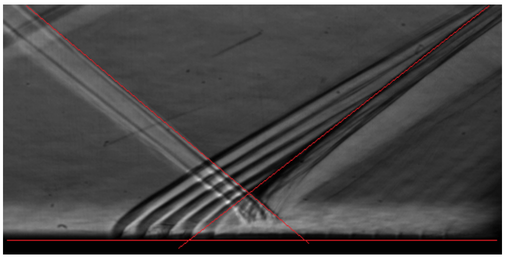

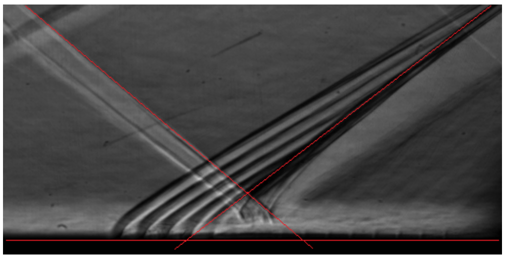

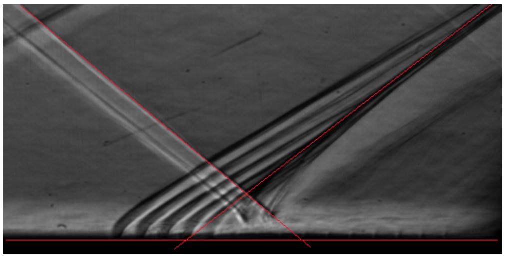

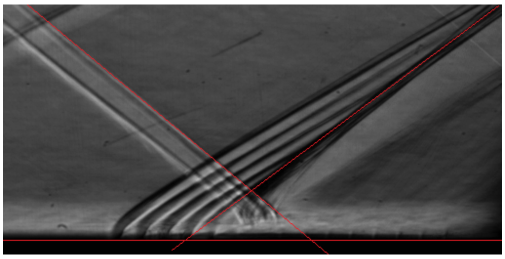

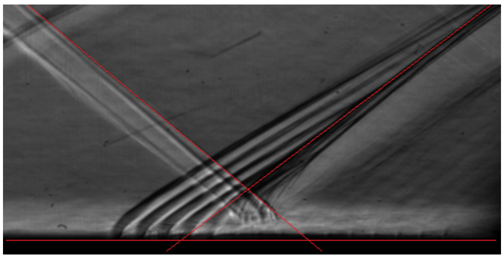

Wedge 8.8°, Dummy Plate

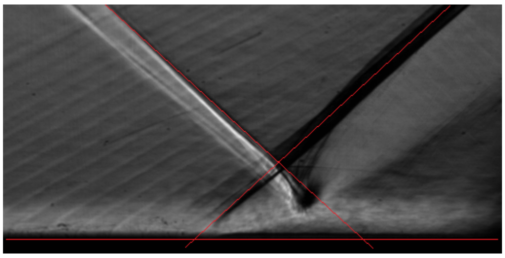

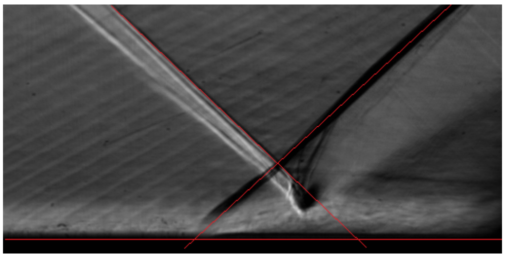

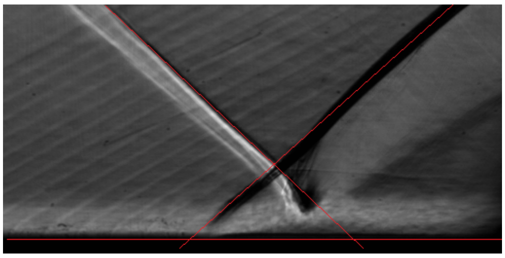

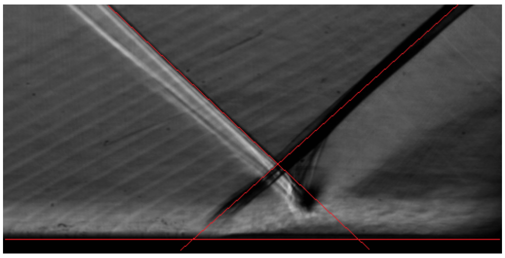

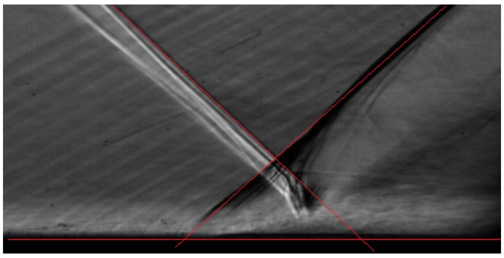

Wedge 8.8°, 0.5mm holes, 5% porosity plate

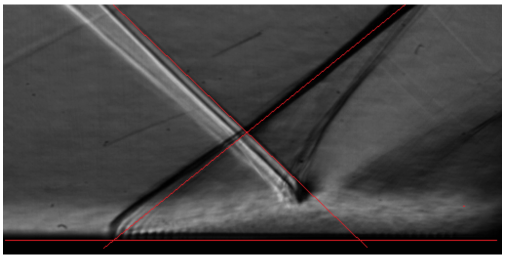

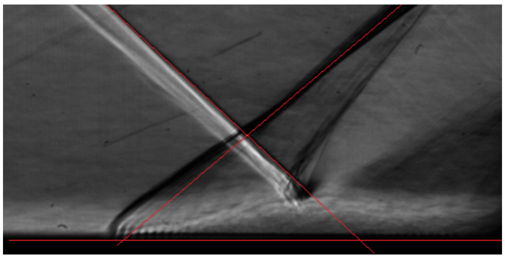

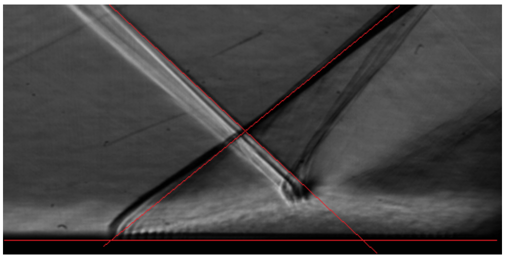

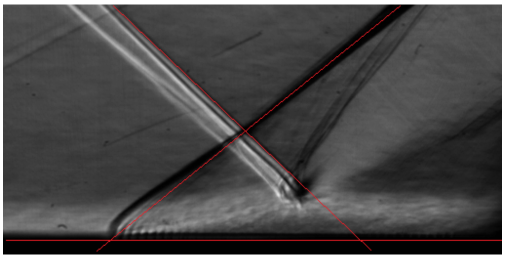

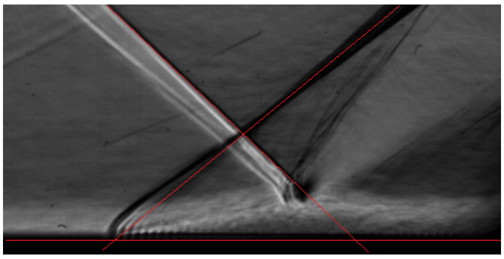

Wedge 8.8°, 1.0mm holes, 5% porosity plate

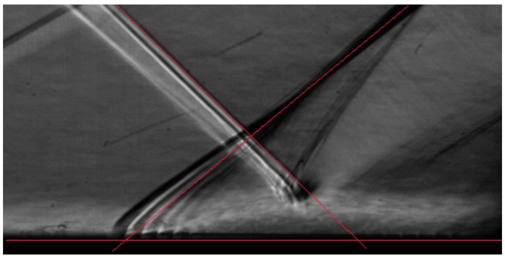

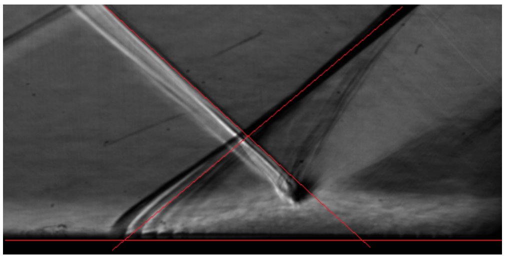

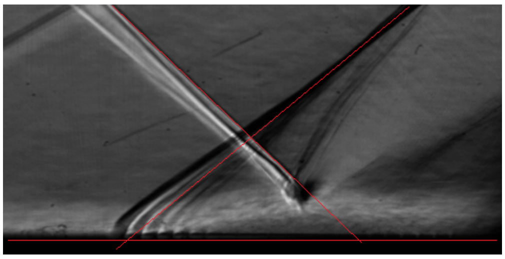

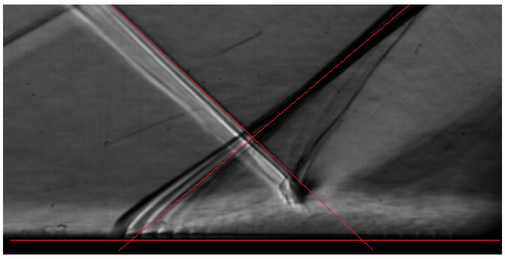

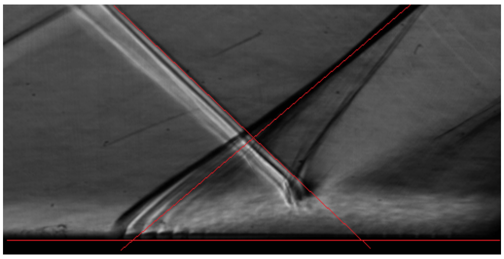

Wedge 8.8°, 1.5mm holes, 5% porosity plate

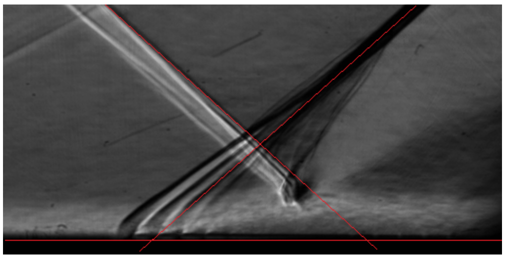

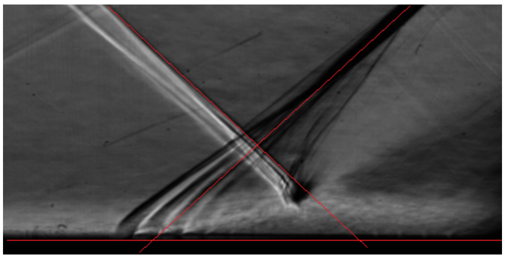

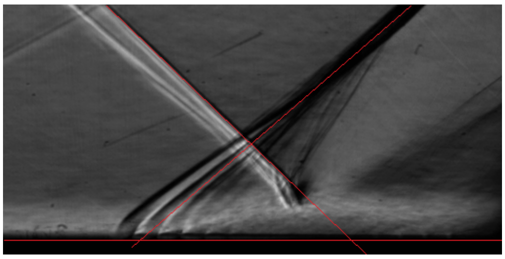

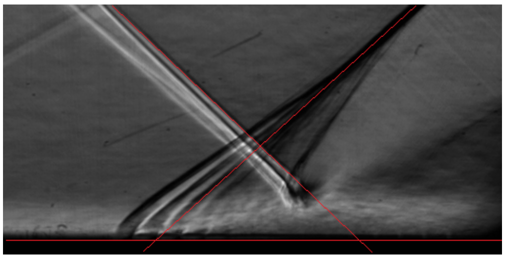

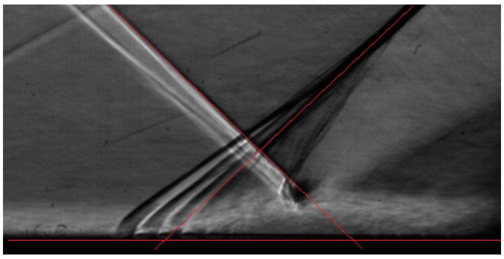

Wedge 8.8°, 1.0mm holes, 2.5% porosity plate

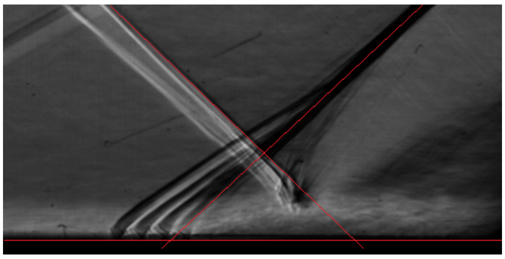

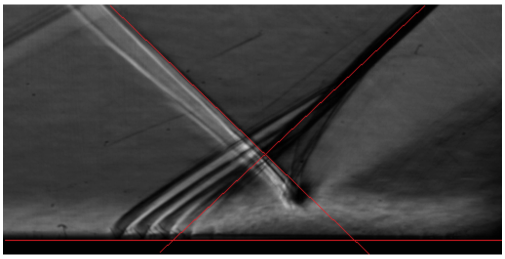

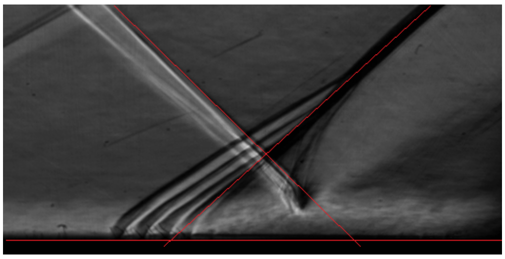

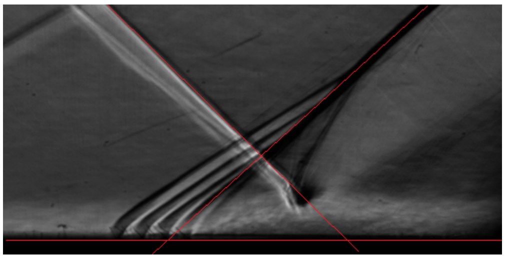

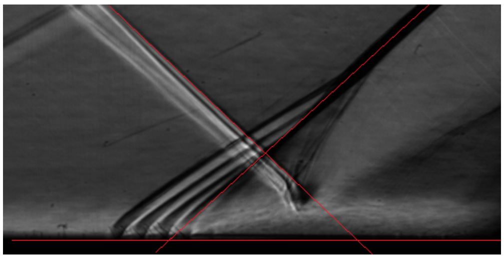

Appendix C

Integration heights for displacement and momentum thickness

Shown below are plots with the curves (plotted as red lines) which determined the height to which was integrated for the displacement and momentum thicknesses, for each case. These are plotted over contour plots of du/dy.

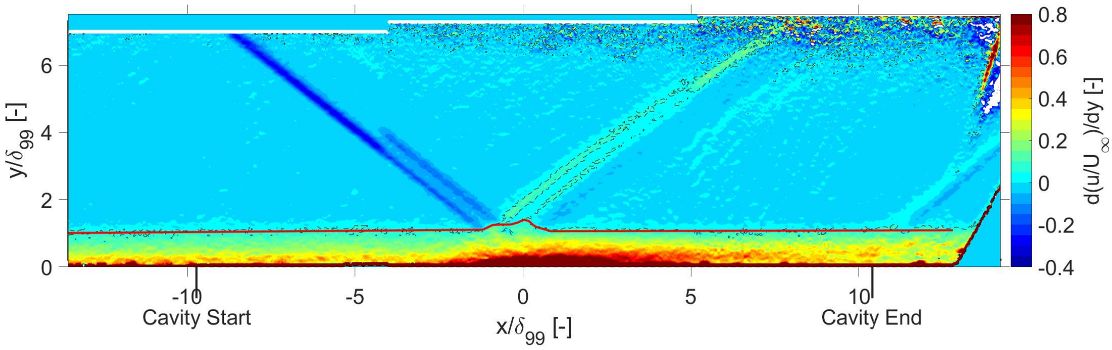

Figure C.1: Curve (in red) determining the height with which δ^* and θ were calculated, for 5.0° wedge, dummy plate

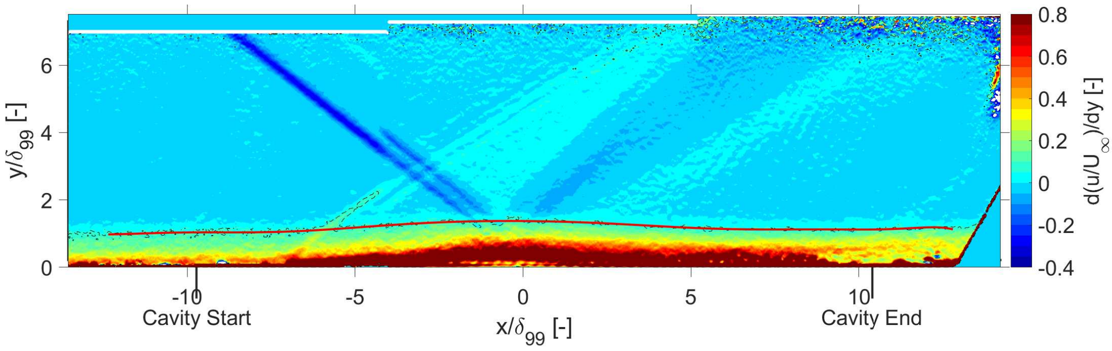

Figure C.2: Curve (in red) determining the height with which δ^* and θ were calculated, for 5.0° wedge, 0.5mm holes, 5% porosity plate

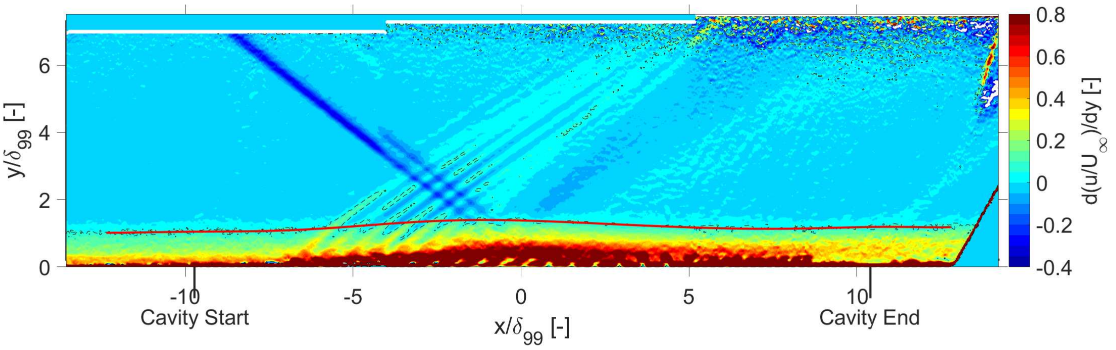

Figure C.3: Curve (in red) determining the height with which δ^* and θ were calculated, for 5.0° wedge, 1.0mm holes, 5% porosity plate

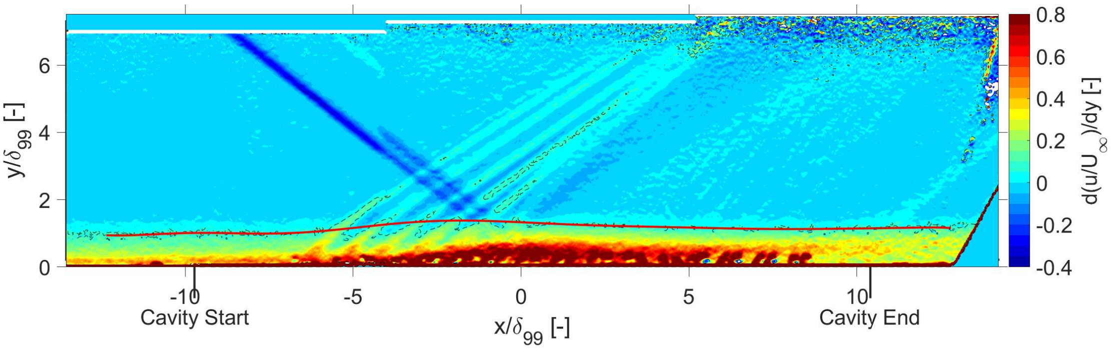

Figure C.4: Curve (in red) determining the height with which δ^* and θ were calculated, for 5.0° wedge, 1.5mm holes, 5% porosity plate

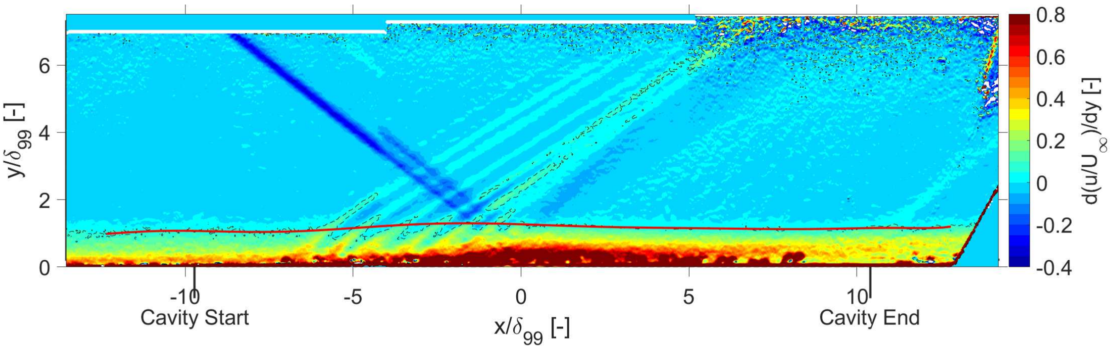

Figure C.5: Curve (in red) determining the height with which δ^* and θ were calculated, for 5.0° wedge, 1.0mm holes, 2.5% porosity plate

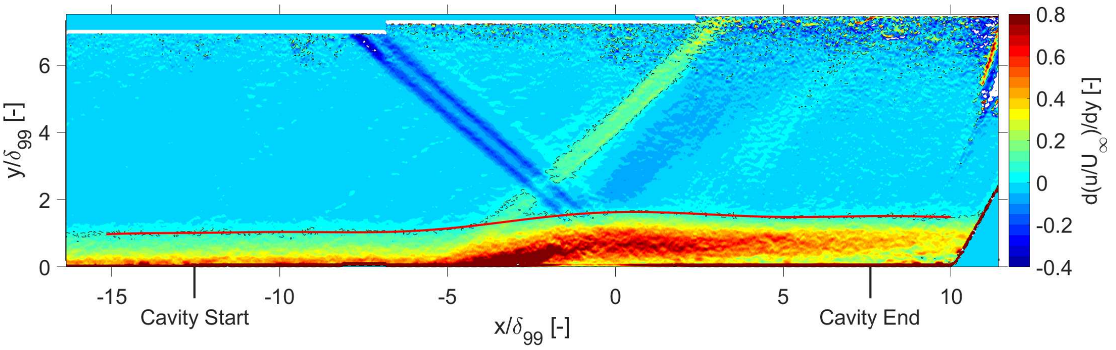

Figure C.6: Curve (in red) determining the height with which δ^* and θ were calculated, for 8.8° wedge, dummy plate

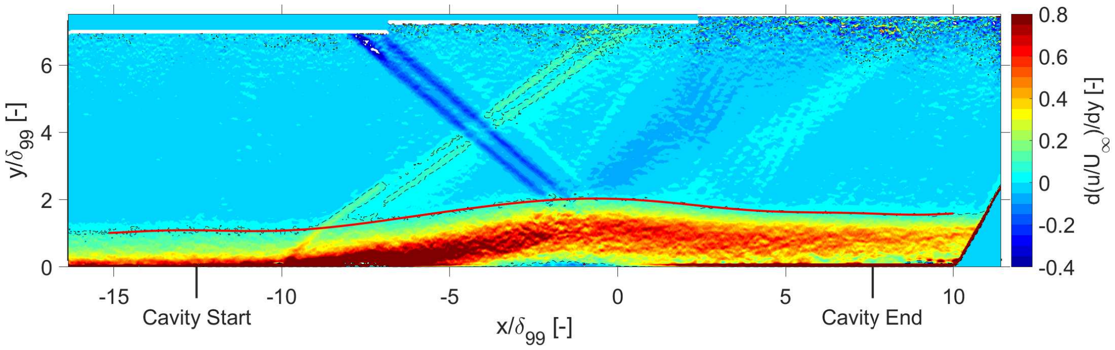

Figure C.7: Curve (in red) determining the height with which δ^* and θ were calculated, for 8.8° wedge, 0.5mm holes, 5% porosity plate

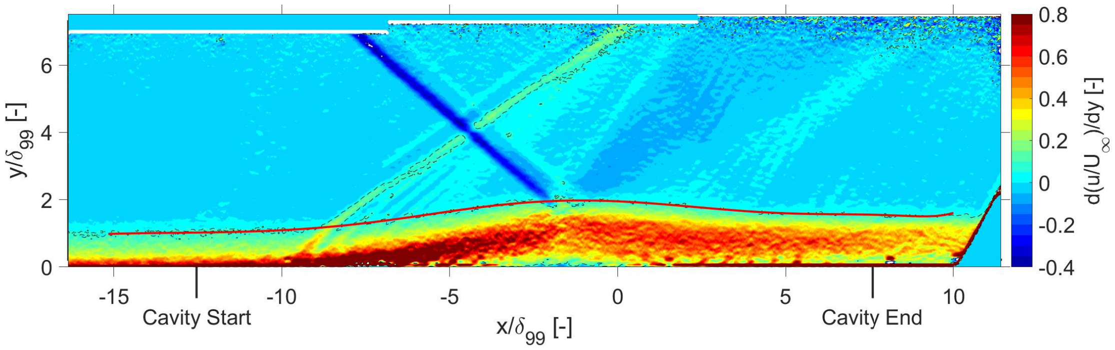

Figure C.8: Curve (in red) determining the height with which δ^* and θ were calculated, for 8.8° wedge, 1.0mm holes, 5% porosity plate

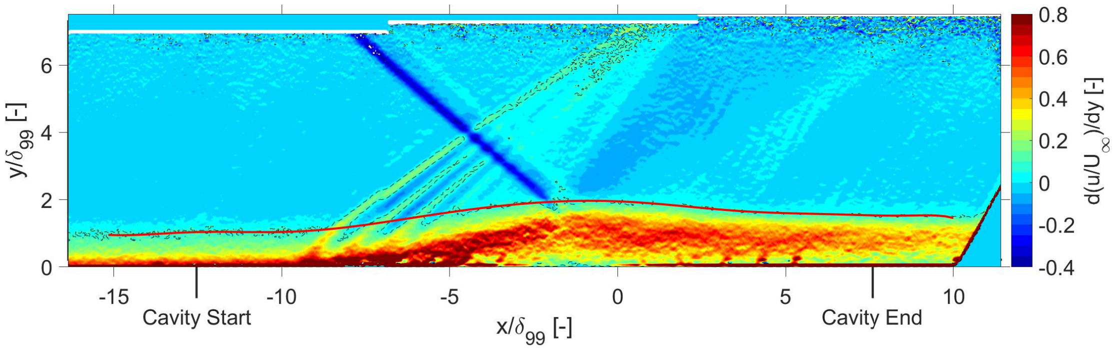

Figure C.9: Curve (in red) determining the height with which δ^* and θ were calculated, for 8.8° wedge, 1.5mm holes, 5% porosity plate

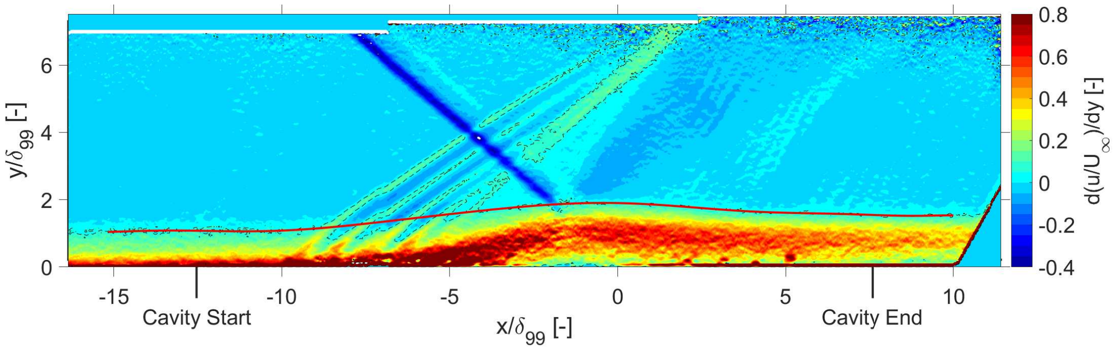

Figure C.10: Curve (in red) determining the height with which δ^* and θ were calculated, for 8.8° wedge, 1.0mm holes, 2.5% porosity plate

APPENDIX D

DETERMINING MASS FLUX THROUGH THE PLATES

In order to determine the mass flux through the porous section of the plate, a control volume approach was used. i.e. the fact that the sum of the mass flow into and out of a volume must equal zero. By calculating the mass flux (per unit of distance in the z-direction) into the left, top and right side of a rectangle, the mass flux on its bottom side could be found. The rectangle used had a height of the distance between 15 vectors and a width of the distance between 2 vectors. Through this method, the distribution of mass flux over the cavity could be found. These distributions showed a lot of scatter, so plots of them are omitted here. However, it was clearly visible that there was more positive mass flux (on the top side of the rectangle as well as its bottom side) at the upstream portion and more negative mass flux at its downstream portion, similar to the shapes of the curves of vertical velocity distributions that could be seen in Figures 5.26 and 5.27. For the 5.0° wedge cases, $x/\delta_{0,99} = -0.42$ separated the upstream and downstream portions, and for the 8.8° wedge this point was $x/\delta_{0,99} = -1.21$. The mass flux upstream and downstream of these points were integrated, and are shown in Table D.1.

Conservation of momentum trivially dictates that the magnitude of the flux going into the cavity must be equal to that going out of the cavity, i.e. that the sum of the third and fourth columns should equal zero. As can be seen from the table, the calculated fluxes deviate from this significantly, which casts doubt upon the accuracy of the method. Nevertheless, to get a better estimate of the in- and outgoing mass flux, the average of the magnitudes of both fluxes are shown as well in the right-most column.

Wedge angle [°]:	Plate:	Mass flux upstream [$\mathrm{kgm^{-1}s^{-1}}$]:	Mass flux downstream [$\mathrm{kgm^{-1}s^{-1}}$]:	Average mass flux [$\mathrm{kgm^{-1}s^{-1}}$]:
5.0	Dummy	0.08	-0.36	0.22
5.0	0.5mm holes, 5% porosity	0.20	-0.73	0.46
5.0	1.0mm holes, 5% porosity	0.14	-0.49	0.31
5.0	1.5mm holes, 5% porosity	0.07	-0.65	0.36
5.0	1.0mm holes, 2.5% porosity	0.11	-0.35	0.23
8.8	Dummy	-0.02	-0.13	0.05
8.8	0.5mm holes, 5% porosity	0.29	-0.27	0.28
8.8	1.0mm holes, 5% porosity	0.14	-0.34	0.24
8.8	1.5mm holes, 5% porosity	0.02	-0.27	0.14
8.8	1.0mm holes, 2.5% porosity	0.05	-0.16	0.11

Table D.1: Mass flux out of (in the upstream section) and into (in the downstream section) the porous section of the plate

The method can be seen to have succesfully predicted that for each wedge, more mass flows through the porous plates than the dummy plate. However, more evidence of the inaccuracy of the method (apart from the inequality of the ingoing and outgoing flux mentioned earlier) can be seen in the fact that the dummy plate's mass flux is not equal to zero for both wedges used, which is physically impossible. Looking at the relative magnitude of the mass fluxes per wedge, it can be seen that the 0.5mm plate had the highest mass flux, and the 2.5% porosity plate has the least. This corroborates the results seen in the vertical velocity distributions of Figures 5.26 and 5.27. However, the inaccuracy of the method is of such an extent that it cannot be deemed valid enough to draw any further conclusions.

Appendix E

Turbulence plots

E.1 $\overline{u'^2}$ turbulent normal stress flow fields

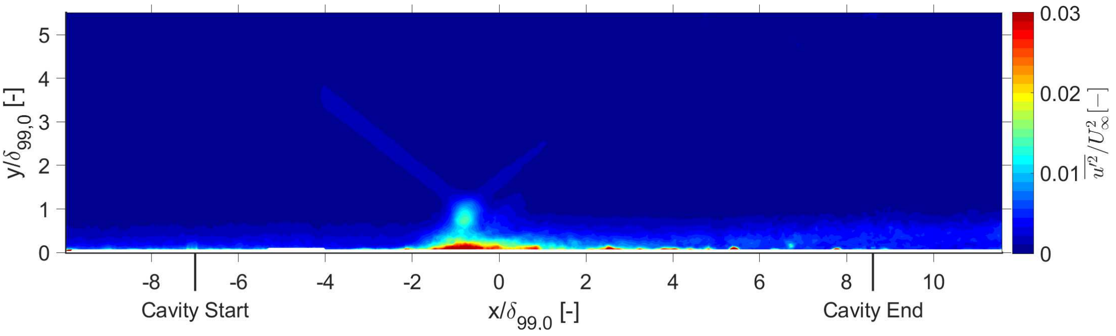

Figure E.1: $\overline{u'^2}$ flow field for 5.0° wedge and dummy plate

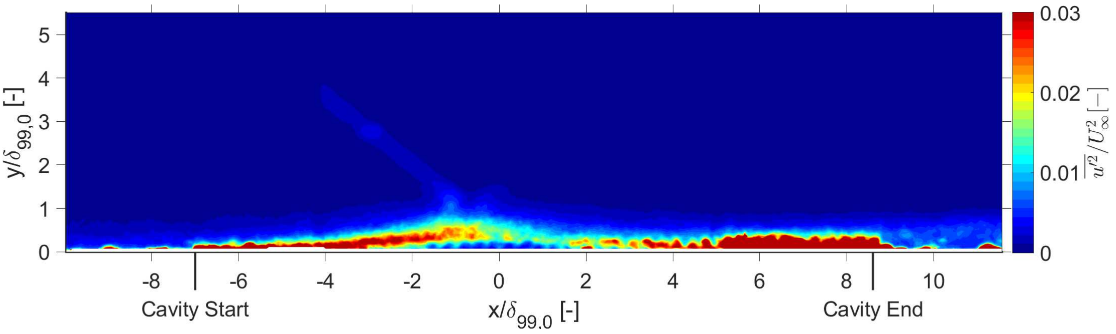

Figure E.2: $\overline{u'^2}$ flow field for 5.0° wedge and dummy plate

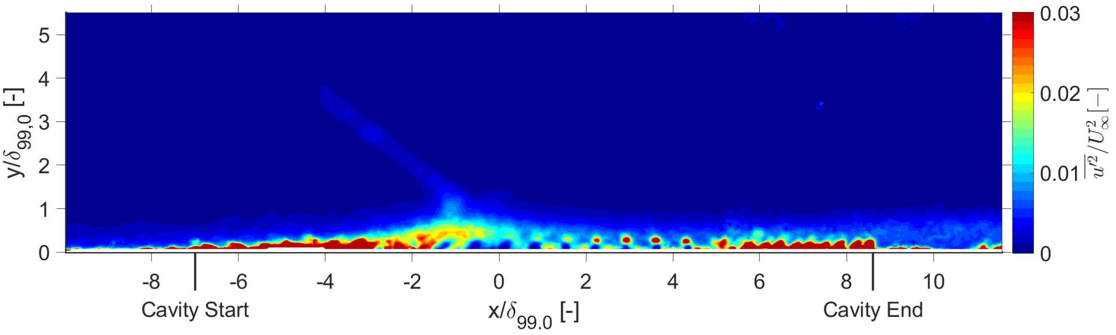

Figure E.3: $\overline{u'^2}$ flow field for 5.0° wedge and dummy plate

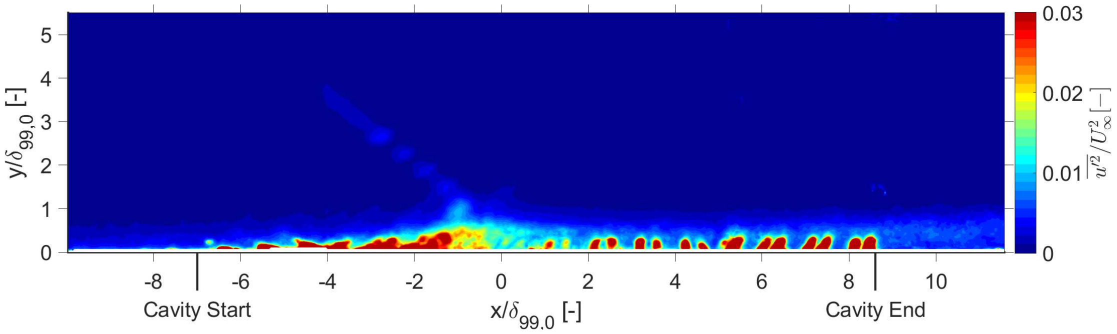

Figure E.4: $\overline{u'^2}$ flow field for 5.0° wedge and dummy plate

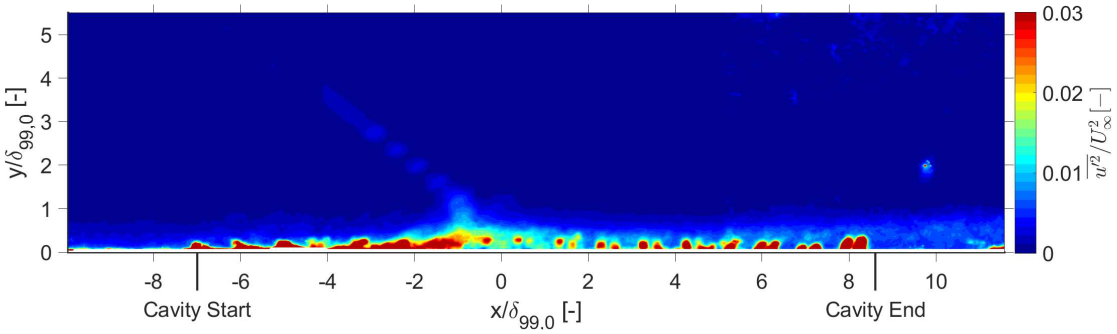

Figure E.5: $\overline{u'^2}$ flow field for 5.0° wedge and dummy plate

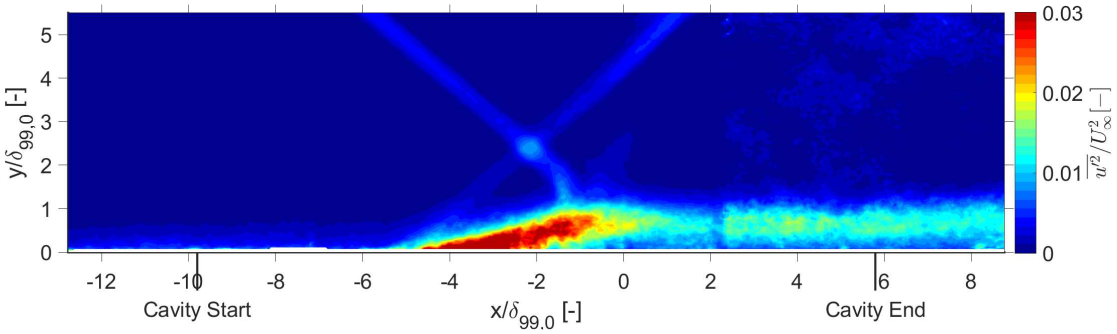

Figure E.6: $\overline{u'^2}$ flow field for 5.0° wedge and dummy plate

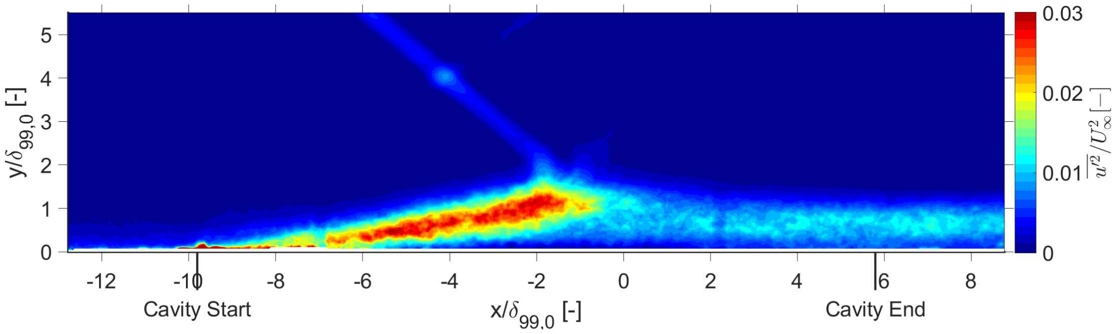

Figure E.7: $\overline{u'^2}$ flow field for 5.0° wedge and dummy plate

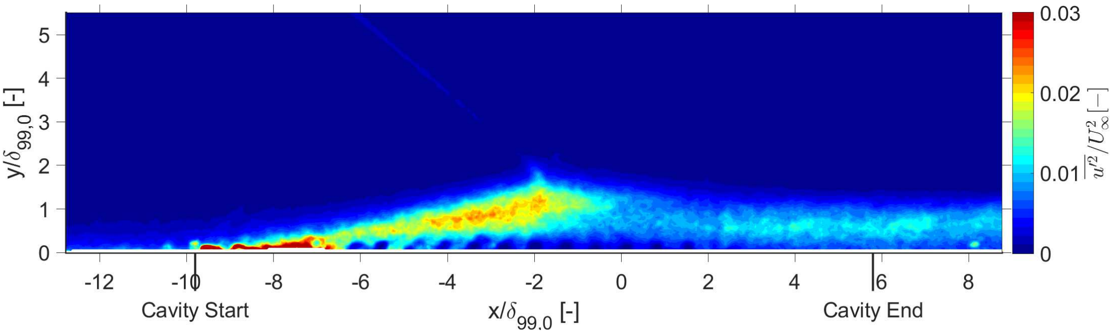

Figure E.8: $\overline{u'^2}$ flow field for 5.0° wedge and dummy plate

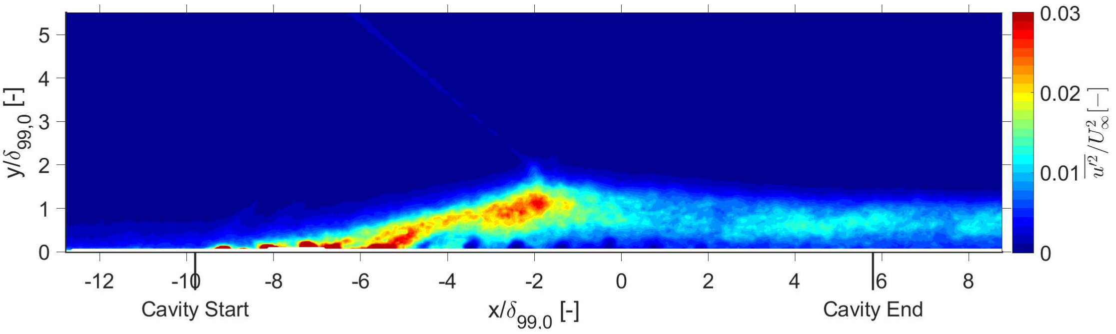

Figure E.9: $\overline{u'^2}$ flow field for 5.0° wedge and dummy plate

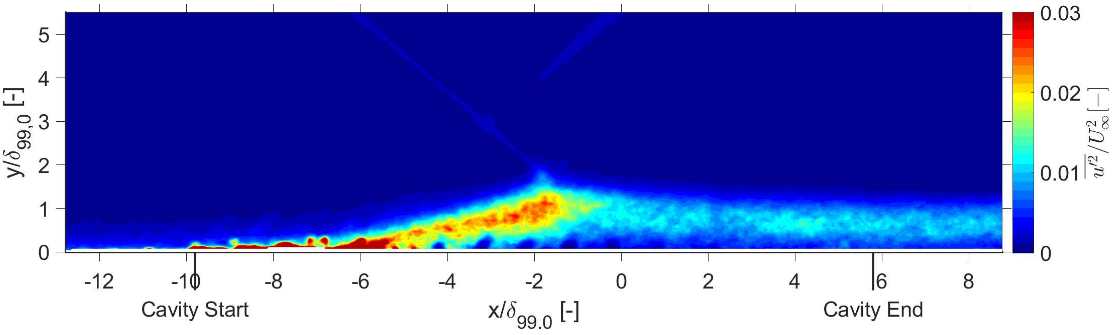

Figure E.10: $\overline{u'^2}$ flow field for 5.0° wedge and dummy plate

E.2 $\overline{v'^2}$ turbulent normal stress flow fields

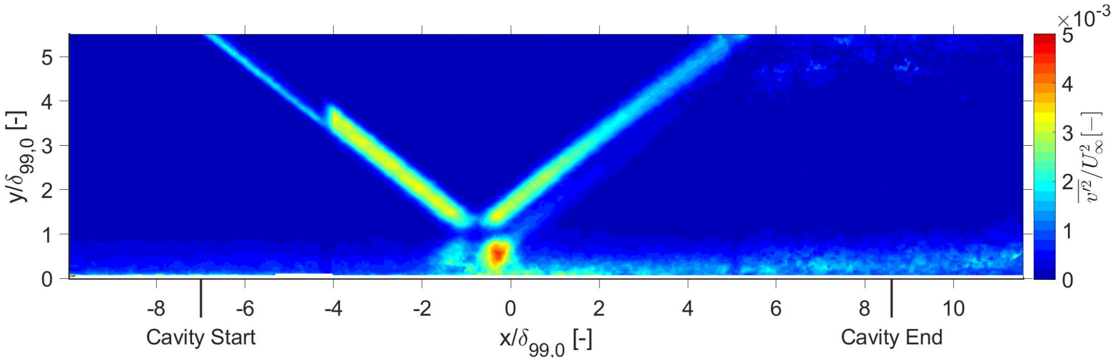

Figure E.11: $\overline{v'^2}$ flow field for 5.0° wedge and dummy plate

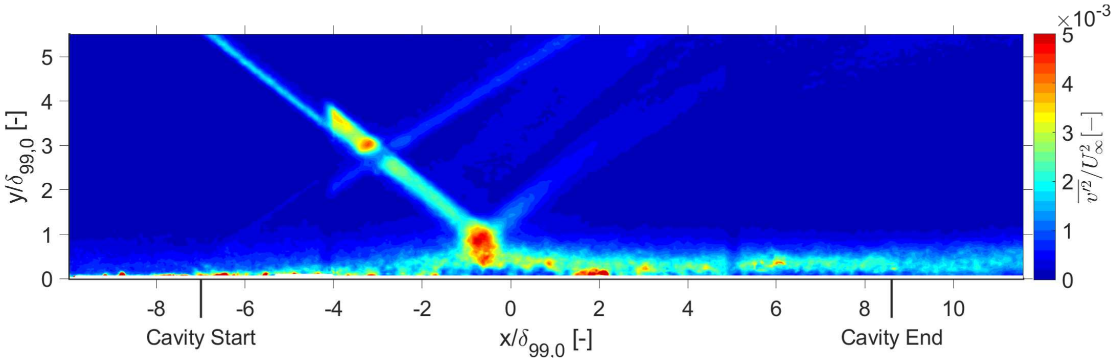

Figure E.12: $\overline{v'^2}$ flow field for 5.0° wedge and dummy plate

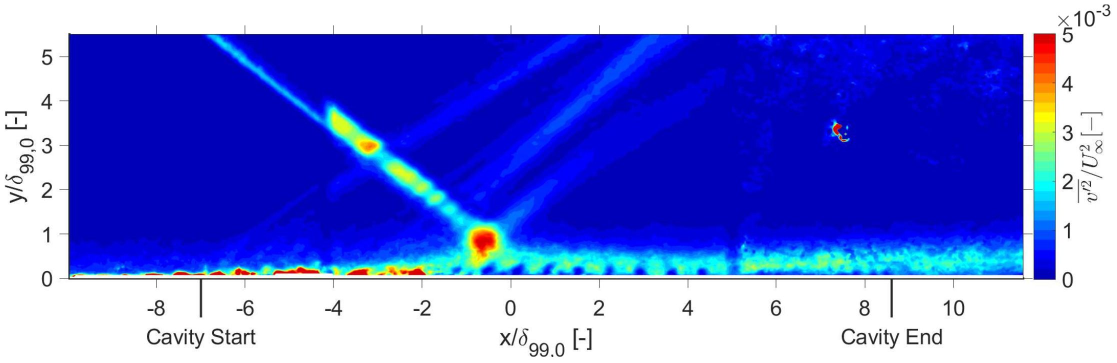

Figure E.13: $\overline{v'^2}$ flow field for 5.0° wedge and dummy plate

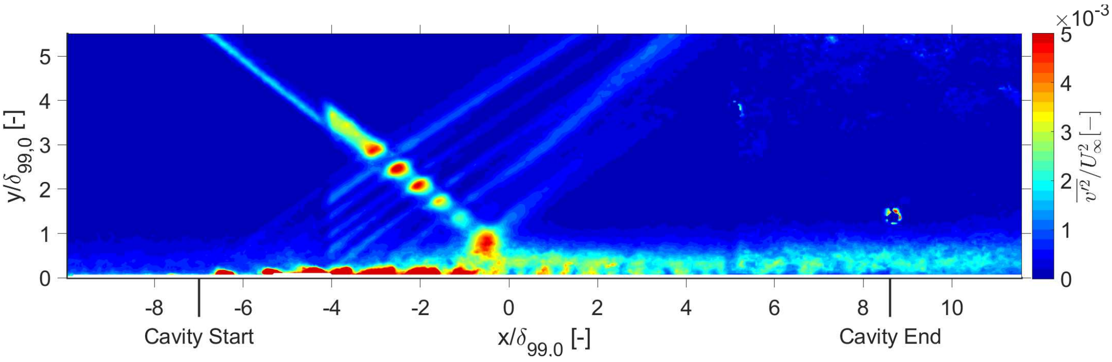

Figure E.14: $\overline{v'^2}$ flow field for 5.0° wedge and dummy plate

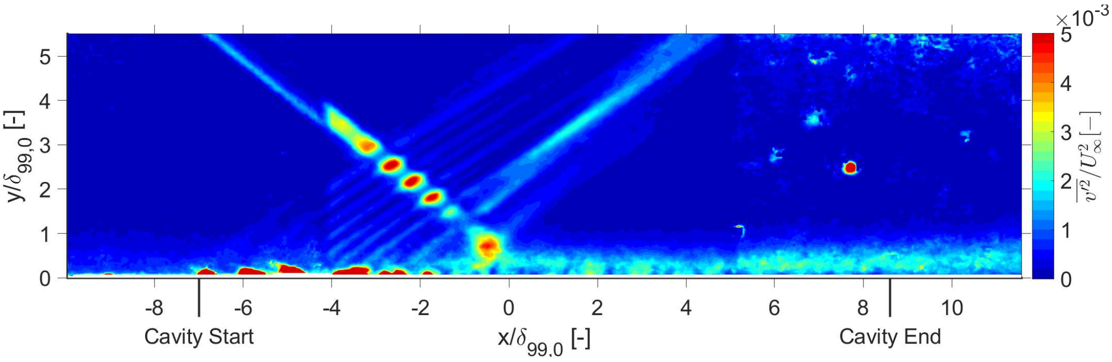

Figure E.15: $\overline{v'^2}$ flow field for 5.0° wedge and dummy plate

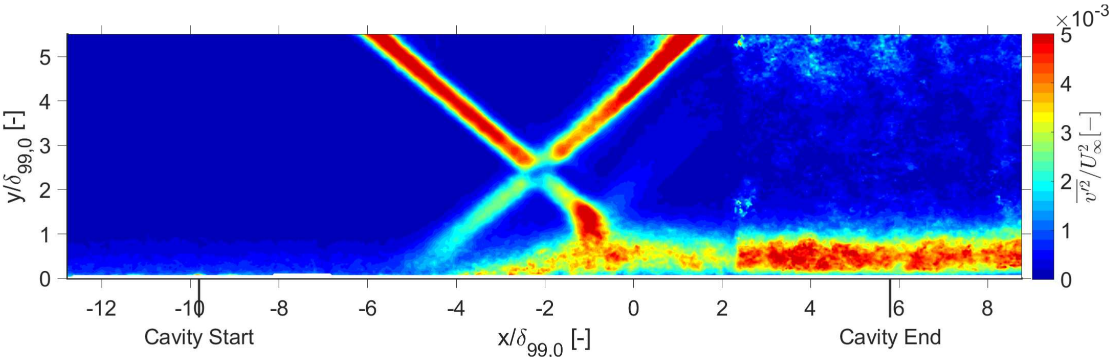

Figure E.16: $\overline{v'^2}$ flow field for 5.0° wedge and dummy plate

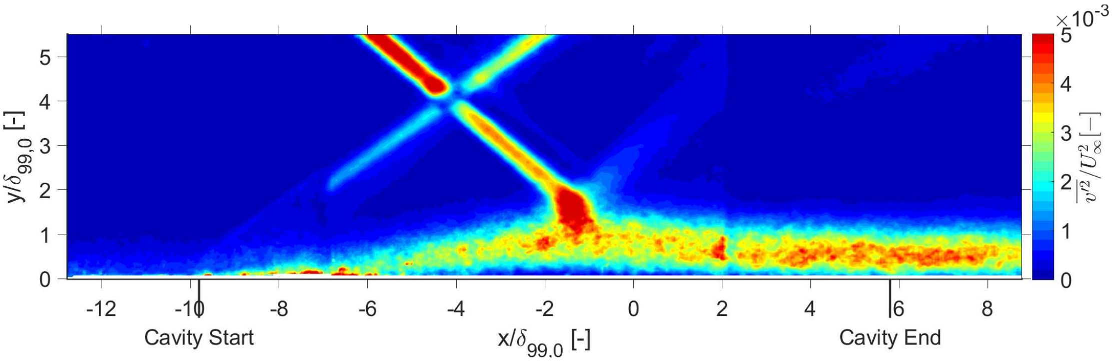

Figure E.17: $\overline{v'^2}$ flow field for 5.0° wedge and dummy plate

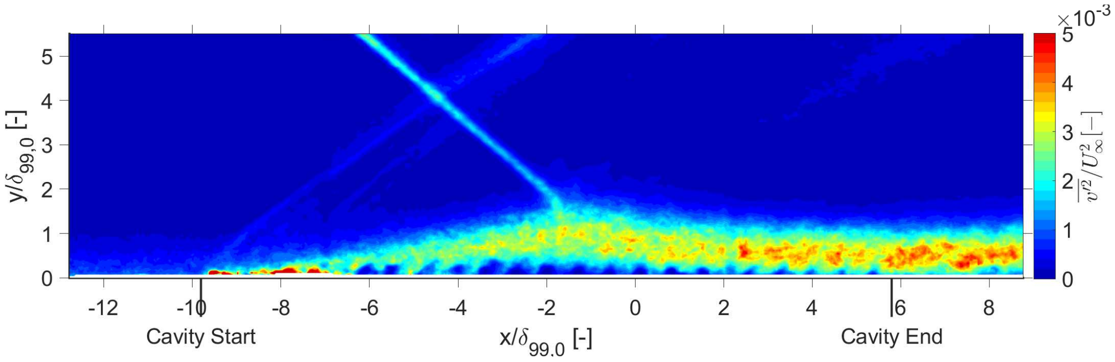

Figure E.18: $\overline{v'^2}$ flow field for 5.0° wedge and dummy plate

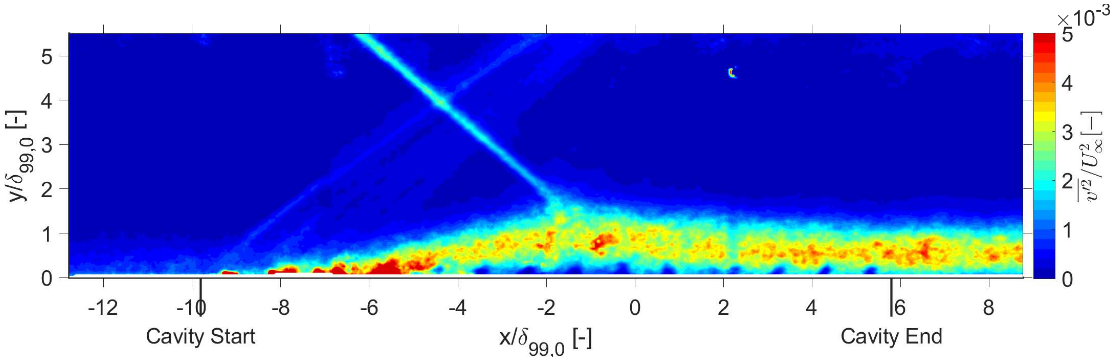

Figure E.19: $\overline{v'^2}$ flow field for 5.0° wedge and dummy plate

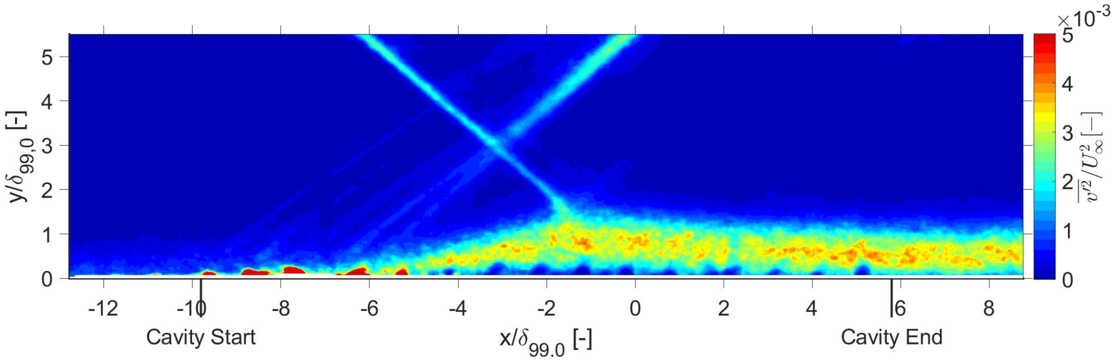

Figure E.20: $\overline{v'^2}$ flow field for 5.0° wedge and dummy plate

E.3 $\overline{u'v'}$ turbulent shear stress flow fields

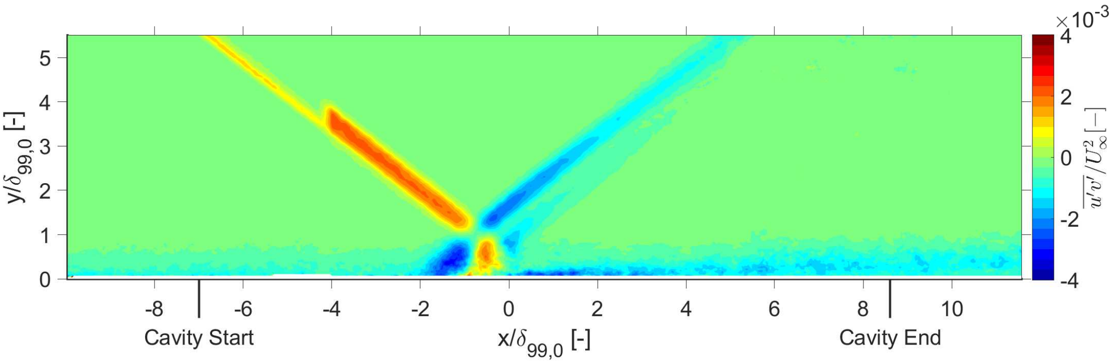

Figure E.21: $\overline{u'v'}$ flow field for 5.0° wedge and dummy plate

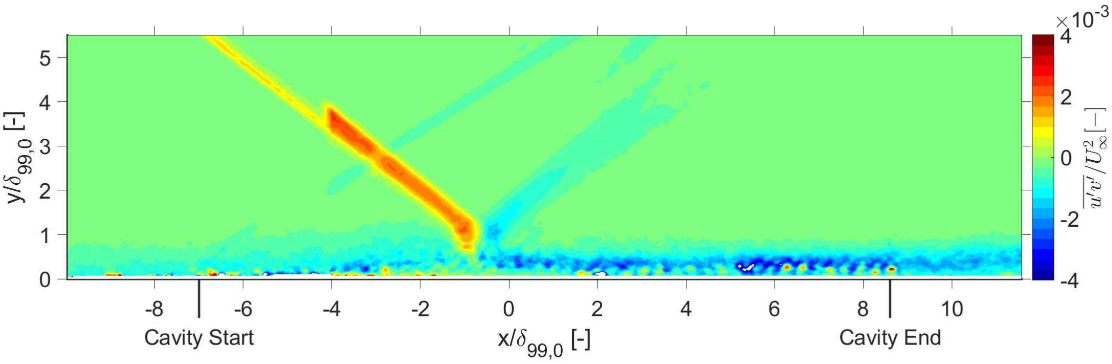

Figure E.22: $\overline{u'v'}$ flow field for 5.0° wedge and 0.5mm holes, 5% porosity plate

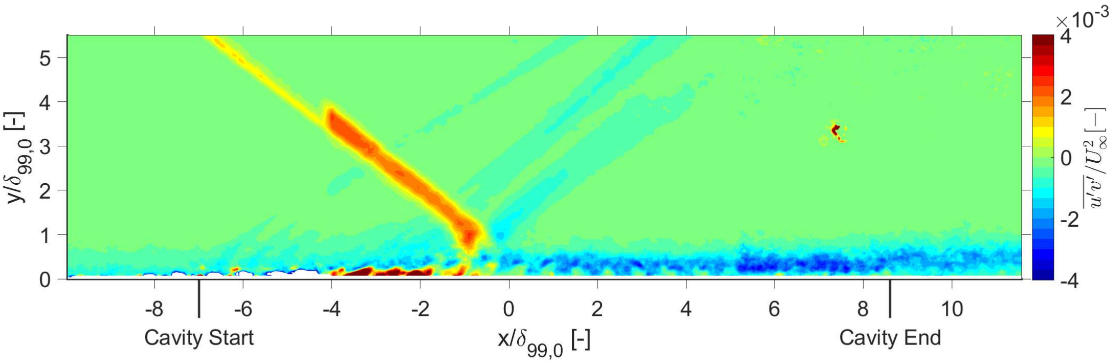

Figure E.23: $\overline{u'v'}$ flow field for 5.0° wedge and 1.0mm holes, 5% porosity plate

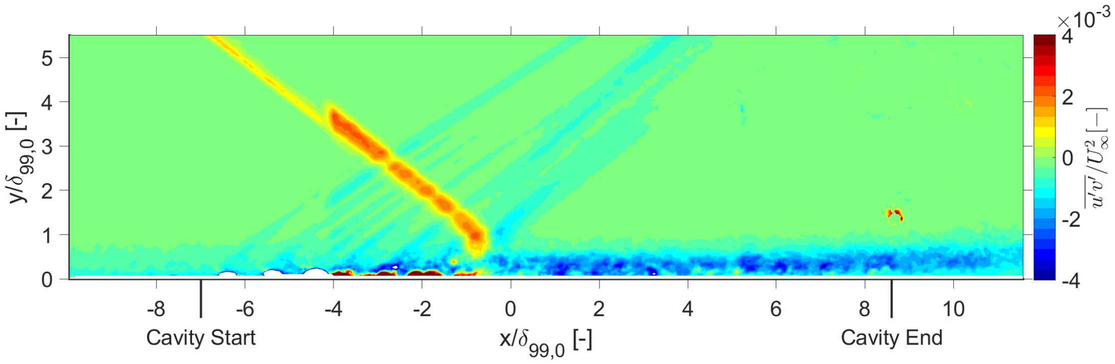

Figure E.24: $\overline{u'v'}$ flow field for 5.0° wedge and 1.5mm holes, 5% porosity plate

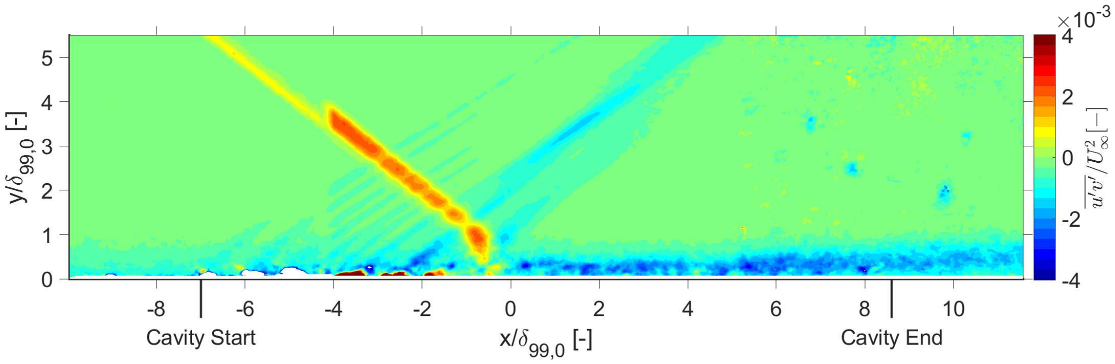

Figure E.25: $\overline{u'v'}$ flow field for 5.0° wedge and 1.0mm holes, 2.5% porosity plate

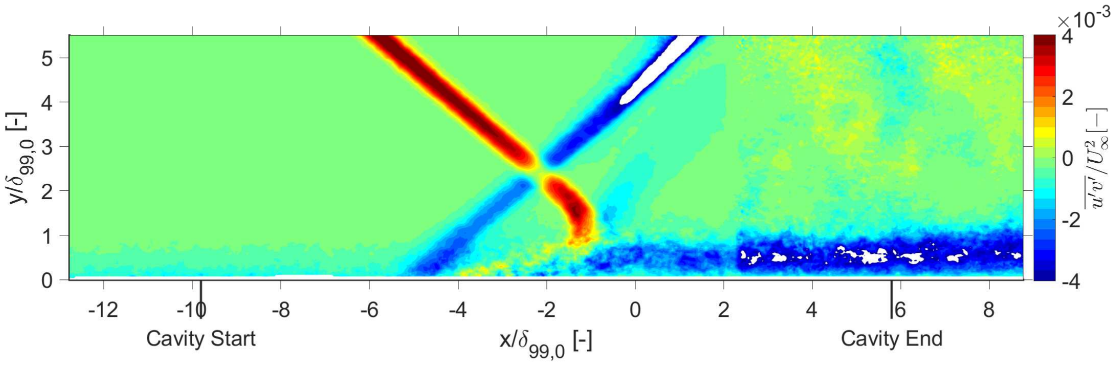

Figure E.26: $\overline{u'v'}$ flow field for 8.8° wedge and dummy plate

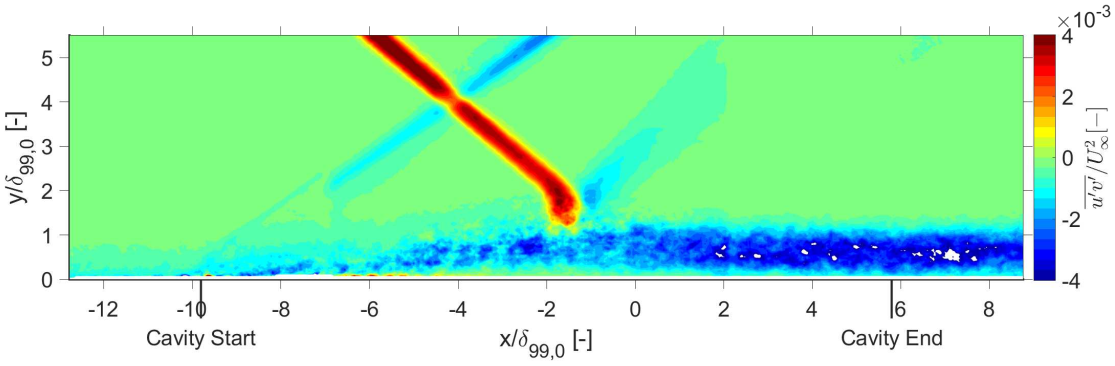

Figure E.27: $\overline{u'v'}$ flow field for 8.8° wedge and 0.5mm holes, 5% porosity plate

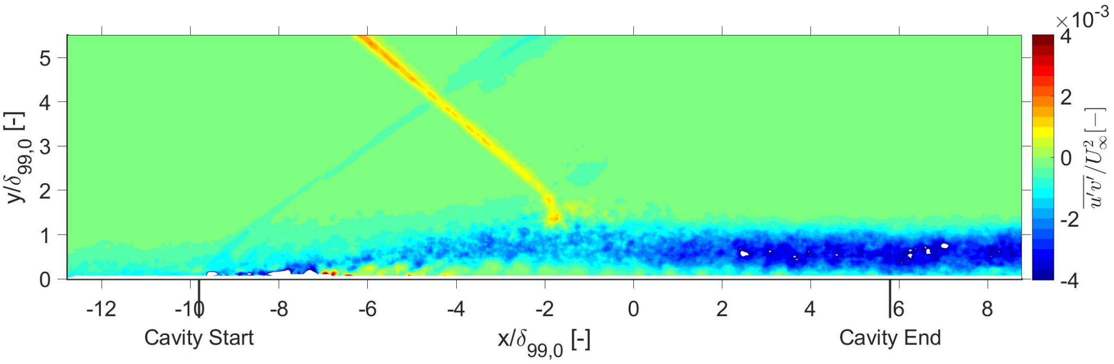

Figure E.28: $\overline{u'v'}$ flow field for 8.8° wedge and 1.0mm holes, 5% porosity plate

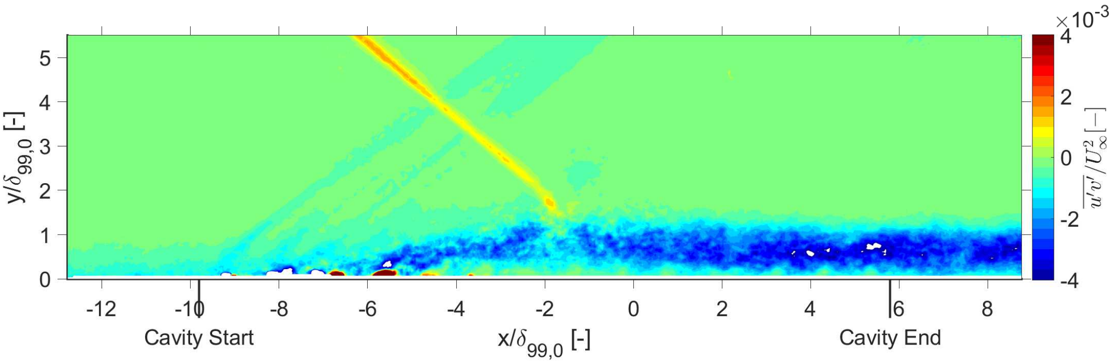

Figure E.29: $\overline{u'v'}$ flow field for 8.8° wedge and 1.5mm holes, 5% porosity plate

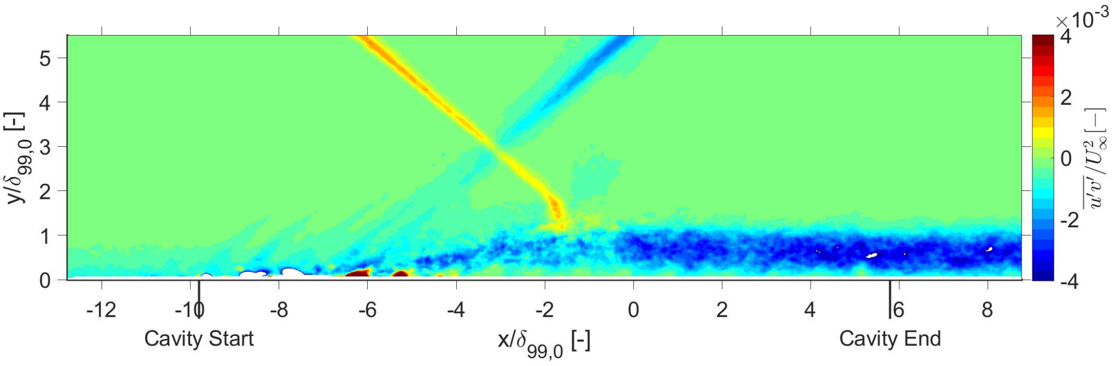

Figure E.30: $\overline{u'v}'$ flow field for 8.8° wedge and 1.0mm holes, 2.5% porosity plate